

INVITED COMMENT

In-medium similarity renormalization group for closed and open-shell nuclei

To cite this article: H Hergert 2017 *Phys. Scr.* **92** 023002

View the [article online](#) for updates and enhancements.

Related content

- [Coupled-cluster computations of atomic nuclei](#)
G Hagen, T Papenbrock, M Hjorth-Jensen et al.
- [New applications of renormalization group methods in nuclear physics](#)
R J Furnstahl and K Hebeler
- [Unified ab initio approaches to nuclear structure and reactions](#)
Petr Navrátil, Sofia Quaglioni, Guillaume Hupin et al.

Recent citations

- [Natural orbitals for ab initio no-core shell model calculations](#)
Alexander Tichai *et al*
- [Tensor-decomposition techniques for ab initio nuclear structure calculations: From chiral nuclear potentials to ground-state energies](#)
A. Tichai *et al*
- [Combining symmetry breaking and restoration with configuration interaction: Extension to z -signature symmetry in the case of the Lipkin model](#)
J. Ripoché *et al*

Invited Comment

In-medium similarity renormalization group for closed and open-shell nuclei

H Hergert

NSCL/FRIB Laboratory and Department of Physics & Astronomy, Michigan State University, East Lansing, MI 48824, USA

E-mail: hergert@nscl.msu.edu

Received 22 July 2016, revised 28 October 2016

Accepted for publication 7 November 2016

Published 19 December 2016

**Abstract**

We present a pedagogical introduction to the in-medium similarity renormalization group (IMSRG) framework for *ab initio* calculations of nuclei. The IMSRG performs continuous unitary transformations of the nuclear many-body Hamiltonian in second-quantized form, which can be implemented with polynomial computational effort. Through suitably chosen generators, it is possible to extract eigenvalues of the Hamiltonian in a given nucleus, or drive the Hamiltonian matrix in configuration space to specific structures, e.g., band- or block-diagonal form. Exploiting this flexibility, we describe two complementary approaches for the description of closed- and open-shell nuclei: the first is the multireference IMSRG (MR-IMSRG), which is designed for the efficient calculation of nuclear ground-state properties. The second is the derivation of non-empirical valence-space interactions that can be used as input for nuclear shell model (i.e., configuration interaction (CI)) calculations. This IMSRG+shell model approach provides immediate access to excitation spectra, transitions, etc, but is limited in applicability by the factorial cost of the CI calculations. We review applications of the MR-IMSRG and IMSRG+shell model approaches to the calculation of ground-state properties for the oxygen, calcium, and nickel isotopic chains or the spectroscopy of nuclei in the lower *sd* shell, respectively, and present selected new results, e.g., for the ground- and excited state properties of neon isotopes.

Keywords: nuclear many-body theory, renormalization group, *ab initio* nuclear structure theory, configuration interaction, shell model

(Some figures may appear in colour only in the online journal)

1. Introduction

More than 60 years have passed since Rainwater, Bohr, and Mottelson published the seminal works that led to them winning the 1975 Nobel prize in physics [1–5]. The collective model developed in these publications is an essential tool for nuclear physicists, and it qualifies as one of the most successful data-driven approaches to nuclear structure. A variety of approaches exist in this category, ranging from local to global applicability, and from microscopic to macroscopic views of nuclei: collective Bohr–Mottelson Hamiltonians are fine-tuned to specific nuclei or limited regions of the nuclear chart, and do not treat the dynamics of all nucleons on a fully

microscopic level. The traditional nuclear configuration interaction (CI) approach (see, e.g., [6, 7]) uses phenomenological interactions that are highly optimized, e.g., to *sd*-shell data [8], and treats only the dynamics of valence nucleons on top of an inert core in fully microscopic fashion. Finally, nuclear density functional theory takes a global perspective, and aims for a microscopic description of the entire nuclear chart based on energy density functionals that are optimized to data [9–12].

The philosophy behind data-driven models is complementary to that of *ab initio* nuclear many-body theory, although the lines are somewhat blurry. An *ab initio* approach attempts to describe nuclear structure and dynamics based on

fundamental degrees of freedom and their interactions. In the Standard Model, the fundamental theory of strong interactions is quantum chromodynamics (QCDs), but a description of nuclear observables on the level of quarks and gluons is not feasible, except for the lightest few-nucleon systems (see, e.g., [13]). Instead, we start from nuclear interactions that describe low-energy QCD observables in the NN and $3N$ systems, like scattering data or binding energies. Nowadays, such interactions are derived in chiral effective field theory (EFT), which provides a constructive framework and organizational hierarchy for NN , $3N$, and higher many-nucleon forces, as well as consistent electroweak operators (see, e.g., [14–24]). Since chiral EFT is a low-momentum expansion, high-momentum (short-range) physics is not explicitly resolved by the theory, but parametrized by the so-called low-energy constants (LECs).

In principle, the LECs can be determined by matching calculations of the same observables in chiral EFT and (Lattice) QCD in the overlap region of the two theories. Since such a calculation is currently not feasible, they are fit to experimental data, typically in the πN , NN , and $3N$ sectors. Recently, Ekström *et al* have developed an optimization protocol for chiral interactions that gives up on the reductionist approach of fixing the LECs in the few-nucleon system, and includes certain many-body data in the fit as well. The many-body data, e.g., selected radii, are chosen in order to improve the deficient saturation behavior of chiral interactions that are used as input for nuclear many-body calculations. The first interaction optimized with this protocol is NNLO_{sat} [25], which is able to accurately describe the ground-state energies and charge radii of $^{40,48}\text{Ca}$ at the same time. Following the same philosophy but not the same approach, Shirokov *et al* have produced Daejeon16, a softened chiral NN interaction that has been tuned for the description of light nuclei without explicit $3N$ forces [26–29].

Renormalization group (RG) methods are natural companions for EFTs, because they make it possible to smoothly connect theories with different resolution scales and degrees of freedom. Since they were introduced in low-energy nuclear physics around the start of the millennium [30–33], they have provided a systematic framework for formalizing many ideas on the renormalization of nuclear interactions and many-body effects that had been discussed in the nuclear structure community since the 1950s. For instance, soft and hard-core NN interactions can reproduce scattering data equally well, but have significantly different saturation properties, which caused the community to move away from the former in the 1970s (see, e.g., [34]). What was missing at that time was the recognition of the intricate link between the off-shell NN interaction and $3N$ forces that was formally demonstrated for the first time by Polyzou and Glöckle in 1990 [35]. From the modern RG perspective, soft- and hard-core interactions emerge as representations of low-energy QCD at different resolution scales, and the dialing of the resolution scale necessarily leads to induced $3N$ forces, in such a way that observables (including saturation properties) remain invariant under the RG flow (see section 2 and [32, 33]). In conjunction, chiral EFT and nuclear RG applications demonstrate that

one cannot treat the NN , $3N$, ... sectors in isolation from each other.

During the 1960s, Kuo and Brown pioneered work on the *ab initio* derivation of effective interactions for nuclear valence-space CI calculations, culminating in the publication of Hamiltonians for the sd and pf shells [36, 37]. Their approach relied on Brueckner’s G matrix to treat short-range correlations induced by the free-space NN interaction, and employed the so-called hole-line expansion to second order [38–40]. After some initial successes, Barret, Kirson, and others demonstrated a lack of order-by-order convergence of this expansion [41–45], and Vary, Sauer and Wong found a disturbingly strong model-space dependence in intermediate-state summations, with larger model spaces actually degrading the agreement with experimental data [46]. Bogner *et al* revisited this issue with the help of the similarity renormalization group (SRG) [47, 48], and demonstrated that the G matrix retains significant coupling between low- and high-momentum nodes of the underlying interaction [32], so the convergence issues are not surprising from a modern perspective. In the SRG and other modern RG approaches, low- and high-momentum physics are decoupled properly, and the resulting low-momentum $NN + 3N$ interactions are indeed perturbative [32, 49]. For such interactions, results from finite-order many-body perturbation theory (MBPT) are in good agreement with non-perturbative results if the expansion is based on a Hartree–Fock (HF) reference state [50, 51].

Of course, low-momentum $NN + 3N$ interactions are well-suited inputs not just for MBPT, but for all methods that work in truncated configuration spaces. The decoupling of low- and high-momentum modes of the interaction leads to a greatly improved convergence behavior, which in turn extends the range of nuclei a many-body method can be applied to. With SRG-evolved interactions, the no-core shell model (NCSM) and related large-scale diagonalization methods can be extended into the lower sd -shell [52–55], and methods with systematic many-body truncations like coupled cluster (CC) are nowadays applied to nuclei as heavy as tin [56–58].

Instead of merely using the SRG as a tool to ‘pre-process’ the nuclear interactions that are used as inputs for other many-body methods, we can turn it into a method for solving the many-body Schrödinger equation itself. This leads us to the so-called in-medium SRG (IMSRG), which is the main focus of the present work [59–61]. In a nutshell, we want to use SRG-like flow equations to decouple physics at different excitation energy scales of the nucleus, and render the Hamiltonian matrix in configuration space block or band diagonal in the process. This can also be viewed as a reorganization of the many-body expansion, in which correlations that are described explicitly by the configuration space are absorbed into an *RG-improved* Hamiltonian. With an appropriately chosen decoupling strategy, it is even possible to extract eigenvalues and eigenstates of the nuclear Hamiltonian, and therefore, the IMSRG qualifies as an *ab initio* method for solving quantum many-body problems.

In this work, we will discuss two distinct implementations of the IMSRG ideas. The first is the so-called

multireference IMSRG (MR-IMSRG), which is designed for calculations of the ground-state properties of closed- and open-shell nuclei. Like most many-body approaches, it relies on the organization of the many-body basis in terms of a reference state and its excitations. Contrary to approaches like MBPT or CI, which employ Slater determinant reference states, the MR-IMSRG is built for arbitrary correlated reference states. This gives us the greatest possible flexibility in the description of correlations: static correlations, e.g., due to intrinsic deformation, can be built into the reference state, while dynamic correlations due to the excitation of nucleon pairs, triples, etc are described by the MR-IMSRG transformation.

The second approach uses the IMSRG to construct RG-improved Hamiltonians for nuclear valence CI calculations. These interactions are subsequently used as input for existing shell model codes like NuShellX [62]. Such a combined approach gives us immediate access to a much larger number of observables than the MR-IMSRG, but it is limited by the computational effort of the CI part of the calculation.

The idea of using flow equations to solve quantum many-body problems was already discussed in Wegner's initial work on the SRG [48] (also see [63] and references therein). In the solid-state physics literature, the approach is also known as continuous unitary transformation (CUT) theory, see [64–68]. When we discuss our decoupling strategies for the nuclear many-body problem, it will become evident that the IMSRG is related to CC [57, 69], canonical transformation (CT) theory [70–72], and the irreducible (or anti-Hermitian) contracted Schrödinger equation (ICSE) approach [73–79], and there is even some overlap with purely variational methods (see section 4.3). What sets the IMSRG apart from these methods is that the Hamiltonian instead of the wave function is at the center of attention, in the spirit of RG methodology. This seems to be a trivial distinction, but there are practical advantages of this viewpoint, e.g., the simultaneous decoupling of ground and excited states (see section 4.2), the avoidance of N -representability issues [80], and more. Inspired in part by our work on the IMSRG in nuclear physics, Evangelista and co-workers have recently presented the Driven SRG for *ab initio* calculations in quantum chemistry, which implements IMSRG transformations in terms of inhomogeneous nonlinear equations rather than flow equations [81–84].

1.1. Organization of this work

Let us conclude our introduction of the IMSRG with a look ahead at the main body of this work. In section 2, we briefly review the essential concepts of the free-space SRG, and how it is used to dial the resolution scale of (nuclear) interactions and operators. To set up the IMSRG formalism, we first discuss normal-ordering techniques and Wick's theorem for arbitrary reference states in section 3. This will be followed by the presentation of the MR-IMSRG flow equations in section 4, which also discusses the choice of decoupling scheme and generators. The single-reference IMSRG

equations are obtained as a limit of the more general MR-IMSRG framework. In section 5, general features of (MR-) IMSRG flows are discussed, and section 6 reviews applications of the MR-IMSRG to the ground-state properties of closed- and open-shell nuclei. In section 7, we describe the derivation of non-empirical interactions for the nuclear valence-space CI approach. Salient points are summarized in section 8, and we look ahead at new developments. Expressions for products and commutators of normal-ordered operators are collected in appendix A, and appendix B recapitulates elements of the Hartree–Fock–Bogoliubov (HFB) theory and particle-number projection, which are used in the construction of reference states for the MR-IMSRG.

2. The similarity RG

2.1. General concept

The SRG was first formulated independently by Wegner [48] and Glazek and Wilson [47], for applications in condensed matter physics and light-front quantum field theory, respectively. The general concept of the method is to simplify the structure of the Hamiltonian in a suitable representation through the use of a continuous unitary transformation,

$$H(s) = U(s)H(0)U^\dagger(s). \quad (1)$$

Here, $H(s=0)$ is the starting Hamiltonian and s denotes the so-called flow parameter, which parameterizes the unitary transformation. Taking the derivative of equation (1) with respect to s , we obtain the operator flow equation

$$\frac{d}{ds}H(s) = [\eta(s), H(s)], \quad (2)$$

where the anti-Hermitian generator $\eta(s)$ is related to $U(s)$ by

$$\eta(s) = \frac{dU(s)}{ds}U^\dagger(s) = -\eta^\dagger(s). \quad (3)$$

By rearranging this relation, we obtain a differential equation for $U(s)$ whose formal solution is given by the *path*- or *S-ordered* exponential [85, 86]

$$\begin{aligned} U(s) &= \mathcal{S} \exp \int_0^s ds' \eta(s') \\ &\equiv \sum_n \frac{1}{n!} \int_0^s ds_1 \int_0^{s_1} ds_2 \dots \int_0^{s_{n-1}} ds_n \mathcal{S} \{ \eta(s_1) \dots \eta(s_n) \}. \end{aligned} \quad (4)$$

Here, the S -ordering operator \mathcal{S} ensures that the flow parameters appearing in the integrands are always in descending order, $s_1 > s_2 > \dots$. Since our continuous unitary transformation preserves the spectrum of the Hamiltonian and any other observable of interest, it is an example of a so-called isospectral flow, a class of transformations which has been studied extensively in the mathematics literature (see, e.g., [87–89]).

With a suitable choice of generator $\eta(s)$, we can smoothly transform the Hamiltonian to almost arbitrary structures as we integrate the flow equation (2) for $s \rightarrow \infty$.

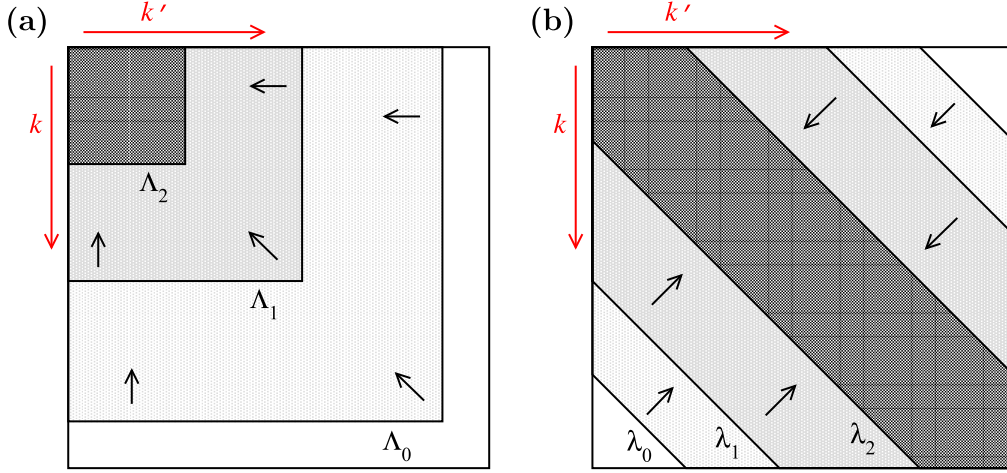


Figure 1. Schematic illustration of two types of RG evolution for NN potentials in momentum space: (a) $V_{\text{low-}k}$ running in Λ , and (b) SRG running in λ (see main text). Here, k and k' denote the relative momenta of the initial and final state, respectively. At each Λ_i or λ_i , the matrix elements outside of the corresponding blocks or bands are negligible, implying that high- and low-momentum states are decoupled.

Inspired by the work of Brockett [87] on the so-called double-bracket flow, Wegner [48] proposed the generator

$$\eta(s) \equiv [H_d(s), H_{\text{od}}(s)], \quad (5)$$

which is constructed by splitting the Hamiltonian into suitably chosen *diagonal* ($H_d(s)$) and *offdiagonal* ($H_{\text{od}}(s)$) parts. It can be shown analytically that the generator (5) will monotonically suppress $H_{\text{od}}(s)$ as the Hamiltonian is evolved via equation (2) (see, e.g., [48, 61, 63]). Note that the label diagonal does not need to mean strict diagonality here, but rather refers to a desired structure that the Hamiltonian will assume in the limit $s \rightarrow \infty$. By working in bases that are ordered by momenta or energies, the capability to impose structure on the Hamiltonian allows us to make an explicit connection with RG ideas.

2.2. SRG evolution of nuclear interactions

In figure 1, we show schematic examples of RG evolutions that are applied to nucleon-nucleon interactions in momentum-space representation. Figure 1(a) implements the RG as a decimation: The interaction is evolved to decreasing cutoff scales $\Lambda_0 > \Lambda_1 > \Lambda_2$, and we end up with a low-momentum interaction $V_{\text{low-}k}$ that only has non-zero matrix elements between states with initial and final relative momenta $k, k' \leq \Lambda$ [30, 32]. In contrast, figure 1(b) results from a transformation via the flow equation (2), using a Wegner-type generator built from the relative kinetic energy in the two-nucleon system:

$$\eta(\lambda) \equiv \left[\frac{\vec{k}^2}{2\mu}, v(\lambda) \right]. \quad (6)$$

Here, $\vec{k} = \frac{1}{2}(\vec{p}_1 - \vec{p}_2)$, and μ is the reduced nucleon mass. We have parametrized the transformation with $\lambda = s^{-1/4}$, which has the dimensions of a momentum (in natural units). As suggested by figure 1(b), λ is a measure for the ‘width’ of the band-diagonal Hamiltonian in momentum space, i.e., it controls the scale of momentum transfers between nucleons.

Because

$$|\vec{q}| = |\vec{k}' - \vec{k}| \lesssim \lambda \quad (7)$$

low- and high-lying momenta are decoupled in a proper RG sense as λ is decreased.

The decoupling of low- and high-lying momenta significantly improves the convergence properties of configuration-space based many-body methods, because it prevents the Hamiltonian from scattering nucleon pairs from low to high momentum states. Methods like the NCSM or the IMSRG discussed below yield converged results in much smaller many-body Hilbert spaces, which in turn makes it possible to apply these methods to heavier nuclei [52–56, 60, 61, 90–98]. However, this improvement comes at a cost, which is best illustrated by considering the Hamiltonian in a second-quantized form, assuming only a two-nucleon interaction for simplicity:

$$H_{\text{int}} = T_{\text{rel}} + V = \frac{1}{4} \sum_{pqrs} \langle pq | \frac{\vec{k}_{12}^2}{2\mu} + v_{12} | rs \rangle a_p^\dagger a_q^\dagger a_s a_r. \quad (8)$$

If we plug T_{rel} and V into the commutators in equations (6) and (2), we obtain

$$\begin{aligned} [a_i^\dagger a_j^\dagger a_l a_k, a_p^\dagger a_q^\dagger a_s a_r] = & \delta_{lp} a_i^\dagger a_j^\dagger a_q^\dagger a_s a_r a_k + \{a_i^\dagger a^\dagger a a a\} \\ & - \delta_{lp} \delta_{kq} a_i^\dagger a_j^\dagger a_s a_r + \{a_i^\dagger a^\dagger a a\}, \end{aligned} \quad (9)$$

where the bracketed terms with suppressed indices schematically stand for additional two- and three-body operators. Thus, even if we start from a pure two-body interaction, the SRG flow will induce operators of higher rank, i.e., three-, four-, and in general up to A -nucleon interactions. Of course, these induced interactions are only probed if we study an A -nucleon system. If we truncate the SRG flow equations at the two-body level, we preserve the properties of the two-nucleon system, in particular phase shifts and the deuteron binding energy. A truncation at the three-body level ensures the invariance of observables in $A = 3$ nuclei, e.g. ^3H and ^3He

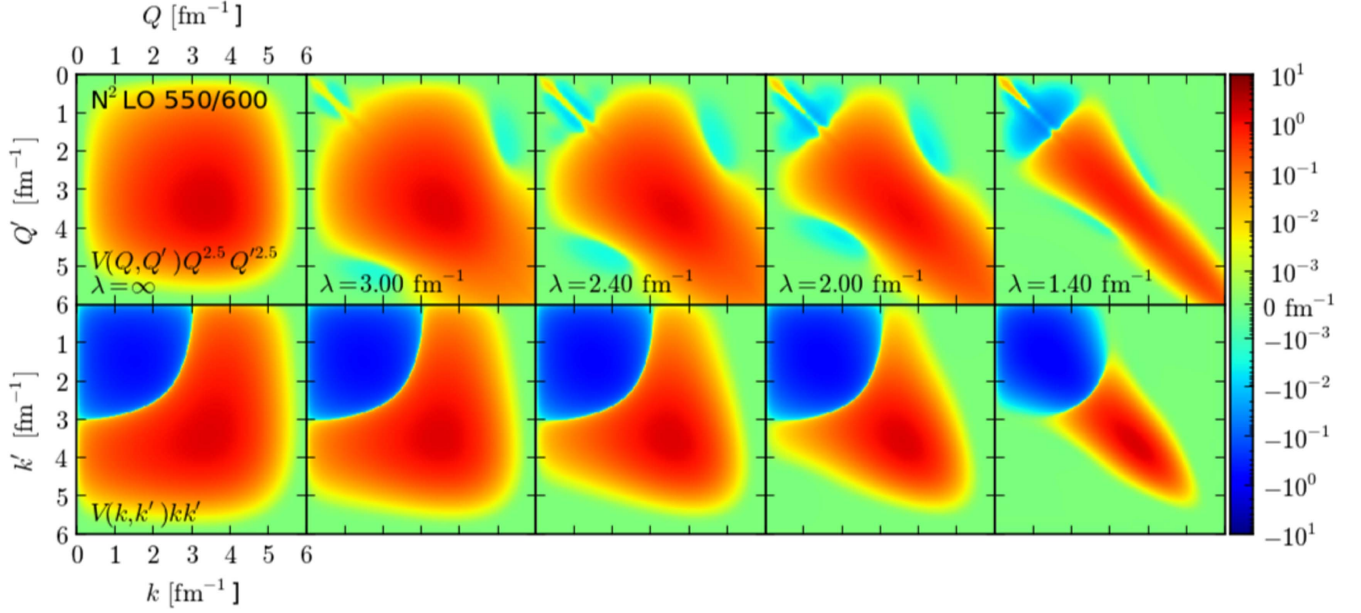


Figure 2. SRG evolution of a chiral NNLO $NN + 3N$ Hamiltonian with cutoffs 550/600 MeV [104, 105] in a three-body hyperspherical momentum basis. The figure shows contour plots of the matrix elements as a function of λ in the lowest hyperspherical partial wave, both for the $3N$ interaction (top panel) and the embedded NN interaction in that partial wave (lower panel). See [107] for additional details. Figure reproduced with permission from [107] Copyright American Physical Society 2013.

ground-state energies, and so on. Truncations in the SRG flow equation cause a violation of unitarity that manifests as a (residual) dependence of many-body results on λ . By varying this parameter, the size of the missing contributions can be assessed (see, e.g., [32, 54, 56, 60, 90, 98–101]).

State-of-the-art SRG evolutions of nuclear interactions are nowadays performed in the three-body system, using relative (Jacobi) harmonic oscillator [53, 99, 102], relative momentum plane wave [100], or momentum-space hyperspherical harmonics representations [103]. Pioneering work on implementing the SRG evolution in the lowest partial waves of the four-body system has been carried out by Calci and co-workers [109], again working in Jacobi HO representation.

Figure 2 shows the evolution of NN and $3N$ matrix elements of a chiral NNLO interaction by Epelbaum, Glöckle, and Meißner [104, 105], with cutoffs 550/600 MeV. As discussed for our schematic example, both the NN and $3N$ interactions become band diagonal and the SRG decouples the low- and high-momentum regimes as we evolve to lower values of λ . In figure 3, the same family of SRG-evolved interactions is used to calculate the ground-state energy of the triton, as a function of λ . If only the NN part of the chiral interaction is used as input, and the SRG generator and flowing Hamiltonian are truncated at the two-body level (NN -only), the SRG evolution is not unitary in the three-body system. The energy exhibits a significant dependence on λ , on the order of 5%–6%. If the flow equations are truncated at the three-body level instead, induced $3N$ interactions are properly included and the unitarity of the transformation is restored ($NN + 3N$ -induced): The energy does not change as λ is varied. Finally, the curve $NN + 3N$ -full shows the result for a calculation with initial NN and $3N$ forces, which are

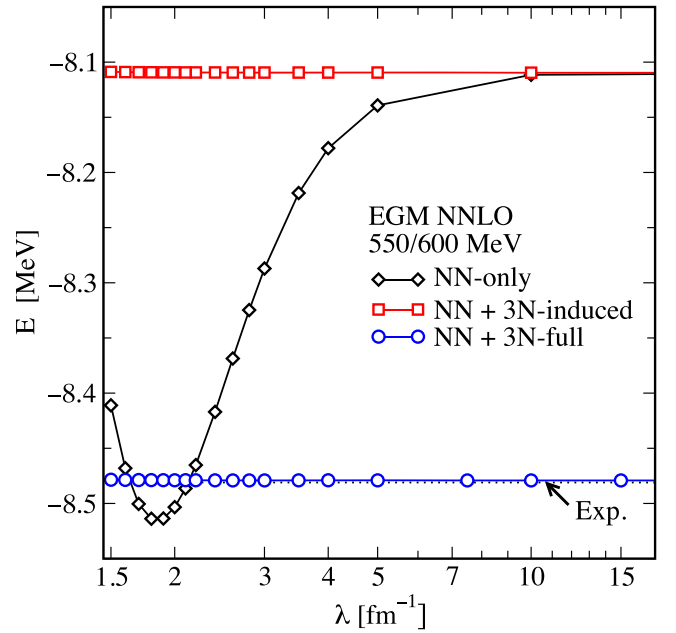


Figure 3. Ground state energy of ${}^3\text{H}$ as a function of the flow parameter λ for a chiral NNLO $NN + 3N$ interaction with cutoffs 550/600 MeV (see figure 2 and [104, 105]). NN -only means initial and induced $3N$ interactions are discarded, $NN + 3N$ -induced takes only induced $3N$ interactions into account, and $3N$ -full contains initial $3N$ interactions as well. The black dotted line shows the experimental binding energy [108]. Data courtesy of K. Hebeler.

consistently SRG-evolved at the three-body level. The triton ground-state energy is again invariant under the SRG flow, and closely reproduces the experimental value that is used as a constraint in the adjustment of the $3N$ force's LECs (see, e.g., [14, 15, 106]).

The SRG flow equations force us to manipulate large sections (or the entirety) of the Hamiltonian's spectrum in order to avoid basis truncation artifacts (also see [55, 56]). We may ask, then, if it might be possible to avoid the use of matrix representations entirely by solving the operator flow equation (2) directly in the algebra of operators. This is the strategy that we will explore in the following, which will ultimately lead us to the formulation of the IMSRG. First, we have to lay some groundwork on normal-ordering techniques and Wick's theorem.

3. Normal ordering and Wick's theorem for arbitrary reference states

3.1. Reference states and many-body bases

To describe the structure and dynamics of an atomic nucleus of mass A , we need to work in an A -body Hilbert space¹, and choose a suitable A -body basis. Since we are dealing with a system of fermions, a straightforward choice are *antisymmetrized product states*, or *Slater determinants*. Introducing fermionic creation and annihilation operators a_i^\dagger and a_j that satisfy the canonical anticommutation relations

$$\{a_i^\dagger, a_j^\dagger\} = \{a_i, a_j\} = 0, \{a_i^\dagger, a_j\} = \delta_{ij}, \quad (10)$$

we can write a generic A -particle Slater determinant as

$$|\Phi\rangle = \prod_{k=1}^A a_{i_k}^\dagger |\text{vac}\rangle, \quad (11)$$

where $|\text{vac}\rangle$ refers to the particle vacuum. Here, the indices run over a suitably chosen single-particle basis, e.g., spatially localized orbitals if we plan to describe a finite system like a nucleus. A complete basis for the many-body Hilbert space can be obtained by distributing A nucleons over the available single-particle states in all possible ways.

Of course, not all of the states in this naively chosen basis are created equal. As alluded to in section 2, nuclear interactions and the nucleus itself have characteristic energy or momentum scales. The ground state and low-lying excitation spectrum of an A -body nucleus is typically dominated by excitations of particles in the vicinity of its Fermi energy. Thus, we can find a Slater determinant $|\Phi\rangle$ that is a fair approximation to the nuclear ground state, and use it as a *reference state* for the construction and organization of our many-body basis. Slater determinants that are variationally optimized through a HF procedure have been shown to be reasonable reference states for interactions with low resolution scales around $\lambda = 2.0 \text{ fm}^{-1}$ (see, e.g., [32, 50, 52, 57, 61, 114] and references therein), allowing post-HF methods like MBPT, CC, or the IMSRG discussed below to converge rapidly to the exact Full CI result. Starting from such a HF reference state $|\Phi_{\text{HF}}\rangle$, we can obtain a basis

consisting of the state itself and up to A -particle, A -hole ($ApAh$) excitations:

$$|\Phi_{\text{HF}}\rangle, a_{p_1}^\dagger a_{h_1} |\Phi_{\text{HF}}\rangle, \dots, a_{p_1}^\dagger \dots a_{p_A}^\dagger a_{h_A} \dots a_{h_1} |\Phi_{\text{HF}}\rangle. \quad (12)$$

Here, indices p_i and h_i run over all one-body basis states with energies above (*particle* states) and below the Fermi level (*hole* states), respectively.

Many-body bases built from such a single Slater determinant and its particle-hole excitations work best for systems with large gaps in the single-particle spectrum, e.g., closed-shell nuclei. If the gap is small, particle-hole excited basis states can be near-degenerate with the reference state, which usually results in spontaneous symmetry breaking and strong configuration mixing. At best, these phenomena impede the convergence of a many-body calculation by forcing us to use model spaces that contain nph excitations with large n , e.g., in a CI framework. At worst, the behavior of a truncated many-body method like IMSRG or CC may be completely uncontrolled. We want to overcome these problems by building correlations from configuration mixing into the reference state, and constructing a basis of generalized $ApAh$ excitations on top of this state. A key element of such an approach are generalized normal ordering techniques.

3.2. Normal-ordered operators and Wick contractions

In [115], Kutzelnigg and Mukherjee developed a generalized normal ordering for arbitrary reference states. Here, we present the essential elements of their discussion that we will need in the following, but use the slightly different notation of Kong *et al* [116].

First, we introduce a pseudo-tensorial notation for strings of creation and annihilation operators, to facilitate book-keeping and make the formalism more compact. A particle-number conserving product of k creators and annihilators each is written as

$$A_{j_1 \dots j_k}^{i_1 \dots i_k} \equiv a_{i_1}^\dagger \dots a_{i_k}^\dagger a_{j_k} \dots a_{j_1}. \quad (13)$$

We do not consider particle-number changing operators in the present work, because they cause ambiguities in the contraction and sign rules for the A operators that are defined in the following. The anticommutation relations imply

$$A_{j_1 \dots j_k}^{\mathcal{P}(i_1 \dots i_k)} = (-1)^{\pi(\mathcal{P}) + \pi(\mathcal{P}')} A_{j_1 \dots j_k}^{i_1 \dots i_k}, \quad (14)$$

where $\pi(\mathcal{P}) = \pm 1$ indicates the parity (or signature) of a permutation \mathcal{P} . A general k -body operator in second quantization can now be written in terms of the basis operators as

$$O^{(k)} = \frac{1}{(k!)^2} \sum_{i_1 \dots i_k} o_{j_1 \dots j_k}^{i_1 \dots i_k} A_{j_1 \dots j_k}^{i_1 \dots i_k}, \quad (15)$$

where we assume that the coefficients $o_{j_1 \dots j_k}^{i_1 \dots i_k}$ are antisymmetrized, and therefore also obey equation (14) under index permutations.

Next, we introduce *irreducible k -body density matrices* $\chi^{(k)}$. In the one-body case, we have the usual density matrix

$$\chi_j^i \equiv \langle \Phi | A_j^i | \Phi \rangle, \quad (16)$$

¹ To include continuum degrees of freedom, i.e., resonant and scattering states, we would have to treat the nucleus as an open quantum system in a so-called rigged Hilbert space [110, 111]. This setting also creates opportunities for a completely microscopic description of nuclear reactions, see, e.g., [112, 113].

and for future use, we also define

$$\xi_j^i \equiv \lambda_j^i - \delta_j^i. \quad (17)$$

Up to a factor (-1) that unifies the sign rules for one-body contractions presented below, $\xi^{(1)}$ is simply the generalization of the hole density matrix for a correlated state. In the natural orbital basis, i.e., the eigenbasis of $\lambda^{(1)}$, both one-body density matrices are diagonal:

$$\lambda_j^i = n_i \delta_j^i, \quad \xi_j^i = -\bar{n}_i \delta_j^i \equiv -(1 - n_i) \delta_j^i. \quad (18)$$

The fractional occupation numbers $0 \leq n_i \leq 1$ are the eigenvalues of $\lambda^{(1)}$.

For $k \geq 2$, we denote full density matrices by

$$\rho_{j_1 \dots j_k}^{i_1 \dots i_k} = \langle \Phi | A_{j_1 \dots j_k}^{i_1 \dots i_k} | \Phi \rangle, \quad (19)$$

and define

$$\lambda_{kl}^{ij} \equiv \rho_{kl}^{ij} - \mathcal{A}\{\lambda_k^i \lambda_l^j\}, \quad (20)$$

$$\lambda_{lmn}^{ijk} \equiv \rho_{lmn}^{ijk} - \mathcal{A}\{\lambda_l^i \lambda_m^j \lambda_n^k\} - \mathcal{A}\{\lambda_l^i \lambda_m^k \lambda_n^j\}, \quad (21)$$

etc, where $\mathcal{A}\{\dots\}$ fully antisymmetrizes the indices of the expression within the brackets, e.g.,

$$\mathcal{A}\{\lambda_k^i \lambda_l^j\} = \lambda_k^i \lambda_l^j - \lambda_l^i \lambda_k^j. \quad (22)$$

From equation (20), it is easy to see that $\lambda^{(2)}$ encodes the two-nucleon correlation content of the reference state $|\Phi\rangle$. If the reference state is a Slater determinant, i.e., an independent-particle state, the full two-body density matrix factorizes, and $\lambda^{(2)}$ vanishes:

$$\begin{aligned} \lambda_{kl}^{ij} &= \rho_{kl}^{ij} - \mathcal{A}\{\lambda_k^i \lambda_l^j\} \\ &= \lambda_k^i \lambda_l^j - \lambda_k^i \lambda_l^j - (\lambda_k^i \lambda_l^j - \lambda_k^j \lambda_l^i) = 0. \end{aligned} \quad (23)$$

Equation (21) shows that $\lambda^{(3)}$ is constructed by subtracting contributions from three independent particles as well as two correlated nucleons in the presence of an independent spectator particle from the full three-body density matrix, and therefore encodes the genuine three-nucleon correlations. This construction and interpretation generalizes to irreducible density matrices of rank k .

Now we consider the expansion of a (number-conserving) string of creation and annihilation operators in normal-ordered components. First, we define a normal-ordered one-body operator by subtracting from a given one-body operator its expectation value in the reference state:

$$:A_b^a: \equiv A_b^a - \langle \Phi | A_b^a | \Phi \rangle = A_b^a - \lambda_b^a. \quad (24)$$

This implies that the expectation value of the normal-ordered operator in the reference state vanishes by construction:

$$\langle \Phi | :A_b^a: | \Phi \rangle = 0. \quad (25)$$

For a two-body operator, we have the expansion

$$\begin{aligned} A_{cd}^{ab} &= :A_{cd}^{ab}: + \lambda_c^a :A_d^b: \\ &\quad - \lambda_d^a :A_c^b: + \lambda_d^b :A_c^a: - \lambda_c^b :A_d^a: \\ &\quad + \lambda_c^a \lambda_d^b - \lambda_d^a \lambda_c^b + \lambda_{cd}^{ab}. \end{aligned} \quad (26)$$

As a consequence of equation (14), the sign of each term is determined by the product of the parities of the permutations

that map upper and lower indices to their ordering in the initial operator. Except for the last term, this expression looks like the result for the regular normal ordering, with pairwise contractions of indices giving rise to one-body density matrices. The last term, a contraction of four indices, appears because we are dealing with an arbitrary, correlated reference state here.

Taking the expectation value of equation (26) and using equation (25), we obtain

$$\begin{aligned} \rho_{cd}^{ab} &= \langle \Phi | :A_{cd}^{ab}: | \Phi \rangle \\ &\quad + \underbrace{\lambda_c^a \lambda_d^b - \lambda_d^a \lambda_c^b + \lambda_{cd}^{ab}}_{=\rho_{cd}^{ab}}, \end{aligned} \quad (27)$$

and see that

$$\langle \Phi | :A_{cd}^{ab}: | \Phi \rangle = 0. \quad (28)$$

The normal ordering procedure can be extended in analogy to the one- and two-body cases, e.g.,

$$\begin{aligned} A_{def}^{abc} &= :A_{def}^{abc}: + \mathcal{A}\{\lambda_d^a :A_e^b :A_f^c :\} \\ &\quad + \mathcal{A}\{\lambda_d^a \lambda_e^b :A_f^c :\} + \mathcal{A}\{\lambda_{de}^{ab} :A_f^c :\} \\ &\quad + \lambda_{def}^{abc} + \mathcal{A}\{\lambda_d^a \lambda_e^b \lambda_f^c\} + \mathcal{A}\{\lambda_d^a \lambda_e^c \lambda_f^b\}, \end{aligned} \quad (29)$$

yielding normal-ordered operators of arbitrary rank k that satisfy

$$\langle \Phi | :A_{j_1 \dots j_k}^{i_1 \dots i_k}: | \Phi \rangle = 0. \quad (30)$$

Finally, a generalized Wick's theorem for arbitrary reference states can be formulated: any product of two normal-ordered operators can be expanded in a sum of normal-ordered terms, with Wick contractions and operators containing at least one index from each of the original operators. For example, the basic contractions appearing in the expansion of a product of normal-ordered two-body operators are (notice the signs)

$$:A_{cd}^{a\bar{b}}::A_{kl}^{ij}: = -\lambda_{kl}^{\bar{a}} :A_{cdl}^{aij}:, \quad (31)$$

$$:A_{cd}^{ab}:A_{kl}^{i\bar{j}}: = -\xi_{kl}^{\bar{a}} :A_{cdkl}^{bia}:, \quad (32)$$

$$:A_{cd}^{a\bar{b}}::A_{kl}^{ij}: = +\lambda_{kl}^{\bar{a}} :A_{cd}^{ij}:, \quad (33)$$

$$:A_{cd}^{a\bar{b}}::A_{kl}^{i\bar{j}}: = -\lambda_{kl}^{\bar{a}} :A_{cd}^{aj}:, \quad (34)$$

$$:A_{cd}^{ab}:A_{kl}^{i\bar{j}}: = -\lambda_{kl}^{\bar{a}} :A_{cdl}^{ab}:, \quad (35)$$

$$:A_{cd}^{a\bar{b}}::A_{kl}^{i\bar{j}}: = -\lambda_{kl}^{\bar{a}} :A_{cd}^{j}:, \quad (36)$$

$$:A_{cd}^{a\bar{b}}::A_{kl}^{i\bar{j}}: = +\lambda_{cdkl}^{\bar{a}b\bar{i}j}. \quad (37)$$

Only the first two contraction types, equations (31) and (32), appear in the regular Wick's theorem for uncorrelated reference states. The additional contractions (33)–(37) increase the number of terms when we expand operator products using the generalized Wick's theorem—examples are shown in appendix A. Fortunately, we will see in section 4 that the overall increase in complexity is manageable.

3.3. Normal-ordered Hamiltonian and normal-ordered two-body approximation

We conclude this section by applying the generalized normal ordering to an intrinsic nuclear A -body Hamiltonian containing both NN and $3N$ interactions, which will be relevant for the applications discussed later in this work. Let

$$H = \left(1 - \frac{1}{A}\right)T^{(1)} + \frac{1}{A}T^{(2)} + V^{(2)} + V^{(3)}, \quad (38)$$

where

$$T^{(1)} \equiv \sum_i \frac{\vec{p}_i^2}{2m}, \quad T^{(2)} \equiv -\sum_{i<j} \frac{\vec{p}_i \cdot \vec{p}_j}{m} \quad (39)$$

(see, e.g., [117]). Choosing a generic correlated reference state $|\Phi\rangle$, we rewrite the Hamiltonian as

$$H = E + \sum_{ij} f_j^i : A_j^i : + \frac{1}{4} \sum_{ijkl} \Gamma_{kl}^{ij} : A_{kl}^{ij} : + \frac{1}{36} \sum_{ijklmn} W_{lmn}^{ijk} : A_{lmn}^{ijk} :, \quad (40)$$

where the labels have been chosen for historical reasons. The individual normal-ordered contributions in equation (40) are given by

$$E = \left(1 - \frac{1}{A}\right) \sum_{ab} t_b^a \lambda_b^a + \frac{1}{4} \sum_{abcd} \left(\frac{1}{A} t_{cd}^{ab} + v_{cd}^{ab}\right) \rho_{cd}^{ab} + \frac{1}{36} \sum_{abcdef} v_{def}^{abc} \rho_{def}^{abc}, \quad (41)$$

$$f_j^i = \left(1 - \frac{1}{A}\right) t_j^i + \sum_{ab} \left(\frac{1}{A} t_{jb}^{ia} + v_{jb}^{ia}\right) \lambda_b^a + \frac{1}{4} \sum_{abcd} v_{jcd}^{iab} \rho_{cd}^{ab}, \quad (42)$$

$$\Gamma_{kl}^{ij} = \frac{1}{A} t_{kl}^{ij} + v_{kl}^{ij} + \sum_{ab} v_{klb}^{ija} \lambda_b^a, \quad (43)$$

$$W_{lmn}^{ijk} = v_{lmn}^{ijk}. \quad (44)$$

Here, we use the full density matrices for compactness, but it is easy to express equations (41)–(43) completely in terms of irreducible density matrices by using equations (20) and (21). Note that the normal-ordered zero-, one-, and two-body parts of the Hamiltonian all contain in-medium contributions from the free-space $3N$ interaction. It has been shown empirically that the omission of the normal-ordered three-body piece of the Hamiltonian causes a deviation of merely 1%–2% in ground-state and (absolute) excited state energies of light and medium-mass nuclei [90, 93, 118–120]. This *normal-ordered two-body approximation* (NO2B) to the Hamiltonian is widely used nowadays, because it provides an efficient means to account for $3N$ force effects in nuclear many-body calculations without incurring the computational expense of explicitly treating three-body operators. In the next section, we will also see that the NO2B approximation meshes in a natural way with the framework of the MR-IMSRG, which makes it especially appealing for our purposes.

4. The multireference in-medium SRG

4.1. MR-IMSRG flow equations

We are now ready to formulate the MR-IMSRG flow equations by applying the tools discussed in the previous section to the operator differential equation (2). We express all operators in terms of normal-ordered strings of creation and annihilation operators. As discussed in section 2, each evaluation of the commutator on the right-hand side will induce operators of higher rank,

$$[:A_{cd}^{ab} : ; :A_{kl}^{ij} :] = \delta_{ci} : A_{dkl}^{abj} : + \dots, \quad (45)$$

and we would need to include operators up to rank A if we want the MR-IMSRG flow to be unitary in an A -body system, which is not feasible. However, in contrast to equation (9), we are now working with *normal-ordered* operators whose in-medium contributions have been absorbed into terms of lower rank. Consequently, we expect the induced operators to be much weaker than in the free-space SRG case. The empirical success of the NO2B approximation discussed at the end of section 3 certainly seems to justify this expectation in the case of nuclear $NN+3N$ Hamiltonians with low resolution scales.

Following this line of reasoning further, we choose to truncate all flowing operators at a given particle rank $n \leq A$ in order to obtain a closed system of flow equations. For $n = 2$, we demand that for all values of the flow parameter s

$$\eta(s) \approx \eta^{(1)}(s) + \eta^{(2)}(s), \quad (46)$$

$$H(s) \approx E(s) + f(s) + \Gamma(s), \quad (47)$$

$$\frac{d}{ds} H(s) \approx \frac{d}{ds} E(s) + \frac{d}{ds} f(s) + \frac{d}{ds} \Gamma(s). \quad (48)$$

This is the so-called MR-IMSRG(2) truncation, which has been our primary workhorse in past applications [54, 59–61, 91, 121, 122]. It is the basis for all results in this work. We note that the MR-IMSRG(2) at this specific level of truncation is a cousin to a variety of other truncated many-body schemes, e.g., canonical transformation theory with singles and doubles excitations (CTSDs) [70–72], the two-body antisymmetrized or ICSE approach (ICSE(2)) [73–79] and of course CCSD (CC with Singles and Doubles) (see, e.g., [69]), although the latter is based on non-unitary similarity transformations.

Plugging equations (46)–(48) into the operator flow equation (2) and organizing contributions by particle rank, we obtain the system of MR-IMSRG(2) flow equations:

$$\begin{aligned} \frac{dE}{ds} = & \sum_{ab} (n_a - n_b) \eta_b^a f_a^b \\ & + \frac{1}{4} \sum_{abcd} (\eta_{cd}^{ab} \Gamma_{ab}^{cd} - \Gamma_{cd}^{ab} \eta_{ab}^{cd}) n_a n_b \bar{n}_c \bar{n}_d \\ & + \frac{1}{4} \sum_{abcd} \left(\frac{d}{ds} \Gamma_{cd}^{ab} \right) \lambda_{cd}^{ab} \\ & + \frac{1}{4} \sum_{abcdklm} (\eta_{cd}^{ab} \Gamma_{am}^{kl} - \Gamma_{cd}^{ab} \eta_{am}^{kl}) \lambda_{cdm}^{bkl}, \end{aligned} \quad (49)$$

$$\begin{aligned}
\frac{d}{ds} f_j^i = & \sum_a (\eta_a^i f_j^a - f_a^i \eta_j^a) \\
& + \sum_{ab} (\eta_b^a \Gamma_{aj}^{bi} - f_b^a \eta_{aj}^{bi}) (n_a - n_b) \\
& + \frac{1}{2} \sum_{abc} (\eta_{bc}^{ia} \Gamma_{ja}^{bc} - \Gamma_{bc}^{ia} \eta_{ja}^{bc}) (n_a \bar{n}_b \bar{n}_c + \bar{n}_a n_b n_c) \\
& + \frac{1}{4} \sum_{abcde} (\eta_{bc}^{ia} \Gamma_{ja}^{de} - \Gamma_{bc}^{ia} \eta_{ja}^{de}) \lambda_{bc}^{de} \\
& + \sum_{abcde} (\eta_{bc}^{ia} \Gamma_{jd}^{be} - \Gamma_{bc}^{ia} \eta_{jd}^{be}) \lambda_{cd}^{ae} \\
& - \frac{1}{2} \sum_{abcde} (\eta_{jb}^{ia} \Gamma_{ae}^{cd} - \Gamma_{jb}^{ia} \eta_{ae}^{cd}) \lambda_{be}^{cd} \\
& + \frac{1}{2} \sum_{abcde} (\eta_{jb}^{ia} \Gamma_{de}^{bc} - \Gamma_{jb}^{ia} \eta_{de}^{bc}) \lambda_{de}^{ac},
\end{aligned} \tag{50}$$

$$\begin{aligned}
\frac{d}{ds} \Gamma_{kl}^{ij} = & \sum_a (\eta_a^i \Gamma_{kl}^{aj} + \eta_a^j \Gamma_{kl}^{ia} - \eta_k^a \Gamma_{al}^{ij} - \eta_l^a \Gamma_{ka}^{ij}) \\
& - f_a^i \eta_{kl}^{aj} - f_a^j \eta_{kl}^{ia} + f_k^a \eta_{al}^{ij} + f_l^a \eta_{ka}^{ij} \\
& + \frac{1}{2} \sum_{ab} (\eta_{ab}^{ij} \Gamma_{kl}^{ab} - \Gamma_{ab}^{ij} \eta_{kl}^{ab}) (1 - n_a - n_b) \\
& + \sum_{ab} (n_a - n_b) ((\eta_{kb}^{ia} \Gamma_{la}^{jb} - \Gamma_{kb}^{ia} \eta_{la}^{jb}) \\
& - (\eta_{kb}^{ja} \Gamma_{la}^{ib} - \Gamma_{kb}^{ja} \eta_{la}^{ib})).
\end{aligned} \tag{51}$$

All single-particle indices and occupation numbers (see section 3) refer to natural orbitals, and the s -dependence has been suppressed for brevity. The *single-reference limit* is readily obtained by setting the irreducible density matrices $\lambda^{(2)}$ and $\lambda^{(3)}$ to zero in the previous expressions.

We solve the flow equations (49)–(51) by integrating from $s = 0$ to $s \rightarrow \infty$, using the components of the normal-ordered input Hamiltonian (equations (41)–(43)) as initial values. In this process, the flow equations will re-shuffle the correlations in the A -body system, generating a highly non-perturbative resummation of the many-body expansion (see section 5.2 for numerical examples).

To interpret the multireference flow equations, we associate the fractional occupation numbers \bar{n}_i and n_i with particle- and hole-like states, respectively (see equation (18)), and note that

$$1 - n_a - n_b = \bar{n}_a \bar{n}_b - n_a n_b, \tag{52}$$

$$n_a - n_b = n_a \bar{n}_b - \bar{n}_a n_b. \tag{53}$$

For the typical ansätze that we use for $\eta(s)$ (see section 4.3), the generator is proportional to the (offdiagonal) Hamiltonian, and we see the first two terms of the zero-body flow equation have the structure of second-order energy corrections, but evaluated for the *flowing* Hamiltonian $H(s)$. Furthermore, we recognize that the second and third lines of equation (51) have the structure of ladder (particle–particle/hole–hole) and ring (particle–hole) skeleton diagrams, respectively. They generate ladder and ring summations in the limit $s \rightarrow \infty$, but also ring-ladder interference diagrams with rich topologies that go far beyond traditional re-summation methods [40, 123, 124]. A detailed perturbative analysis is presented in [61].

For general reference states, the MR-IMSRG flow equations also include couplings to correlated pairs and triples of nucleons through the irreducible density matrices $\lambda^{(2)}$ and $\lambda^{(3)}$. It is noteworthy that the MR-IMSRG(2) flow equations do not depend on $\lambda^{(4)}$ or nonlinear powers of $\lambda^{(2)}$. While such contractions appear in the *products* of normal-ordered two-body operators, they cancel in the commutators (see appendix A). This ensures that the MR-IMSRG only sums so-called *connected* many-body diagrams (i.e., diagrams which do not contain intermediate insertions of the reference state) [69, 123].

Let us conclude this section by briefly considering the numerical implementation of the MR-IMSRG(2) scheme. The computational effort is dominated by the two-body flow equation (51), which naively requires $\mathcal{O}(N^6)$ operations, where N denotes the single-particle basis size. This puts the MR-IMSRG(2) in the same category as its aforementioned ‘cousins’ CCSD [57, 69], CTSD [70–72], and ICSE(2) [73–79], as well as the self-consistent Green’s function approaches (SCGF) [96, 97, 125–127]. Fortunately, the flow equations can be expressed in terms of matrix products and traces, allowing us to use optimized linear algebra libraries provided by high-performance computing vendors.

Moreover, we can reduce the computational cost in the single-reference case by distinguishing particle and hole states, because the number of hole states N_h is typically much smaller than the number of particle states $N_p \sim N$. The best scaling we can achieve in the IMSRG(2) depends on the choice of generator (see section 4.3). If the one- and two-body parts of the generator only consist of ph and pphhh type matrix elements (and their Hermitian conjugates), respectively, the scaling is reduced to $\mathcal{O}(N_h^2 N_p^4)$, which matches the cost of solving the CCSD amplitude equations.

4.2. Decoupling strategy

Having set up the flow equations in the previous section, we now need to specify our decoupling strategy, i.e., how we split the Hamiltonian into diagonal parts that we want to keep, and offdiagonal parts that we want to suppress through the MR-IMSRG evolution (see section 2). To do this, we refer to the matrix representation of the Hamiltonian in a given A -body basis, which is shown schematically for single- and multireference cases in figures 4 and 5, respectively. We stress that we do not actually need to construct the Hamiltonian matrix in this representation.

4.2.1. IMSRG decoupling in the single-reference case. Let us consider the simpler single-reference case first. We choose a Slater determinant reference and construct a basis by considering all possible particle–hole excitations (see section 3):

$$|\Phi\rangle, :A_h^p : |\Phi\rangle, :A_{hh'}^{pp'} : |\Phi\rangle, \dots \tag{54}$$

Note that $:A_{h_1 \dots h_i}^{p_1 \dots p_i} := A_{h_1 \dots h_i}^{p_1 \dots p_i}$ because contractions of particle and hole indices vanish by construction. Using Wick’s theorem, it is easy to see that the particle–hole excited Slater determinants are orthogonal to the reference state as

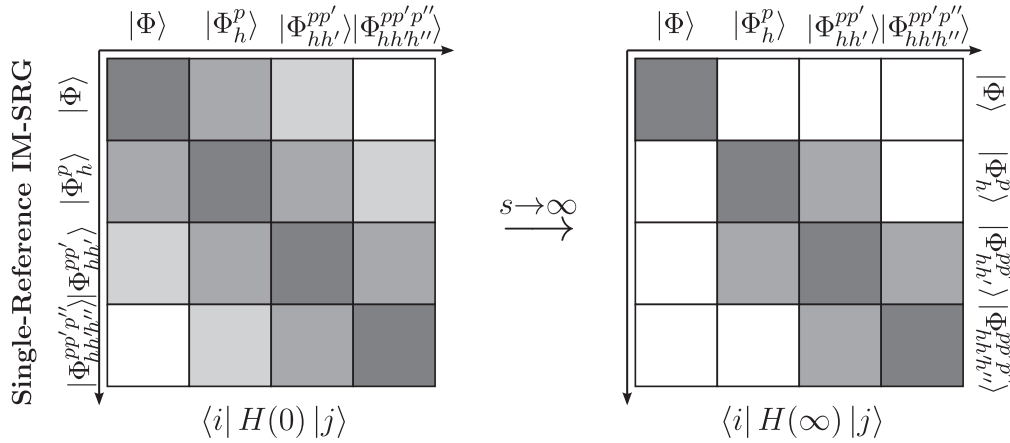


Figure 4. Schematic view of single-reference IMSRG decoupling in a many-body Hilbert space spanned by a Slater determinant reference $|\Phi\rangle$ and its particle-hole excitations $|\Phi_{hh'}^{pp'}\rangle$.

well as each other. In the Hilbert space spanned by this basis, the matrix representation of our initial Hamiltonian in the NO2B approximation (or any two-body operator) has the structure shown in the left panel of figure 4, i.e., it is band-diagonal, and can at most couple nph and $(n \pm 2)p(n \pm 2)h$ excitations.

We now have to split the Hamiltonian into appropriate diagonal and offdiagonal parts on the operator level, which is a non-trivial task (see, e.g., the extensive discussion in [128–130]). Using a broad definition of diagonality is ill-advised because we must avoid to induce strong in-medium $3N$, ... interactions to maintain the validity of the IMSRG(2) truncation. We choose what we call a *minimal decoupling scheme* that aims to decouple the one-dimensional block spanned by the reference state from all particle-hole excitations, as shown in the right panel of figure 4.

If we could implement this decoupling without approximations, we would extract a single eigenvalue and eigenstate of the many-body Hamiltonian for the nucleus of interest in the limit $s \rightarrow \infty$. The eigenvalue would simply be given by the zero-body piece of $H(\infty)$, while the eigenstate is obtained by applying the unitary IMSRG transformation to the reference state, $U^\dagger(\infty)|\Phi\rangle$. In practice, we end up with an approximate eigenvalue and mapping.

An important caveat is that we cannot guarantee *a priori* that we will target the true interacting ground state and its energy eigenvalue in this way. Empirically, the IMSRG flow is found to connect the reference state to the eigenstate with which it has the highest overlap. In single-reference scenarios, a HF Slater determinant will typically have the highest overlap with the exact ground state because it minimizes both the absolute energy and the correlation energy, the latter being due to admixtures from particle-hole excitations. In the multireference case, we have found examples where the MR-IMSRG flow targets excited states, as discussed in sections 6.3 and 7.4.

Analyzing the matrix elements between the reference state and its excitations with the help of Wick's theorem, we first see that the Hamiltonian couples the $0p0h$ block to $1p1h$

excitations through the matrix elements

$$\begin{aligned} \langle \Phi | H : A_h^p : | \Phi \rangle &= E \langle \Phi | : A_h^p : | \Phi \rangle + \sum_{ij} f_j^i \langle \Phi | : A_j^i : : A_h^p : | \Phi \rangle \\ &+ \frac{1}{4} \sum_{ijkl} \Gamma_{kl}^{ij} \langle \Phi | : A_{kl}^{ij} : : A_h^p : | \Phi \rangle \\ &= \sum_{ij} f_j^i \delta_h^i \delta_j^p n_i \bar{n}_j = f_p^h \end{aligned} \quad (55)$$

and their Hermitian conjugates. The contributions from the zero-body and two-body pieces of the Hamiltonian vanish because they are expectation values of normal-ordered operators in the reference state (see equation (28)). Likewise, the $0p0h$ and $2p2h$ blocks are coupled by the matrix elements

$$\langle \Phi | H : A_{hh'}^{pp'} : | \Phi \rangle = \Gamma_{pp'}^{hh'} \quad (56)$$

and their conjugates. It is precisely these two-body matrix elements that couple nph and $(n \pm 2)p(n \pm 2)h$ states and generate the outermost side diagonals of the Hamiltonian matrix. This suggests that we can transform the Hamiltonian to the shape shown in the top right panel of figure 4 by defining its offdiagonal part as

$$H_{\text{od}} \equiv \sum_{ph} f_h^p : A_h^p : + \frac{1}{4} \sum_{pp'hh'} \Gamma_{hh'}^{pp'} : A_{hh'}^{pp'} : + \text{h.c.} \quad (57)$$

In section 5, we will show that the IMSRG flow does indeed exponentially suppress the matrix elements of H_{od} and achieve the desired decoupling in the limit $s \rightarrow \infty$.

4.2.2. Variational derivation of minimal decoupling. Our minimal decoupling scheme is of course very reminiscent of the strategy followed in CC approaches [57, 69], except that we specifically use a unitary transformation instead of a general similarity transformation. It is also appealing for a different reason: as we will discuss now, it can be derived from a variational approach, tying the seemingly unrelated ideas of energy minimization and renormalization in the many-body system together. To this end, we consider the energy expectation value of the final IMSRG evolved

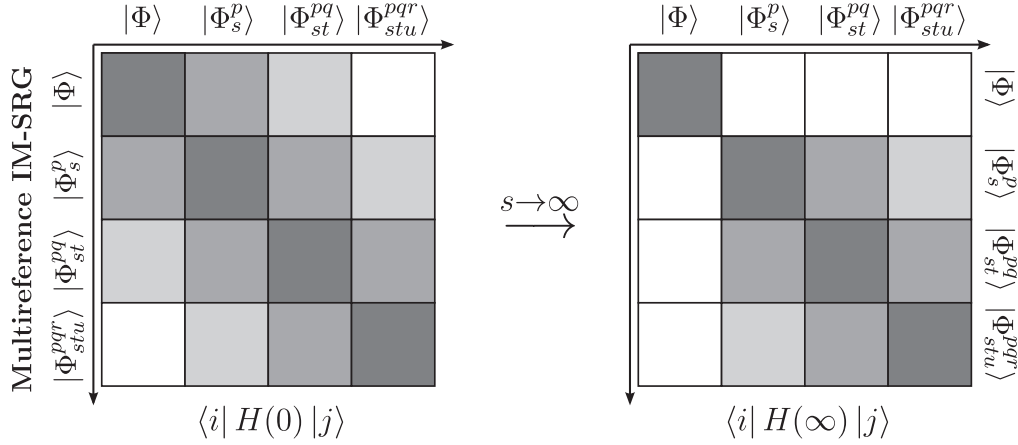


Figure 5. Schematic view of MR-IMSRG decoupling in the many-body Hilbert space. $|\Phi\rangle$ denotes an arbitrary reference state, and $|\Phi_{s,\dots}^p\rangle$ are suitably defined quasi-particle excitations.

Hamiltonian,

$$\bar{H} \equiv H(\infty), \quad (58)$$

in the reference state (which is assumed to be normalized):

$$E = \langle \Phi | \bar{H} | \Phi \rangle. \quad (59)$$

Next, we introduce a *unitary* variation, which we can choose to apply either to the reference state,

$$|\Phi\rangle \rightarrow e^Z |\Phi\rangle, \quad Z^\dagger = -Z, \quad (60)$$

or, equivalently, to the Hamiltonian:

$$e^{Z^\dagger} \bar{H} e^Z = e^{-Z} \bar{H} e^Z. \quad (61)$$

The variation of the energy is

$$\begin{aligned} \delta E &= \langle \Phi | e^{-Z} (\bar{H} - E) e^Z | \Phi \rangle = \langle \Phi | \bar{H} - E | \Phi \rangle \\ &+ \langle \Phi | [\bar{H} - E, Z] | \Phi \rangle + O(\|Z\|^2), \end{aligned} \quad (62)$$

with a suitable operator norm $\|\cdot\|$. The first term obviously vanishes, as does the commutator of Z with the energy. Thus, the energy is stationary if

$$\delta E = \langle \Phi | [\bar{H}, Z] | \Phi \rangle = 0. \quad (63)$$

Expanding

$$Z = \sum_{ph} Z_h^p : A_h^p : + \frac{1}{4} \sum_{pp'hh'} Z_{hh'}^{pp'} : A_{hh'}^{pp'} : + \text{h.c.} + \dots, \quad (64)$$

and using the independence of the expansion coefficients (save for the unitarity conditions), we obtain the system of equations

$$\langle \Phi | [\bar{H}, : A_h^p :] | \Phi \rangle = 0, \quad (65)$$

$$\langle \Phi | [\bar{H}, : A_p^h :] | \Phi \rangle = 0, \quad (66)$$

$$\langle \Phi | [\bar{H}, : A_{hh'}^{pp'} :] | \Phi \rangle = 0, \quad (67)$$

$$\langle \Phi | [\bar{H}, : A_{pp'}^{hh'} :] | \Phi \rangle = 0, \quad (68)$$

...

which are special cases of the so-called *irreducible Brillouin conditions (IBCs)* [75–78]. Writing out the commutator in the

first equation, we obtain

$$\begin{aligned} \langle \Phi | [\bar{H}, : A_h^p :] | \Phi \rangle &= \langle \Phi | \bar{H} : A_h^p : | \Phi \rangle \\ &- \langle \Phi | : A_h^p : \bar{H} | \Phi \rangle \\ &= \langle \Phi | \bar{H} : A_h^p : | \Phi \rangle = 0, \end{aligned} \quad (69)$$

where the second term vanishes because it is proportional to $n_p \bar{n}_h = 0$. The remaining equations can be evaluated analogously, and we find that the stationarity conditions are satisfied if the IMSRG evolved Hamiltonian \bar{H} no longer couples the reference state and its particle–hole excitations, as discussed above. This connection between the decoupling conditions and the stationarity conditions of an energy functional will prove useful in the multireference case.

4.2.3. MR-IMSRG decoupling for correlated reference states. In the multireference case, we choose a suitable correlated reference state, and construct its excitations by applying all possible one- and two-body operators:

$$|\Phi\rangle, : A_j^i : |\Phi\rangle, : A_{kl}^{ij} : |\Phi\rangle, \dots \quad (70)$$

The properties of the normal ordering ensure that the excited states are orthogonal to the reference state, but they are in general not orthogonal to each other: for instance,

$$\begin{aligned} \langle \Phi | : A_j^i : : A_l^k : | \Phi \rangle &= -\lambda_l^i \zeta_j^k + \lambda_{kl}^{ij} \\ &= n_i \bar{n}_j \delta_l^i \delta_j^k + \lambda_{kl}^{ij}, \end{aligned} \quad (71)$$

where $0 \leq n_i, \bar{n}_i \leq 1$. Moreover, there can be linear dependencies between the excitations of the correlated reference state, so the matrix representations of the Hamiltonian and other operators in this basis can be rank deficient. This poses a major challenge for multireference CC and related schemes that obtain solutions of the many-body Schrödinger equation by iterating a system of nonlinear equations. Numerical algorithms for solving systems of nonlinear equations fail if the Jacobian of the system is singular, and therefore one first must construct linearly independent excitations, e.g., through a costly diagonalization

of the overlap matrix. For the MR-IMSRG, in contrast, the linear dependencies merely imply that the flow is implicitly operating on a rank-deficient matrix that has additional spurious zero eigenvalues. These eigenvalues are usually far removed from the low-lying part of the spectrum that interests us most.

As shown in figure 5, the matrix representation of the initial NO2B Hamiltonian in the chosen excited states is again band-diagonal, just like in the single-reference case. Following the minimal decoupling approach discussed before, we want to transform the Hamiltonian to the shape that is shown in the right panel of figure 5, with

$$\langle \Phi | \bar{H} : A_j^i : | \Phi \rangle = 0, \quad (72)$$

$$\begin{aligned} \langle \Phi | \bar{H} : A_{kl}^{ij} : | \Phi \rangle &= 0, \\ &\dots \end{aligned} \quad (73)$$

and corresponding conditions for the conjugate matrix elements. The matrix elements can be evaluated with the generalized Wick's theorem (see section 3), e.g.,

$$\begin{aligned} \langle \Phi | H : A_j^i : | \Phi \rangle &= \bar{n}_i n_j f_i^j + \sum_{ab} f_b^a \lambda_{bj}^{ai} \\ &+ \frac{1}{2} \sum_{abc} (\bar{n}_i \lambda_{ja}^{bc} \Gamma_{ia}^{bc} - n_j \Gamma_{bc}^{ja} \lambda_{bc}^{ia}) \\ &+ \sum_{abcd} \frac{1}{4} \Gamma_{cd}^{ab} \lambda_{jcd}^{iab}. \end{aligned} \quad (74)$$

Note that the first term is merely the generalization of the one-body particle-hole matrix element, equation (55): in the single-reference limit, the occupation number prefactor is non-zero if i and j are particle and hole indices, respectively. In addition, the matrix element depends on the irreducible densities $\lambda^{(2)}$ and $\lambda^{(3)}$ in a non-trivial manner due to the coupling of the Hamiltonian to correlated pairs and triples of nucleons in the reference state. The matrix element between the reference state and the two-body excitation is even more complicated:

$$\begin{aligned} \langle \Phi | H : A_{kl}^{ij} : | \Phi \rangle &= \bar{n}_i \bar{n}_j n_k n_l \Gamma_{ij}^{kl} + (1 - P_{kl}) n_l \sum_b f_b^l \lambda_{bk}^{ij} \\ &- (1 - P_{ij}) \bar{n}_j \sum_a f_j^a \lambda_{kl}^{ai} \\ &+ \frac{1}{2} \bar{n}_i \bar{n}_j \sum_{ab} \Gamma_{ij}^{ab} \lambda_{kl}^{ab} + \frac{1}{2} n_k n_l \sum_{cd} \Gamma_{cd}^{kl} \lambda_{cd}^{ij} \\ &- (1 - P_{ij})(1 - P_{kl}) n_k \bar{n}_i \sum_{ad} \Gamma_{id}^{ak} \lambda_{dl}^{aj} \\ &+ \frac{1}{4} \sum_{abcd} \Gamma_{cd}^{ab} \lambda_{kl}^{ab} \lambda_{cd}^{ij} + \frac{1}{4} (1 - P_{ij}) \\ &\times \sum_{abcd} \Gamma_{cd}^{ab} (\lambda_{kl}^{aj} \lambda_{cd}^{bi} - \lambda_{cd}^{ai} \lambda_{kl}^{bj}) \\ &- \frac{1}{2} (1 - P_{kl}) \sum_{abcd} \Gamma_{cd}^{ab} \lambda_{ck}^{ab} \lambda_{dl}^{ij} \end{aligned}$$

$$\begin{aligned} &+ \frac{1}{2} (1 - P_{ij})(1 - P_{kl}) \sum_{abcd} \Gamma_{cd}^{ab} \lambda_{ck}^{ai} \lambda_{dl}^{bj} \\ &+ \sum_{ab} f_b^a \lambda_{bk}^{aij} + \frac{1}{2} (1 - P_{kl}) n_k \sum_{bcd} \Gamma_{cd}^{kb} \lambda_{cdl}^{bij} \\ &- \frac{1}{2} (1 - P_{ij}) \bar{n}_i \sum_{abd} \Gamma_{id}^{ab} \lambda_{dkl}^{abj} \\ &+ \frac{1}{4} \sum_{abcd} \Gamma_{cd}^{ab} \lambda_{cdkl}^{abij}, \end{aligned} \quad (75)$$

with the permutation symbol P_{ab} defined by (see appendix B)

$$P_{ij} g(\dots, i, \dots, j) \equiv g(\dots, j, \dots, i). \quad (76)$$

Again, only the first term appears in the single-reference limit. While the storage and manipulation of $\lambda^{(3)}$ is feasible for certain types of reference states, treating $\lambda^{(4)}$ is essentially out of the question. Thus, we are forced to introduce truncations in equations (74) and (75), and any decoupling we can achieve will no longer be exact, in general.

This is where the variational perspective introduced before becomes useful. Formally, we can write,

$$\begin{aligned} \langle \Phi | H : A_j^i : | \Phi \rangle &= \frac{1}{2} \langle \Phi | \{ H, : A_j^i : \} | \Phi \rangle \\ &+ \frac{1}{2} \langle \Phi | [H, : A_j^i :] | \Phi \rangle, \end{aligned} \quad (77)$$

$$\begin{aligned} \langle \Phi | H : A_{kl}^{ij} : | \Phi \rangle &= \frac{1}{2} \langle \Phi | \{ H, : A_{kl}^{ij} : \} | \Phi \rangle \\ &+ \frac{1}{2} \langle \Phi | [H, : A_{kl}^{ij} :] | \Phi \rangle, \end{aligned} \quad (78)$$

and suppress the second term in a clean and controlled manner through what amounts to a minimization of the ground-state energy through unitary variation. As discussed above, the energy is stationary if the IBCs for the multi-reference case are satisfied [75–78]:

$$\langle \Phi | [\bar{H}, : A_j^i :] | \Phi \rangle = 0, \quad (79)$$

$$\langle \Phi | [\bar{H}, : A_{kl}^{ij} :] | \Phi \rangle = 0. \quad (80)$$

Evaluating the commutators with the generalized Wick's theorem of section 3, we obtain

$$\begin{aligned} \langle \Phi | [H, : A_j^i :] | \Phi \rangle &= (n_j - \bar{n}_j) f_i^j \\ &- \frac{1}{2} \sum_{abc} (\Gamma_{bc}^{ja} \lambda_{bc}^{ia} - \Gamma_{ic}^{ab} \lambda_{jc}^{ab}), \end{aligned} \quad (81)$$

$$\begin{aligned} \langle \Phi | [H, : A_{kl}^{ij} :] | \Phi \rangle &= \Gamma_{ij}^{kl} (\bar{n}_i \bar{n}_j n_k n_l - n_i n_j \bar{n}_k \bar{n}_l) \\ &+ \sum_a ((1 - P_{ij}) f_i^a \lambda_{kl}^{aj} - (1 - P_{kl}) f_a^k \lambda_{al}^{ij}) \\ &+ \frac{1}{2} ((\lambda \Gamma)_{ij}^{kl} (1 - n_i - n_j) - (\Gamma \lambda)_{ij}^{kl} (1 - n_k - n_l)) \\ &+ (1 - P_{ij})(1 - P_{kl}) \sum_{ac} (n_j - n_k) \Gamma_{cj}^{ak} \lambda_{cl}^{ai} \\ &+ \frac{1}{2} \sum_{abc} ((1 - P_{kl}) \Gamma_{bc}^{ka} \lambda_{bcl}^{aij} - (1 - P_{ij}) \Gamma_{ic}^{ab} \lambda_{ckl}^{abj}). \end{aligned} \quad (82)$$

Like the MR-IMSRG(2) flow equations (49)–(51), these

expressions only depend linearly on $\lambda^{(2)}$ and $\lambda^{(3)}$, which makes untruncated implementations feasible.

By driving the Hamiltonian to a shape that satisfies the IBCs, we will achieve at least some reduction of the coupling between the reference state and excitations. The same also holds for the side diagonals to some extent, although they have a much richer structure than in the single-reference case. We also note that this is achieved by evolving the *individual* one-body and two-body pieces of the Hamiltonian, not just the specific linear combinations that enter into the decoupling conditions and IBCs. Thus, $\langle \Phi | \{H, : A_j^i : \} | \Phi \rangle$ and $\langle \Phi | \{H, : A_{kl}^{ij} : \} | \Phi \rangle$ will also be altered by the flow, and there is empirical evidence for their reduction. A detailed investigation will be presented elsewhere.

4.3. Generators

In the previous subsection we have specified the decoupling we want to achieve, leading us to a definition of the off-diagonal part of the Hamiltonian that must be suppressed by the MR-IMSRG evolution. However, we still have enormous freedom in choosing generators that implement this decoupling, especially if we are only interested in the limit $s \rightarrow \infty$ [61]. Here, we restrict ourselves to those generators that we found to be most useful in practical applications. Let us discuss the single-reference case first.

4.3.1. Construction of generators for single-reference applications. A wide range of suitable generators for the single-reference case is covered by the ansatz

$$\eta = \sum_{ph} \eta_h^p : A_h^p : + \frac{1}{4} \sum_{pp'hh'} \eta_{hh'}^{pp'} : A_{hh'}^{pp'} : - \text{h.c.}, \quad (83)$$

constructing the one- and two-body matrix elements directly from those of the offdiagonal Hamiltonian and an object G that ensures the anti-Hermiticity of η :

$$\eta_h^p \equiv G_h^p f_h^p, \quad (84)$$

$$\eta_{hh'}^{pp'} \equiv G_{hh'}^{pp'} \Gamma_{hh'}^{pp'}. \quad (85)$$

To see possible options for G , we consider the single-reference flow equations in perturbation theory (see [61] for a detailed discussion). We assume a HF reference state, and partition the Hamiltonian as

$$H = H_0 + gH_I, \quad (86)$$

with

$$H_0 \equiv E + \sum_i f_i^i : A_i^i : + \frac{1}{4} \sum_{ij} \Gamma_{ij}^{ij} : A_{ij}^{ij} :, \quad (87)$$

$$H_I \equiv \sum_{ij}^{i \neq j} f_j^i : A_j^i : + \frac{1}{4} \sum_{ijkl}^{ij \neq kl} \Gamma_{kl}^{ij} : A_{kl}^{ij} :. \quad (88)$$

In the space of up to 2p2h excitations, this corresponds to a second-quantized form of Epstein–Nesbet partitioning [131, 132], and treats the proper diagonal matrix elements in the aforementioned blocks of the Hamiltonian matrix as unperturbed. Note that the one-body piece of the initial Hamiltonian is diagonal in the HF orbitals, which implies

$f_h^p, \eta_h^p = 0$. Inspecting the one-body flow equation, we see that corrections to f that are induced during the flow are at least of order $\mathcal{O}(g^2)$, because no diagonal matrix elements of Γ appear:

$$\frac{d}{ds} f_j^i \Big|_{s=0} = \frac{1}{2} \sum_{abc} (\eta_{bc}^{ia} \Gamma_{ja}^{bc} - \Gamma_{bc}^{ia} \eta_{ja}^{bc}) \times (n_a \bar{n}_b \bar{n}_c + \bar{n}_a n_b n_c) = \mathcal{O}(g^2). \quad (89)$$

Using this knowledge, the two-body flow equation for the pphh matrix elements of the offdiagonal Hamiltonian reads

$$\begin{aligned} \frac{d}{ds} \Gamma_{hh'}^{pp'} &= - (f_p^p + f_{p'}^{p'} - f_h^h - f_{h'}^{h'}) \eta_{hh'}^{pp'} - (\Gamma_{hh'}^{hh'} + \Gamma_{pp'}^{pp'}) \eta_{hh'}^{pp'} \\ &\quad + (\Gamma_{p'h'}^{p'h'} + \Gamma_{ph}^{ph} + \Gamma_{ph'}^{ph'} + \Gamma_{p'h}^{p'h}) \eta_{hh'}^{pp'} + \mathcal{O}(g^2) \\ &= - \Delta_{hh'}^{pp'} \eta_{hh'}^{pp'} + \mathcal{O}(g^2). \end{aligned} \quad (90)$$

Note that the factors $\frac{1}{2}$ in the particle–particle and hole–hole ladder summation (line 2 of equation (51)) are canceled by factors 2 from the unrestricted summation over indices, e.g.,

$$\begin{aligned} &\frac{1}{2} \sum_{h_1 h_2} \eta_{h_1 h_2}^{pp'} \Gamma_{hh'}^{h_1 h_2} (1 - n_{h_1} - n_{h_2}) \\ &= - \frac{1}{2} \sum_{h_1 h_2} \eta_{h_1 h_2}^{pp'} (\Gamma_{hh'}^{hh'} \delta_{h_1}^{h_1} \delta_{h_2}^{h_2} + \Gamma_{hh'}^{hh'} \delta_{h_1}^{h_2} \delta_{h_2}^{h_1}) \\ &= - \eta_{hh'}^{pp'} \Gamma_{hh'}^{hh'}. \end{aligned} \quad (91)$$

In equation (90), we have introduced the quantity

$$\begin{aligned} \Delta_{hh'}^{pp'} &\equiv f_p^p + f_{p'}^{p'} - f_h^h - f_{h'}^{h'} + \Gamma_{hh'}^{hh'} + \Gamma_{pp'}^{pp'} \\ &\quad - \Gamma_{ph}^{ph} - \Gamma_{p'h'}^{p'h'} - \Gamma_{ph'}^{ph'} - \Gamma_{p'h}^{p'h} \\ &= \langle \Phi | : A_{pp'}^{hh'} : H : A_{hh'}^{pp'} : | \Phi \rangle - \langle \Phi | H | \Phi \rangle \\ &= \langle \Phi | : A_{pp'}^{hh'} : H_0 : A_{hh'}^{pp'} : | \Phi \rangle - \langle \Phi | H_0 | \Phi \rangle, \end{aligned} \quad (92)$$

i.e., the unperturbed energy difference between the two states that are coupled by the matrix element $\Gamma_{hh'}^{pp'}$, namely the reference state $|\Phi\rangle$ and the excited state $: A_{hh'}^{pp'} : |\Phi\rangle$. Since it is expressed in terms of diagonal matrix elements, $\Delta_{hh'}^{pp'}$ would appear in precisely this form in appropriate energy denominators of Epstein–Nesbet perturbation theory.

Plugging our ansatz for η into equation (90), we obtain

$$\frac{d}{ds} \Gamma_{hh'}^{pp'} = - \Delta_{hh'}^{pp'} G_{hh'}^{pp'} \Gamma_{hh'}^{pp'} + \mathcal{O}(g^2), \quad (93)$$

Neglecting $\mathcal{O}(g^2)$ terms in the flow equations, the one-body part of H remains unchanged, and assuming that G itself is independent of s at order $\mathcal{O}(g)$, we can integrate equation (90):

$$\Gamma_{hh'}^{pp'}(s) = \Gamma_{hh'}^{pp'}(0) e^{-\Delta_{hh'}^{pp'} G_{hh'}^{pp'} s}. \quad (94)$$

Clearly, the offdiagonal matrix elements of the Hamiltonian will be suppressed for $s \rightarrow \infty$, provided the product $\Delta_{hh'}^{pp'} G_{hh'}^{pp'}$ is positive. $G_{hh'}^{pp'}$ also allows us to control the details of this suppression, e.g., the decay scales. To avoid misconceptions, we stress that we do not impose perturbative truncations in practical applications, and treat all matrix elements and derived quantities, including the $\Delta_{hh'}^{pp'}$, as s -dependent.

4.3.2. The imaginary-time generator. Using $G_{hh'}^{pp'}$ to ensure that the energy denominator is always positive, we obtain the so-called *imaginary-time generator* [61, 91, 122], which is inspired by imaginary-time evolution techniques that are frequently used in quantum Monte Carlo methods, for instance (see, e.g., [133] and references therein). Explicitly indicating the flow parameter dependence of all quantities, we define

$$\eta^{\text{IT}}(s) \equiv \sum_{ph} \text{sgn}(\Delta_h^p(s)) f_h^p(s) : A_h^p : + \frac{1}{4} \sum_{pp'hh'} \text{sgn}(\Delta_{hh'}^{pp'}(s)) \Gamma_{hh'}^{pp'}(s) : A_{hh'}^{pp'} : - \text{h.c.}, \quad (95)$$

where

$$\Delta_h^p \equiv f_p^p - f_h^h + \Gamma_{ph}^{ph} = \langle \Phi | : A_p^h : H : A_h^p : | \Phi \rangle - \langle \Phi | H | \Phi \rangle. \quad (96)$$

For this generator, the perturbative analysis of the offdiagonal two-body matrix elements yields

$$\Gamma_{hh'}^{pp'}(s) = \Gamma_{hh'}^{pp'}(0) e^{-|\Delta_{hh'}^{pp'}|s}, \quad (97)$$

ensuring that they are driven to zero by the evolution. We also note that the energy difference $\Delta_{hh'}^{pp'}$ controls the scales of the decay. Matrix elements between states with large energy differences are suppressed more rapidly than those which couple states that are close in energy. This means that η^{IT} generates a proper RG flow [61, 63].

4.3.3. The White generator. A generator that is particularly powerful in numerical applications goes back to the work of White on CT theory in quantum chemistry [59, 61, 70]. In the language we have set up above, it uses $G_{hh'}^{pp'}$ to *remove* the scale dependence of the IMSRG flow. The White generator is defined as

$$\eta^{\text{W}}(s) \equiv \sum_{ph} \frac{f_h^p(s)}{\Delta_h^p(s)} : A_h^p : + \frac{1}{4} \sum_{pp'hh'} \frac{\Gamma_{hh'}^{pp'}(s)}{\Delta_{hh'}^{pp'}(s)} : A_{hh'}^{pp'} : - \text{h.c.}, \quad (98)$$

where the Epstein–Nesbet denominators use the energy differences defined in equations (92) and (96).

Referring again to our perturbative analysis of the offdiagonal two-body matrix elements, we find

$$\Gamma_{hh'}^{pp'}(s) = \Gamma_{hh'}^{pp'}(0) e^{-s}, \quad (99)$$

i.e., the White generator suppresses *all* offdiagonal matrix elements simultaneously with a decay scale identical (or close to) 1 [61]. While this means that η^{W} does *not* generate a proper RG flow, this is inconsequential if we are only interested in the final Hamiltonian $H(\infty)$, because all unitary transformations which suppress H_{od} must be equivalent up to truncation effects [61].

A benefit of the White generator is that its matrix elements are defined as ratios of energies, and therefore the

Hamiltonian only contributes linearly to the magnitude of the right-hand side of the flow equations (49)–(51). This leads to a significant reduction of the ODE system's stiffness compared to the other generators discussed here or in [61], and greatly reduces the numerical effort for the ODE solver. However, the dependence of η^{W} on energy denominators can also be a drawback if Δ_h^p and/or $\Delta_{hh'}^{pp'}$ become small, and cause some of its matrix elements to diverge. This can be mitigated by using an alternative ansatz that is also inspired by White's work [70]:

$$\eta^{\text{W}'}(s) \equiv \frac{1}{2} \sum_{ph} \arctan \frac{2f_h^p(s)}{\Delta_h^p(s)} : A_h^p : + \frac{1}{8} \sum_{pp'hh'} \arctan \frac{2\Gamma_{hh'}^{pp'}(s)}{\Delta_{hh'}^{pp'}(s)} : A_{hh'}^{pp'} : - \text{h.c.} \quad (100)$$

This form emphasizes that the unitary transformation can be thought of as an abstract rotation of the Hamiltonian. The matrix elements of $\eta^{\text{W}'}$ are regularized by the arctan function, and explicitly limited to the interval $]-\frac{\pi}{4}, \frac{\pi}{4}[$. Expanding the function for small arguments, we recover our initial ansatz for the White generator, equation (98).

4.3.4. Generators for the multireference case. The imaginary-time and White generators introduced in the previous subsections can be generalized to the multireference case by evaluating $\langle \Phi | H : A_j^i : | \Phi \rangle$, $\langle \Phi | H : A_{kl}^{ij} : | \Phi \rangle$ and the diagonal matrix elements $\langle \Phi | : A_i^j : H : A_j^i : | \Phi \rangle$, $\langle \Phi | : A_{ij}^{kl} : H : A_{kl}^{ij} : | \Phi \rangle$ that enter equations (96) and (92) with the Wick's theorem for correlated reference states. As we have seen in section 4.2, the offdiagonal matrix element, equation (75), depends on $\lambda^{(4)}$, and the diagonal matrix elements contain terms that are proportional to $\lambda^{(5)}$ and $\lambda^{(6)}$, in general. This forces us to introduce approximations that may adversely impact the behavior of the MR-IMSRG flow for the ground-state energy, e.g., by causing oscillations (see section 5.3 for an example).

In section 4.2.3, we argued that a formally cleaner approach can be devised where we forego the decoupling conditions (72) and (73) in favor of the IBCs (79) and (80), tying the MR-IMSRG flow to a variational minimization of the energy under unitary transformations. We define our so-called *Brillouin* generator as

$$\eta^{\text{B}} \equiv \sum_{ij} \eta_j^i : A_j^i : + \frac{1}{4} \sum_{ijkl} \eta_{kl}^{ij} : A_{kl}^{ij} :, \quad (101)$$

with the one- and two-body matrix elements given by

$$\eta_j^i \equiv \langle \Phi | [H, : A_j^i :] | \Phi \rangle = (n_j - n_i) f_j^i - \frac{1}{2} \sum_{abc} (\Gamma_{bc}^{ja} \lambda_{bc}^{ia} - \Gamma_{ic}^{ab} \lambda_{jc}^{ab}), \quad (102)$$

$$\begin{aligned}
\eta_{kl}^{ij} &\equiv \langle \Phi | [H, : A_{kl}^{ij} :] | \Phi \rangle \\
&= \Gamma_{ij}^{kl} (\bar{n}_i \bar{n}_j n_k n_l - n_i n_j \bar{n}_k \bar{n}_l) \\
&\quad + \sum_a ((1 - P_{ij}) f_i^a \lambda_{kl}^{aj} - (1 - P_{kl}) f_a^k \lambda_{ai}^{ij}) \\
&\quad + \frac{1}{2} ((\lambda \Gamma)_{ij}^{kl} (1 - n_i - n_j) - (\Gamma \lambda)_{ij}^{kl} (1 - n_k - n_l)) \\
&\quad + (1 - P_{ij})(1 - P_{kl}) \sum_{ac} (n_j - n_k) \Gamma_{cj}^{ak} \lambda_{cl}^{ai} \\
&\quad + \frac{1}{2} \sum_{abc} ((1 - P_{kl}) \Gamma_{bc}^{ka} \lambda_{bcl}^{aij} - (1 - P_{ij}) \Gamma_{ic}^{ab} \lambda_{ckl}^{abj}).
\end{aligned} \tag{103}$$

Like the MR-IMSRG(2) flow equations (49)–(51), η^B only depends on $\lambda^{(2)}$ and $\lambda^{(3)}$, and higher-rank irreducible density matrices appear only linearly.

Because the matrix elements of η^B are directly given by the residuals of the IBCs, it can be interpreted as the *gradient* of the energy with respect to the parameters of the unitary transformation at each step of the flow. At the fixed point of the flow, $\eta^B = 0$, and the flowing zero-body part of the Hamiltonian, $E(\infty)$, will be an extremum of the energy. Indeed, η^B has behaved in this manner in all numerical applications to date, generating a monotonic flow of the energy towards the converged results (see section 5.2).

We conclude this section by elucidating the relation between the Brillouin and imaginary-time generators. The multireference version of the latter has the matrix elements

$$\begin{aligned}
(\eta^{IT})_j^i &= \text{sgn}(\Delta_j^i) \langle \Phi | H : A_j^i : | \Phi \rangle \\
&\quad - \text{sgn}(\Delta_i^j) \langle \Phi | H : A_i^j : | \Phi \rangle^*,
\end{aligned} \tag{104}$$

$$\begin{aligned}
(\eta^{IT})_{kl}^{ij} &= \text{sgn}(\Delta_{kl}^{ij}) \langle \Phi | H : A_{kl}^{ij} : | \Phi \rangle \\
&\quad - \text{sgn}(\Delta_{ij}^{kl}) \langle \Phi | H : A_{ij}^{kl} : | \Phi \rangle^*.
\end{aligned} \tag{105}$$

Note that it is not possible to express Δ_j^i in terms of Δ_i^j , because they are matrix elements of the Hamiltonian in the unrelated states $: A_j^i : | \Phi \rangle$ and $: A_i^j : | \Phi \rangle$. The same is the case for the two-body excitation. However, if *all* basic excitations have higher energies than the reference state for all values of s , i.e., $\Delta_j^i, \Delta_{kl}^{ij} > 0$, the matrix elements read

$$\begin{aligned}
(\eta^{IT})_j^i &= \langle \Phi | H : A_j^i : | \Phi \rangle - \langle \Phi | H : A_i^j : | \Phi \rangle^* \\
&= \langle \Phi | H : A_j^i : | \Phi \rangle - \langle \Phi | : A_i^j : H | \Phi \rangle \\
&= \langle \Phi | [H, : A_j^i :] | \Phi \rangle,
\end{aligned} \tag{106}$$

$$(\eta^{IT})_{kl}^{ij} = \langle \Phi | [H, : A_{kl}^{ij} :] | \Phi \rangle, \tag{107}$$

and the Brillouin and imaginary-time generators are identical. Of course, is it difficult to ascertain in general that the condition $\Delta_j^i, \Delta_{kl}^{ij} > 0$ is satisfied in the multireference case. In the single-reference limit, on the other hand, the condition reduces to $\Delta_h^p, \Delta_{hh'}^{pp'} > 0$, which is typically satisfied if we start from HF reference states for nuclei with strong shell closures.

5. Features of IMSRG and MR-IMSRG flows

Before we launch into the discussion of prior and new MR-IMSRG ground state results in section 6, we want to illustrate some of the features of MR-IMSRG flows with concrete numerical examples. More details can also be found in [61].

5.1. Interactions and implementation

Let us start by providing some details on the implementation and typical interactions, for use both here and in later sections.

As made evident in section 3, we use the intrinsic nuclear Hamiltonian in our calculations, and employ interactions from chiral EFT both with and without free-space SRG evolution (section 2). Our primary choice for the NN sector is the $N^3\text{LO}$ interaction by Entem and Machleidt, with cutoff $\Lambda_{NN} = 500$ MeV/c [15, 134]. Unless specifically stated otherwise, this interaction will be supplemented by a local NNLO $3N$ interaction with cutoff $\Lambda_{3N} = 400$ MeV/c [90, 106]. This Hamiltonian, referred to as $NN + 3N(400)$ in the following, has been used widely in the *ab initio* nuclear structure literature in recent years, serving as the ‘parent’ for families of interactions that are generated by varying Λ_{NN} , Λ_{3N} and the SRG resolution scale λ .

The shortcomings of the $NN + 3N(400)$ Hamiltonian, e.g., the underestimation of nuclear charge radii or the overbinding of *pf*-shell nuclei (see section 6 and [56, 60, 91, 94, 98]), have sparked efforts to derive and optimize next-generation chiral forces [17–19, 25, 135–139]. In section 6, we will present MR-IMSRG results with one of the first new $NN + 3N$ interactions that resulted from these efforts, NNLO_{sat} [25]. By taking select many-body data into account in the optimization procedure, the creators of NNLO_{sat} were able to improve the interaction’s saturation properties, allowing an accurate description of the ground-state energies and radii of $^{40,48}\text{Ca}$ [140, 141].

We perform our calculations in a spherical harmonic oscillator configuration space, with a truncation in the energy quantum number:

$$e = (2n + l) \leq e_{\max}. \tag{108}$$

While mature techniques to extrapolate results to infinite HO bases are available [142–148], we limit ourselves to finite bases here, using sufficiently large e_{\max} values to eliminate the single-particle basis truncation as a relevant source of uncertainty, typically up to $e_{\max} = 14$ (15 major HO shells). An additional truncation is necessary to manage the enormous memory requirements of $3N$ interaction matrix elements. We only keep matrix elements involving three-body HO states that satisfy

$$e_1 + e_2 + e_3 \leq E_{3\max}. \tag{109}$$

For nuclei up to the calcium and nickel region, careful analyses have shown that it is sufficient to use $E_{3\max} = 14$ or 16 [56, 91] for soft interactions like $NN + 3N(400)$. These $E_{3\max}$ require ~ 5 GB and ~ 25 GB of memory, respectively, to store matrix elements in single precision. This exponential growth

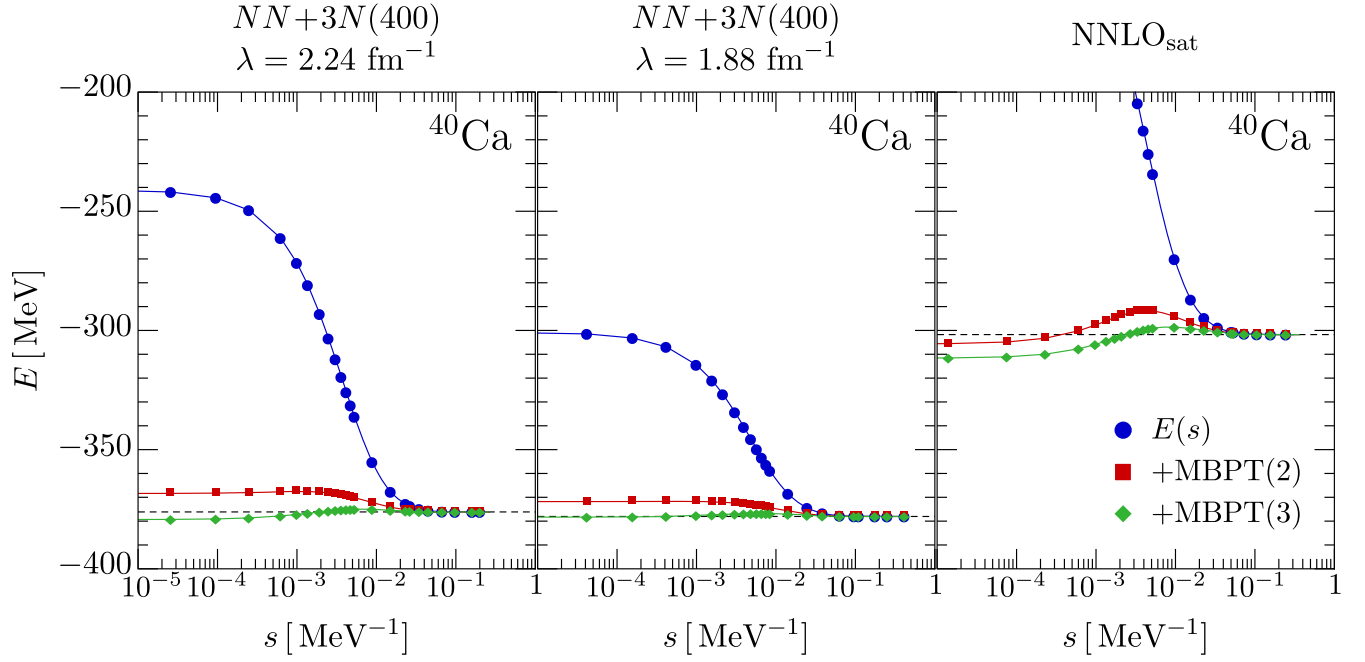


Figure 6. IMSRG(2) flow for ^{40}Ca using different chiral $NN+3N$ interactions, obtained with the single-reference version of the Brillouin generator, equation (101) ($e_{\text{max}} = 14$, $E_{3\text{max}} = 14$, optimal $\hbar\omega$). We show the flowing ground-state energy $E(s)$, and the sum of $E(s)$ and perturbative energy corrections evaluated with the flowing Hamiltonian $H(s)$, to illustrate the re-shuffling of correlations into the Hamiltonian (see text). The dashed lines indicate the final IMSRG(2) energies.

makes it challenging to push calculations to heavier nuclei, and it is clearly not feasible to store the entirety of the $3N$ interaction for a given e_{max} , which would require $E_{3\text{max}} = 3e_{\text{max}}$.

Reference states for closed- and open-shell nuclei are obtained by solving spherical HF and HFB equations, respectively, using the code described in [149]. In this calculation step, $3N$ interactions can be included exactly (up to e_{max} and $E_{3\text{max}}$ truncations). The HFB solutions are projected on good proton and neutron numbers, yielding a correlated state that must be treated in the multireference formalism. Details on the calculation of the irreducible density matrices of particle-number projected HFB states, referred to as *PNP reference states* in the following, can be found in appendix B.

With the reference state and its density matrices at our disposal, we normal-order the Hamiltonian using the techniques discussed in section 3, discard the residual $3N$ interaction, and eventually perform the IMSRG(2) or MR-IMSRG (2) evolution.

5.2. Ground-state calculations

As a first example, we consider IMSRG(2) ground-state calculations for the magic nucleus ^{40}Ca , using the single-reference version of the Brillouin η^{B} generator, equation (101), and different chiral $NN+3N$ interactions (figure 6). Globally, sizable amounts of correlation energy are re-shuffled into the zero-body piece of the Hamiltonian. We note that the specific size of these contributions changes significantly with the resolution scale. For $NN+3N(400)$ with $\lambda = 2.24 \text{ fm}^{-1}$, we gain about 130 MeV of binding. For the Hamiltonian with the lower resolution $\lambda = 1.88 \text{ fm}^{-1}$, the HF reference state is

already significantly lower in energy, so the energy gains from many-body correlations are less pronounced. This behavior is expected as interactions become increasingly soft, and thereby more perturbative (see, e.g., [32]). Note that the final ground-state energies for $\lambda = 2.24 \text{ fm}^{-1}$ and 1.88 fm^{-1} are almost identical, namely -376.1 MeV and -378.0 MeV . As discussed in section 2, in ideal implementations, all results should be invariant under arbitrary changes of λ , which appears to be satisfied to a high degree here. However, we caution that the $NN+3N(400)$ is tuned to minimize induced $4N, \dots$ forces [55, 90], so we have to reconsider the uncertainties due to these omitted terms for other interactions and observables (see, e.g., [150]).

In the rightmost panel of figure 6, we show the result of a calculation with NNLO_{sat} , which is considerably different from the $NN+3N(400)$ Hamiltonian. For instance, the HF ground-state energy of ^{40}Ca is merely -96.4 MeV , and the binding energy gain due to the IMSRG(2) evolution is about 200 MeV, which is a first indicator that its resolution scale is higher than that of the other two interactions used in the figure. The softened $NN+3N(400)$ Hamiltonians overestimate the binding energy compared to the experimental value of -342 MeV [108] (see section 6.2), and yield a charge radius of 3.0 fm, which is about 15% smaller than the experimental one [151]. In contrast, NNLO_{sat} is underbound at the IMSRG(2) level, and the charge radius is about 0.1 fm too large. In CC calculations with NNLO_{sat} , the binding energy at the CCSD(T) level is -326 MeV , [25], and we expect a comparable result from a similar approximate treatment of the next-level IMSRG truncation, denoted IMSRG (3). Work in this direction is in progress.

The mechanism by which the flowing ground-state energy is absorbing correlation energy can be understood if we consider the zero-body flow equation (49) in the perturbative approach we introduced in section 4.3. In the single-reference case, we have

$$\begin{aligned} \frac{dE}{ds} = & \underbrace{\sum_{ab} (n_a - n_b) \eta_b^a f_a^b}_{\mathcal{O}(g^4)} \\ & + \underbrace{\frac{1}{4} \sum_{abcd} (\eta_{cd}^{ab} \Gamma_{ab}^{cd} - \Gamma_{cd}^{ab} \eta_{ab}^{cd}) n_a n_b \bar{n}_c \bar{n}_d}_{\mathcal{O}(g^2)}. \end{aligned} \quad (110)$$

Assuming an imaginary-time (or Brillouin) generator, and recalling

$$\begin{aligned} \Gamma_{hh'}^{pp'}(s) &= \Gamma_{hh'}^{pp'}(0) e^{-|\Delta_{hh'}^{pp'}|s}, \\ \Gamma_{pp'}^{hh'}(s) &= \Gamma_{pp'}^{hh'}(0) e^{-|\Delta_{hh'}^{pp'}|s}, \end{aligned} \quad (111)$$

we have to $\mathcal{O}(g^2)$

$$\frac{dE}{ds} = \frac{1}{2} \sum_{pp'hh'} |\Gamma_{hh'}^{pp'}(0)|^2 e^{-2|\Delta_{hh'}^{pp'}|s}. \quad (112)$$

Integrating over the flow parameter, we obtain

$$E(s) = E(0) - \frac{1}{4} \sum_{pp'hh'} \frac{|\Gamma_{hh'}^{pp'}(0)|^2}{|\Delta_{hh'}^{pp'}|} (1 - e^{-2|\Delta_{hh'}^{pp'}|s}). \quad (113)$$

We recognize the second-order energy correction, evaluated with the initial Hamiltonian, and see that $E(s)$ will decrease with s (i.e., the binding energy increases). In the limit $s \rightarrow \infty$ the entire correction is shuffled into the zero-body piece of the evolved Hamiltonian. The complete IMSRG(2) obviously performs a more complex resummation of correlations, but we can see from figure 6 that it encompasses the complete second order. In fact, we see that the third-order correction is completely absorbed into the final $E(\infty)$ as well. An extensive discussion of how higher-order corrections are resummed can be found in [61] (also see [122]).

The perturbative analysis also gives us a rough understanding of the three characteristic regions in the flowing energy shown in figure 6. From $s = 0$ MeV⁻¹ to about $s = 10^{-3}$ MeV⁻¹, the energy is renormalized only weakly, followed by a rapid drop from 10^{-3} to 10^{-2} MeV⁻¹, and an eventual slow decay from 10^{-2} MeV⁻¹ onward. At a given value of s , the offdiagonal matrix elements that couple states with energy differences $\Delta_{hh'}^{pp'} = 1/s$ have been suppressed by a factor $1/e$. Thus the transitions in the energy flow occur when 2p2h excitations up to 1 GeV and 100 MeV, respectively, have been suppressed. For the softer $NN + 3N$ (400) interaction with $\lambda = 1.88$ fm⁻¹, the coupling between the reference state and such excitations is weaker than for $\lambda = 2.24$ fm⁻¹ (or NNLO_{sat}), and less correlation energy is gained by evolving.

As another example, we consider an MR-IMSRG(2) calculation for the semi-magic open-shell nucleus ⁴⁴Ca, using a PNP reference state and the $NN + 3N$ (400) Hamiltonian with $\lambda = 1.88$ fm⁻¹. In the top panel of figure 7, we show the flow of the ground-state energy for the multireference

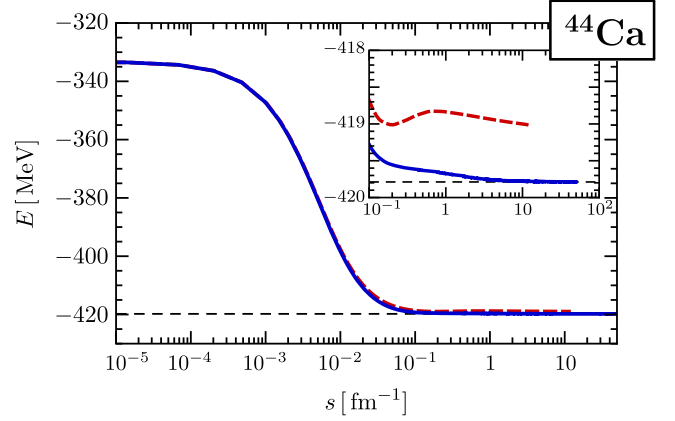


Figure 7. Flow of the MR-IMSRG(2) ground-state energy for ⁴⁴Ca, generated by the multireference Brillouin (equation (101), solid lines) and imaginary-time generators (equation (95), dashed lines). In the latter, $\chi^{(k \geq 2)}$ terms have been truncated (see text). Both calculations use the chiral $NN + 3N$ (400) Hamiltonian, SRG-evolved to $\lambda = 1.88$ fm⁻¹ (see section 5.1), a PNP reference state, and a single-particle basis of 15 major HO shells ($e_{\max} = 14$, $\hbar\omega = 24$ MeV).

Brillouin generator η^B , and an approximate version of the multireference imaginary-time generator where terms involving $\chi^{(k \geq 2)}$ have been truncated. Superficially, the flow of the energy is similar to the ⁴⁰Ca single-reference examples discussed above, and the two generators seem to perform equally well. However, the inset in the panel reveals differences for $s > 0.1$ MeV⁻¹. The flow generated by η^B is causing a monotonic decrease of the energy, while the approximate η^{IT} exhibits oscillatory behavior. These oscillations die out if we evolve to sufficiently large s , and a converged energy of -419.0 MeV is obtained, compared to -419.8 MeV for the Brillouin generator. The inclusion of the terms that are linear in $\chi^{(2)}$ and $\chi^{(3)}$ removes the oscillation and brings the η^{IT} flow in agreement with η^B , suggesting that the sign factors are consistently positive and the relation (107) holds. Terms that are quadratic in $\chi^{(2)}$ or linear in $\chi^{(4)}$ cancel.

5.3. Decoupling

In section 4.2, we discussed in detail how we have to define the offdiagonal Hamiltonian to ensure that the reference state is decoupled from excitations by the (MR-)IMSRG flow. Let us now demonstrate that the matrix elements in question are indeed suppressed as intended. Since only approximate decoupling can be achieved in the multireference case if we want to avoid the extremely costly inclusion of irreducible density matrices $\chi^{(k \geq 4)}$, we use a single-reference calculation for ⁴⁰Ca as our example. For this doubly magic nucleus, we can use the White generator, equation (98). Based on our perturbative analysis in section 4.3, we expect offdiagonal matrix elements to decay according to

$$\Gamma_{hh'}^{pp'}(s) = \Gamma_{hh'}^{pp'}(0) e^{-s} \quad (114)$$

(note that the flow parameter is dimensionless for the White generator).

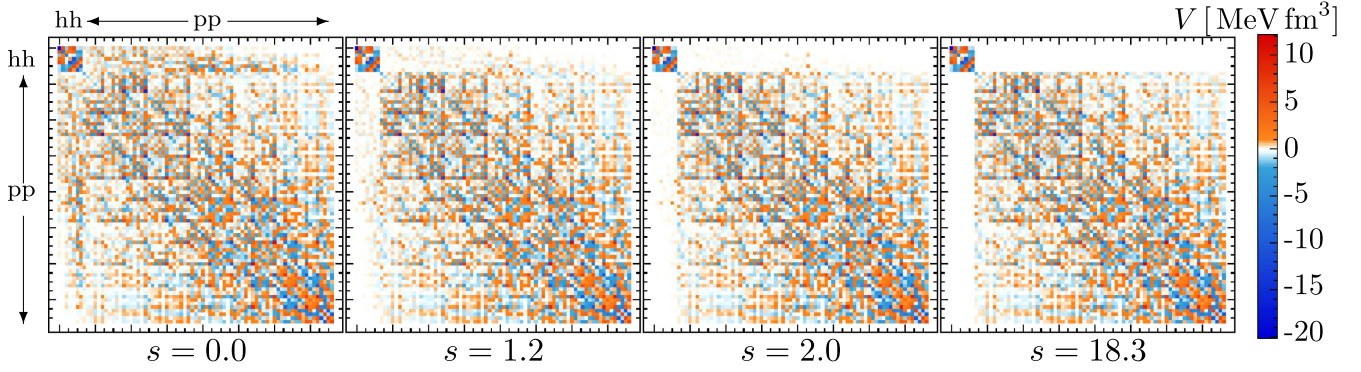


Figure 8. Decoupling for the White generator, equation (98), in the $J^\pi = 0^+$ neutron–neutron interaction matrix elements of ^{40}Ca ($e_{\text{max}} = 8$, $\hbar\omega = 20$ MeV, Entem–Machleidt N^3 LO(500) evolved to $\lambda = 2.0$ fm $^{-1}$, no induced or initial $3N$ forces). Only hhhh, hhpp, pphh, and pppp blocks of the matrix are shown.

In figure 8, we show the pppp, hhhh, pphh and hhpp matrix elements of the normal-ordered Hamiltonian in the $J^\pi = 0^+$ neutron–neutron partial wave (the phph and hphh matrix elements are omitted to avoid clutter). As we integrate the IMSRG(2) flow equations, the offdiagonal matrix elements ($\Gamma_{hh'}^{pp'}$ and $\Gamma_{pp'}^{hh'}$) are suppressed rapidly, as suggested by equation (114). We stop the evolution at $s = 18.3$, where the second-order energy correction calculated with $H(s)$, falls below 10^{-6} MeV.

5.4. Effective Hamiltonians

With the suppression of pphh and hhpp matrix elements, the matrix representation of the Hamiltonian in our many-body Hilbert space is driven to the simplified form shown in figure 4, eliminating the outermost diagonals that are coupling nph and $(n \pm 2)p(n \pm 2)h$ excitations. In the MR-IMSRG, we can at least reduce the strength of the couplings between generalized excitations. At any finite value of s , correlations due to such couplings have been reshuffled into the *diagonal* Hamiltonian. Thus, we can also view the MR-IMSRG as a tool to generate RG-improved effective Hamiltonians, analogous to the free-space SRG discussed in section 2.

Formally, all quantum many-body methods either implicitly or explicitly approximate the eigenvalues and eigenvectors of an initial Hamiltonian that are given by

$$H(0) |\Psi_n\rangle = E_n |\Psi_n\rangle. \quad (115)$$

For an ‘exact’ method like FCI, the only approximation is the use of a finite basis to represent the Hamiltonian matrix, while approaches like CI, CC or MR-IMSRG also introduce systematic truncations. Let us write the approximate eigenvalues and eigenstates of a real many-body calculation as

$$H(0) |\Phi_n\rangle = E'_n |\Phi_n\rangle, \quad |\Phi_n\rangle \approx |\Psi_n\rangle, E'_n \approx E_n. \quad (116)$$

The eigenvalues are invariant under a unitary transformation, e.g., an untruncated MR-IMSRG evolution,

$$\begin{aligned} H(s)U(s) |\Psi_n\rangle &\equiv U(s)HU^\dagger(s)U(s) |\Psi_n\rangle \\ &= E_n U(s) |\Psi_n\rangle. \end{aligned} \quad (117)$$

Thus, it may be fruitful to use an effective Hamiltonian that has absorbed many-body correlations, e.g., through IMSRG

or MR-IMSRG improvement, as input for a quantum many-body calculation. In this case, the many-body method would need to approximate the transformed eigenstate,

$$|\Phi_n\rangle \approx U(s) |\Psi_n\rangle \quad (118)$$

instead of $|\Psi_n\rangle$, which may be a less demanding task. For example, the momentum-space decoupling achieved by the free-space SRG allows us to use low-energy (low-momentum) model spaces to accurately describe low-lying nuclear spectra (see section 2). Similarly, the IMSRG can be used to build correlations into the Hamiltonian that are not accessible by a truncated many-body method, improving the quality of the approximation (118). Examples are a CI method with up to nph excitations that can probe $(n+2)p(n+2)h$ excitations if an IMSRG(2) Hamiltonian is used (see section 4.2), the physics of the inert core and excluded space in the interacting shell model/valence-space CI (see section 7), or excitations beyond a specific N_{max} model space used in the NCSM [152].

For numerical illustration, we use the IMSRG Hamiltonian $H(s)$ from a single-reference ground-state calculation of ^{40}Ca as input for second-order MBPT (denoted MBPT(2)) and CC with singles and doubles excitations (CCSD, [69]), as well as non-iterative triples corrections (Λ -CCSD(T), [153, 154]). The resulting ground-state energies are compared to the flowing IMSRG(2) energy in figure 9. Once we reach $s = 2.0$, the offdiagonal matrix elements of the Hamiltonian have been strongly suppressed (see figure 8), and the ground-state energies of all methods collapse to the same result, namely the IMSRG(2) ground-state energy. The CC results can be viewed as an extension of our discussion of figure 6, showing that for $s > 2.0$ there is practically no more correlation energy to be gained from MBPT corrections, not even when terms are summed to infinite order.

While the FCI ground-state energy is independent of s under exact IMSRG transformations of the Hamiltonian (also see section 2), we have to carefully assess the interplay of all practical truncations if we use IMSRG evolved Hamiltonians as an input for non-exact many-body methods [61]. If an approximate many-body method is less complete than the IMSRG in a specific truncation, we will obtain an RG improvement towards the exact result, as discussed above.

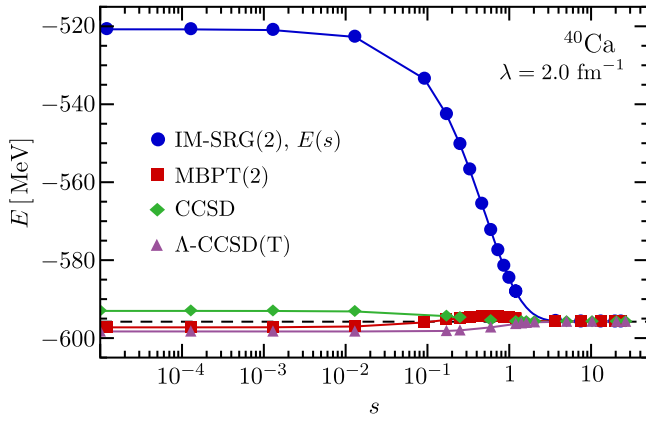


Figure 9. IMSRG(2) ground-state energy of ^{40}Ca as a function of the flow parameter s , compared to MBPT(2), CCSD, and Λ -CCSD(T) energies with the IMSRG-evolved Hamiltonian $H(s)$. We only show part of the data points to avoid clutter. Calculations were done for $e_{\text{max}} = 10$ and optimal $\hbar\omega = 24$ MeV, using our standard N^3LO interaction (see section 5.1) at $\lambda = 2.0$ fm^{-1} , without initial or induced $3N$ forces. The dashed lines indicate the final IMSRG(2) energies.

However, if the many-body method contains terms beyond the truncated IMSRG, the final result can be an inferior approximation of the true eigenvalue and eigenstate than the one obtained with the unevolved Hamiltonian. Figure 9 contains examples for both cases: MBPT(2) is less complete than the IMSRG(2), so the MBPT(2) energy is improved towards the exact energy. Note that the improvement in the energy can amount to an attractive or a repulsive correction, depending on the initial Hamiltonian. For soft interactions like the one used here, MBPT(2) tends to provide too much binding [32, 50, 51, 59, 155–158], hence the final IMSRG(2) ground-state energy increases (the binding energy decreases). On the other hand, the Λ -CCSD(T) energy contains fourth-order 3p3h (triples) correlations that are missing in the IMSRG(2) [61], hence it is a better approximation to the true ground-state energy of the initial Hamiltonian than the result obtained with the IMSRG(2) Hamiltonian for large s .

In general, the capability to ‘split’ correlations between the wave function and the effective Hamiltonian can be used to greatest effect if complementary types of correlations are handled better by each ingredient. For instance, reference states that are projected from symmetry-broken mean fields offer a very efficient way to capture *static correlations* that would require an explicit treatment of up to $A\rho A$ (or generalized A -body) excitations in the many-body bases we have discussed so far. Conversely, these latter bases are well-suited for the description of *dynamical correlations* (i.e., the dynamics of nucleon pairs, triples, ...) inside the nucleus. The MR-IMSRG offers us a framework that can harness both types of correlations, by building dynamical correlations on top of statically correlated reference states. A concrete example are the calculations based on PNP reference states discussed above and in section 6.

6. Ground-state calculations for closed- and open-shell nuclei

In recent years, we have applied the MR-IMSRG to study the ground-state energies of semi-magic isotopic chains and gauge the quality of chiral interactions like $NN + 3N(400)$ through their confrontation with experimental data [54, 60, 91]. We will review the salient findings of these investigations in the following, using the opportunity to repeat the MR-IMSRG(2) calculations with the Brillouin generator (101) instead of our earlier choices. Thus, the present work serves as a benchmark for the new generator. The outcome of this benchmark process can be anticipated based on our discussion in sections 4.3 and 5.2: Results obtained with η^B agree with those for (approximate) multireference imaginary-time and White generators on the level of 0.1%–0.2%, which is currently a negligible contribution to the uncertainties of our calculations. On the many-body side, these uncertainties are due to truncation effects (i.e., the omission of three- and higher-body terms that are induced by the MR-IMSRG flow) and the NO2B approximation. As discussed in [54, 60, 91] and the remainder of this section, these uncertainties can be quantified and controlled reasonably well, so that the main sources of uncertainty are the input Hamiltonian and the impact of changing the resolution scale λ .

6.1. Oxygen isotopes

The oxygen isotopic chain has become a testing ground for *ab initio* nuclear structure methods in recent years [54, 90, 127, 159–165], mainly for two reasons: first, Otsuka *et al* [160] showed the impact of $3N$ forces on the location of the neutron drip line, and second, exact results from the importance-truncated NCSM (IT-NCSM) [55, 90, 166, 167] are available for the ground states and low-lying excitations, allowing us to assess the many-body uncertainties of our calculations.

The semi-magicity of the oxygen isotopes also allows us to enforce spherical symmetry in our calculations to boost the numerical efficiency. For instance, an IMSRG(2) calculation for a closed-shell oxygen isotope, using a spherical HF reference state and 15 major HO shells, requires about 20 core hours on current high-performance computing hardware. An MR-IMSRG(2) calculation for an open-shell isotope, based on a spherical PNP reference state, takes about 500–1000 core hours to converge. In contrast, an IT-NCSM calculation requires on the order of 100 000 core hours for neutron-rich oxygen nuclei [54].

In figure 10, we compare MR-IMSRG(2) results for the oxygen ground-state energies with a variety of configuration-space many-body methods. In addition to IT-NCSM, CCSD, and Λ -CCSD(T) (see 5.4), we also include results from the SCGF approach in the ADC(3) scheme [127, 159]. The latter are obtained at a slightly different resolution scale $\lambda = 2.0$ fm^{-1} , but the dependence of the ground-state

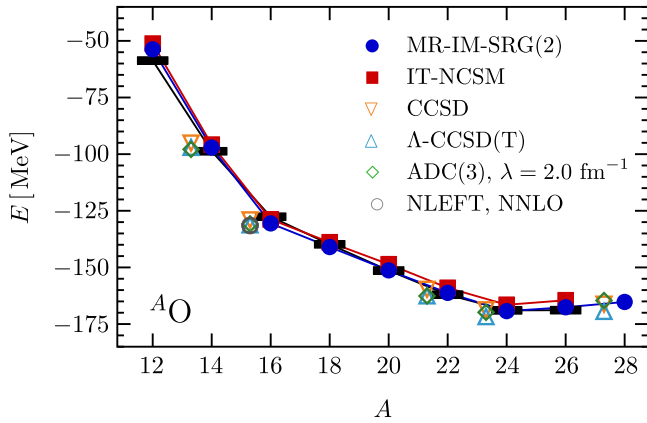


Figure 10. Ground-state energies of the oxygen isotopes from MR-IMSRG(2) and other many-body approaches, using the $NN + 3N(400)$ interaction at $\lambda = 1.88 \text{ fm}^{-1}$. Some data points were offset horizontally to enhance the readability of the figure. MR-IMSRG(2) calculations were performed using the Brillouin generator ($e_{\text{max}} = 14$, $E_{3\text{max}} = 14$, and optimal $\hbar\omega$), updating earlier results shown in [54, 61]. Note that the ADC(3) self-consistent Green's function results [127, 159] were obtained for $\lambda = 2.0 \text{ fm}^{-1}$, but the dependence of energies on λ is very weak. Black bars indicate experimental data [108].

energies on λ is very weak, at least in the range $\lambda = 1.88, \dots, 2.24 \text{ fm}^{-1}$. For example, the ground-state energy of ^{24}O changes by 0.2% under this variation (see figure 11). The insensitivity of the ground-state energies to variations of λ is due to a cancellation of $4N$ forces that are induced by lowering the resolution scale of the initial NN and $3N$ forces, respectively (see section 5.2 and [54, 94]). We will illustrate below that this tuning does not hold for general observables.

For the same $NN + 3N(400)$ input Hamiltonian, all used methods give consistent results that agree within a few percent with experimental ground state energies. The systematically truncated methods, i.e., MR-IMSRG(2), CCSD, Λ -CCSD(T) and ADC(3), agree very well with the exact IT-NCSM results, on the level of 1%–2%. Since the IT-NCSM includes the complete $3N$ interaction, in accordance with its model space truncation, this deviation is due to the combined effects of the NO2B approximation [93, 94, 119], as well as truncated many-body correlations. The Λ -CCSD(T) method gains about 2% of additional binding energy compared to CCSD through the inclusion of triples correlations, giving us an in-method measure of the scheme's many-body uncertainty, and indicating the rapid convergence of the many-body expansion for low-momentum Hamiltonians [32, 49, 50]. However, this particular CC method is known to over-predict ground-state energies in quantum chemistry compared to exact diagonalization methods like FCI, which is the counterpart to the IT-NCSM in our case. For this reason, improved triples approaches like the completely renormalized CR-CC (2, 3) scheme have been introduced in the literature [119, 168], which we will use for comparison in section 6.2. For an approximate or complete implementation of MR-IMSRG(3), we can expect binding energy gains of

comparable size because it will probe dynamical correlations due to nucleon triples in a similar fashion. For more details, we refer the reader to the in-depth analysis published in [61].

The MR-IMSRG(2) ground-state energy of ^{16}O , -130.1 MeV , also agrees well with the result of a recent nuclear lattice EFT (NLEFT) calculation, which is $-131.3(5) \text{ MeV}$. This ground-state energy is obtained with an NNLO Lagrangian, including NN and $3N$ interactions, as well as a tuned regularized $4N$ contact force [162]. The net effect of the $4N$ term is repulsive; without it, the ground-state energy is $-138.8(5) \text{ MeV}$. Since the treatment of the nuclear many-body problem in NLEFT is completely different from all the other approaches compared here [169], the consistency of the results for comparable inputs is very encouraging.

The *ab initio* calculations clearly predict the neutron drip line at ^{24}O , matching experimental findings [170]. While absolute ground-state energies can change significantly under variations of the $3N$ cutoffs or other modifications of the initial Hamiltonian, the drip line signal turns out to be rather robust [54]. All methods predict the ^{26}O resonance at an energy $E_x \approx 1 - 2 \text{ MeV}$ above the ^{24}O ground state, which is considerably higher than the current experimental limits $E_x \approx 50 \text{ keV}$ [171–173]. In part, this is due to the omission of continuum effects in all calculations that are shown here. However, we also see indications that while the $NN + 3N(400)$ Hamiltonian reproduces the ground-state energy trends along the isotopic chain quite well, it enhances certain shell closures compared to experiment. This causes an overestimation of the experimental ^{16}O binding energy, for instance. We will find further examples of enhanced shell closures in other isotopic chains. The interplay of nuclear interactions, many-body and continuum effects that causes the flat trend of the experimental ground-state resonance energies beyond ^{24}O suggests that the oxygen isotopes will remain an important testing ground for nuclear Hamiltonians and many-body methods for the foreseeable future.

While $NN + 3N(400)$ gives a good reproduction of the oxygen ground-state energies, an issue with the Hamiltonian's saturation properties is revealed by inspecting the oxygen charge radii (see figure 11). The theoretical charge radii are about 10% smaller than the experimental charge radius of ^{16}O , $R_{\text{ch}} = 2.70 \text{ fm}$ [151], and the sharp increase for ^{18}O is missing entirely.

The underestimation of nuclear radii was one of the deficiencies that inspired efforts by multiple groups to improve the construction and optimization of chiral interactions. One of the first new interactions to come out of these efforts is NNLO_{sat} by Ekström and collaborators [25]. As the name suggests, it is defined at chiral order NNLO, and contains NN and $3N$ interactions. The creators of this interaction chose to include select many-body data in the optimization protocol for the interaction's LECs, including the ^{16}O ground-state energy and charge radius. Note that perfect agreement with experimental data is not enforced, because the optimization procedure aims to account for uncertainties due to truncation at chiral order NNLO, and the many-body approach used for accessing the medium-mass nuclei (CCSD).

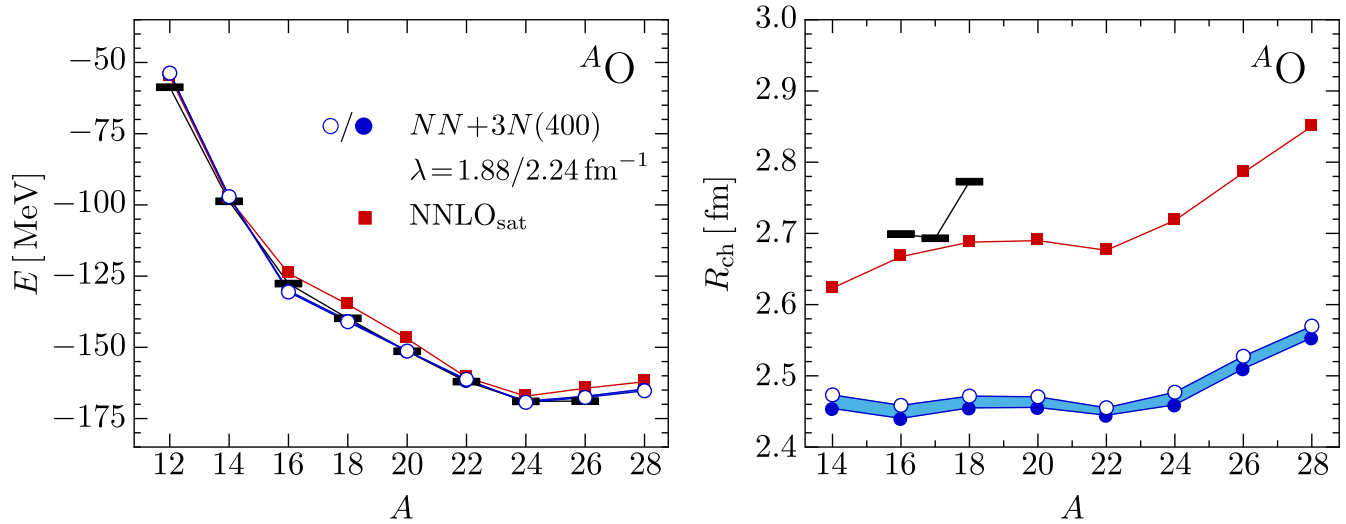


Figure 11. MR-IMSRG(2) ground-state energies and charge radii of the oxygen isotopes for $NNLO_{\text{sat}}$ and $NN+3N(400)$ at $\lambda = 1.88, \dots, 2.24 \text{ fm}^{-1}$ ($e_{\text{max}} = 14$, $E_{3\text{max}} = 14$, and optimal $\hbar\omega$). Black bars indicate experimental data [108, 151].

In figure 11, we compare MR-IMSRG(2) results for $NNLO_{\text{sat}}$ and $NN+3N(400)$. For the latter, we indicate the effects of varying λ from 1.88 fm^{-1} to 2.24 fm^{-1} through a shaded band. As discussed above, the ground-state energies only vary by 0.2% due to a fine-tuned cancellation, but the change in the radii is as large as 1%. Interestingly, R_{ch} grows larger as λ decreases. This is consistent with a recent study in light nuclei [174], which also found that two- and three-body terms that are induced by consistently evolving the charge radius operator to lower λ have the opposite effect and *reduce* its expectation value. These terms have not been included here.

The MR-IMSRG(2) ground-state energies obtained with $NNLO_{\text{sat}}$ are slightly *lower* than those for $NN+3N(400)$ in the proton-rich isotopes $^{12,14}\text{O}$, and above the $NN+3N(400)$ energies in $^{16-28}\text{O}$. From $^{16-22}\text{O}$, the $NNLO_{\text{sat}}$ ground-state energies exhibit a parabolic behavior as opposed to the essentially linear trend we find for $NN+3N(400)$. A possible cause is the inclusion of the $^{22,24}\text{O}$ ground-state energies in the optimization protocol, which constrains the possible energy deviation in these nuclei. $NNLO_{\text{sat}}$ predicts the drip line at ^{24}O , and the trend for the $^{26,28}\text{O}$ resonance energies is similar to the $NN+3N(400)$ case.

For $NNLO_{\text{sat}}$, the charge radii for the bound oxygen isotopes are about 10% larger than for $NN+3N(400)$, which is expected given the use of the ^{16}O charge radius in the optimization of the LECs (also see [175]). For the resonant states, the increase is even larger, but continuum effects must be considered to make a meaningful comparison. We note that $NNLO_{\text{sat}}$ also fails to describe the sharp jump in R_{ch} at ^{18}O .

6.2. Calcium and nickel isotopes

In [91], we applied the MR-IMSRG(2) to study the ground-state energies of calcium and nickel isotopes. As for the oxygen isotopes reviewed in the previous subsection, we

exploited the semi-magicity of these nuclei and enforced spherical symmetry in our calculations. Figure 12(a) shows the MR-IMSRG(2) ground-state energies for the calcium isotopic chain. The deficient saturation properties of the $NN+3N(400)$ interaction are now fully apparent, causing an overbinding compared to experiment that increases from 8% to 12% along the known isotopes $^{36,54}\text{Ca}$. In nuclei with sub-shell closures, the MR-IMSRG(2) energies are consistent with results from CCSD and CR-CC(2, 3) calculations with the same Hamiltonian, just as in the oxygen case. The ground-state energy gains from the inclusion of triples are on the order of 2% for the Hamiltonian used here, which can serve as an indicator of the uncertainty due to the many-body truncation. The energies are insensitive to variations of the resolution scale λ in a window around 2.0 fm^{-1} , which suggests that the cancellation of induced $4N$ interactions works as in the oxygen chain. The residual changes are about 0.2% for MR-IMSRG(2), 2% for CCSD, and 1% for CR-CC(2, 3).

The presence of the $3N$ force in our Hamiltonian causes the appearance of a flat trend in the ground-state energies beyond ^{54}Ca [91]. Similar behavior was found in CC calculations that used a more phenomenological treatment of the $3N$ force, normal ordering it in symmetric nuclear matter to derive the in-medium contributions to lower-rank parts of the Hamiltonian, and readjusting the LECs [177]. It will be interesting to see if this trend will be confirmed experimentally in the coming years, since it would have strong implications for the location of the neutron drip line in calcium.

In figure 12(b), we show the MR-IMSRG(2) results for the two-neutron separation energies, defined as

$$S_{2n}(Z, N) \equiv E(Z, N-2) - E(Z, N). \quad (119)$$

Despite the overestimation of the calcium binding energies, the $NN+3N(400)$ Hamiltonian gives a reasonable reproduction of the experimental trends. Most notably, the major shell closure at the magic neutron number $N=20$ is too pronounced, continuing behavior we saw in the oxygen

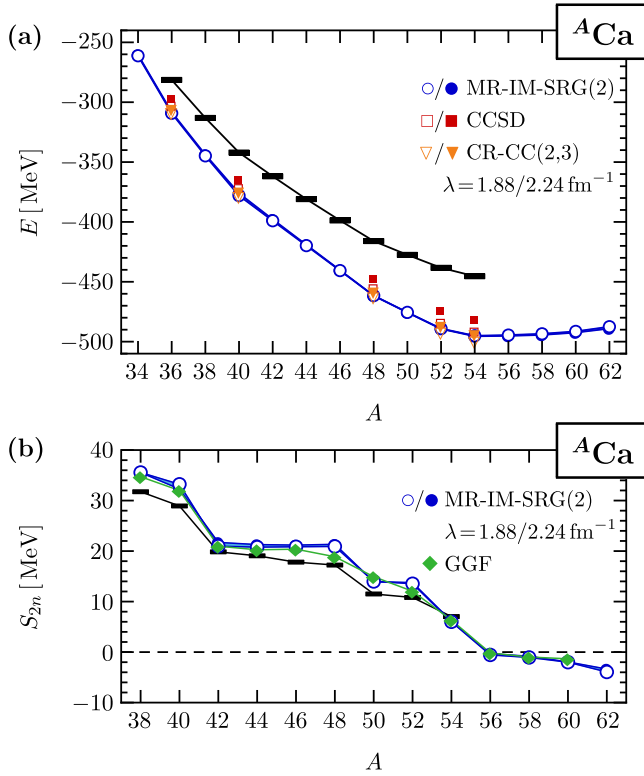


Figure 12. MR-IMSRG(2) ground-state energies (top) and two-neutron separation energies (bottom) of the calcium isotopes, for the $NN+3N(400)$ Hamiltonian with $\lambda = 1.88, \dots, 2.24 \text{ fm}^{-1}$ ($e_{\text{max}} = 14$, $E_{3\text{max}} = 14$, optimal $\hbar\omega$). All calculations were performed with the Brillouin generator, updating the previous work [91]. For nuclei with neutron sub-shell closures, we show ground-state energies from CCSD and CR-CC(2, 3) calculations for comparison (see text and [56, 119]). Two-neutron separation energies are compared to results from self-consistent second-order Gor'kov Green's function (GGF) calculations with the $NN+3N(400)$ Hamiltonian at $\lambda = 2.0 \text{ fm}^{-1}$ [91, 98]. Black bars indicate experimental data [108, 176].

isotopes. The drops in the theoretical S_{2n} in ${}^{48,52,54}\text{Ca}$, corresponding to the hypothetical shell closures $N = 28, 32, 34$, suggests that these nuclei are magic for the used interaction, matching predictions from shell model calculations with interactions derived from chiral $NN+3N$ forces in MBPT [178, 179]. While this view was supported by precision mass measurements [176, 180, 181], a recent experiment found an unexpectedly large charge radius of ${}^{52}\text{Ca}$, which puts the magicity of the neutron number $N = 32$ in question [141] (also see [182]).

The flat trend of the calcium ground-state energies is reflected by the small values of the separation energies in isotopes beyond ${}^{54}\text{Ca}$. In fact, our calculations predict the S_{2n} to be negative, rendering these isotopes unbound with respect to ${}^{54}\text{Ca}$. Taking into account the uncertainties of our calculation, including the missing continuum effects, the S_{2n} may well be positive in a more refined treatment. Thus, we cannot presently identify the drip line location for the $NN+3N(400)$ Hamiltonian.

Since CCSD and CR-CC(2, 3) are single-reference methods, they can only be applied in nuclei that have good sub-shell closures. Thus, we cannot obtain S_{2n} values from these methods for comparison with our MR-IMSRG(2) results. However, in recent years, Somà *et al* have extended the SCGF approach to open-shell nuclei by using the Gor'kov formalism for systems with broken particle number symmetry [95–98]. In figure 12(b), we compare S_{2n} results from this self-consistent second-order Gor'kov Green's Function (GGF) method with those from the MR-IMSRG(2). While the GGF scheme contains less many-body correlations than the MR-IMSRG(2), the differences primarily affect absolute energies, as is evident from the agreement we see in figure 12(b). The main discrepancy between the two methods are seen near the sub-shell closures, where the S_{2n} from the GGF approach behave more smoothly. This is a consequence of the broken particle number symmetry, which causes a mixing of neighboring even-even nuclei if the sub-shell closures are sufficiently weak (note that there is no smooth transition in the GGF results at the major shell-closure $N = 20$). Thus, the S_{2n} from both methods are consistent when the same input Hamiltonian is used.

Moving on to the nickel isotopes, we show the MR-IMSRG(2) ground-state energies and two-neutron separation energies in figure 13. The binding energies of the known nickel isotopes are overestimated by about 13%. The variation of the ${}^{48-78}\text{Ni}$ ground-state energies with λ is again very weak. For CCSD and CR-CC(2, 3), it is comparable to the variation in the calcium energies, while the variation of the MR-IMSRG(2) results grows to 0.5% in ${}^{78}\text{Ni}$, and eventually to 0.7% in ${}^{86}\text{Ni}$. The nickel isotopes also exhibit a flat trend in the neutron-rich region, although it is not quite as pronounced as in the calcium isotopic chain. Consequently, the S_{2n} are quite small. Figure 13(b) shows that they become negative in ${}^{86}\text{Ni}$, but the uncertainties of our calculations are too large for a conclusive identification of the neutron drip line for the $NN+3N(400)$ Hamiltonian.

The S_{2n} also indicate the presence of sub-shell closures in ${}^{60}\text{Ni}$ and ${}^{62}\text{Ni}$ that are not seen in the experimental data. These isotopes have neutron numbers $N = 32$ and 34 , respectively, placing them in the same isotonic chains as ${}^{52,54}\text{Ca}$, where we first saw these sub-shell closures. This is another example of enhanced shell closures with $NN+3N(400)$. The mounting evidence suggests deficiencies in the tensor and spin-orbit structures of the Hamiltonian, which are the main drivers for the details of the shell evolution.

In our original study in [91], we experienced numerical problems with the MR-IMSRG(2) flow of the ${}^{64,66}\text{Ni}$ ground-state energies. Using an approximate imaginary-time generator, the ${}^{64}\text{Ni}$ energy exhibited energy oscillations in the several-percent range that did not fall off over large ranges of the flow parameter (see section 5.2), while the energy of ${}^{66}\text{Ni}$ diverges around $s \approx 1 \text{ MeV}^{-1}$. The complete Brillouin generator we use here fixes the issue in ${}^{64}\text{Ni}$, but the divergence in ${}^{66}\text{Ni}$ remains. A possible reason could be the enforcement

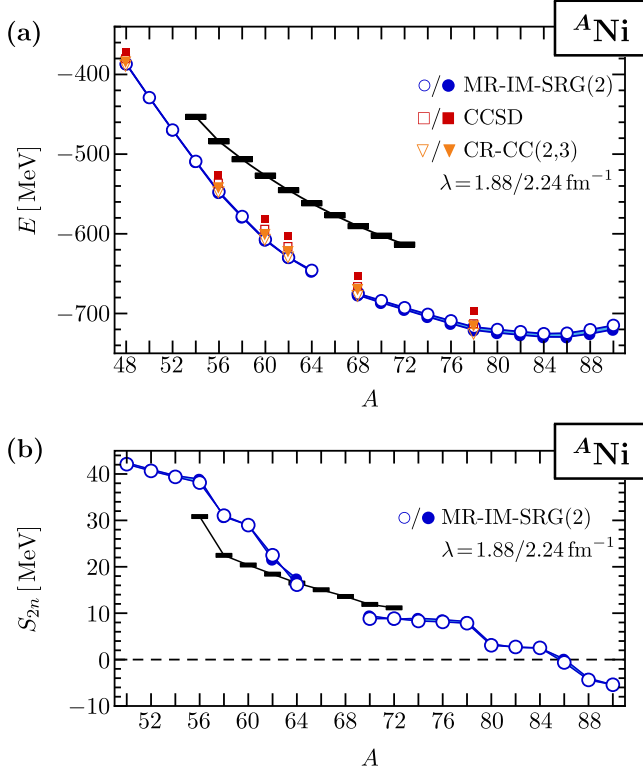


Figure 13. MR-IMSRG(2) ground-state energies (top) and two-neutron separation energies (bottom) of the nickel isotopes, for the $NN + 3N(400)$ Hamiltonian with $\lambda = 1.88, \dots, 2.24 \text{ fm}^{-1}$ ($e_{\text{max}} = 14$, $E_{3\text{max}} = 14$, optimal $\hbar\omega$). All calculations were performed with the Brillouin generator, updating the previous work [91]. For nuclei with neutron sub-shell closures, we show ground-state energies from CCSD and CR-CC(2, 3) calculations for comparison (see text and [56, 119]). Black bars indicate experimental data [108].

of spherical symmetry in our calculations. Recent experiments have revealed the coexistence of spherical ground states and axially deformed states with excitation energies below 3 MeV in ${}^{68}\text{Ni}$ and its vicinity [183–185]. In the next subsection, we will discuss examples in which the MR-IMSRG(2) successfully deals with the presence of both spherical and deformed states in the spectrum of neon isotopes, but we note that the states in question have much larger energetic separations of 7–8 MeV.

6.3. Towards doubly open-shell nuclei: neon isotopes

We want to conclude our discussion by addressing applications of the MR-IMSRG(2) away from the semi-magic chains. The biggest obstacle is the tendency of doubly open-shell nuclei to undergo transitions in their intrinsic shapes. In our calculation for semi-magic isotopic chains, we enforce spherical symmetry when we calculate HF and PNP reference states, which greatly facilitates the handling of the full $3N$ interaction at that stage. These reference states have $J^\pi = 0^+$, which implies that their density matrices are scalars under rotations and block-diagonal in angular momentum in the individual one-body, two-body, ... sectors. As a consequence, the normal-ordered Hamiltonian will be represented by block-

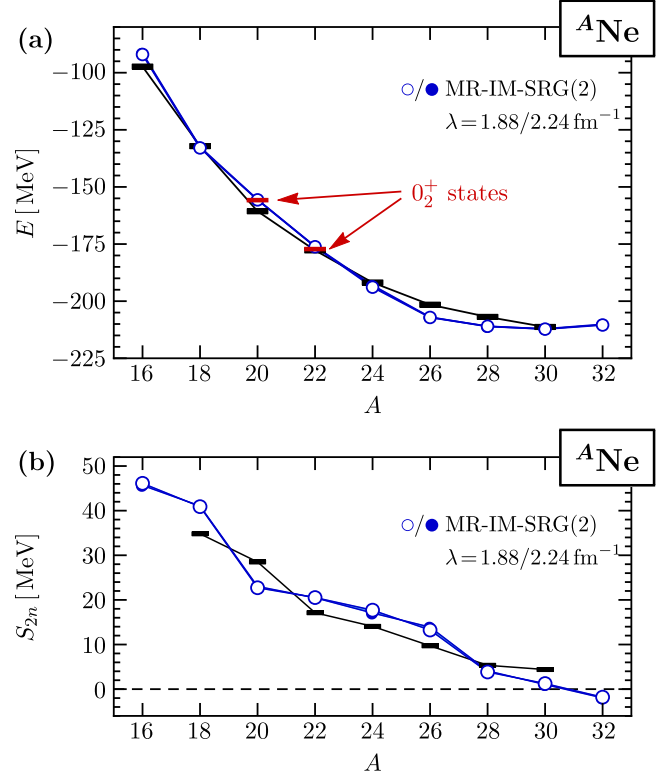


Figure 14. MR-IMSRG(2) ground-state energies (top) and two-neutron separation energies (bottom) of the neon isotopes, for the $NN + 3N(400)$ Hamiltonian with $\lambda = 1.88, \dots, 2.24 \text{ fm}^{-1}$ ($e_{\text{max}} = 14$, $E_{3\text{max}} = 14$, optimal $\hbar\omega$). Spherical symmetry is enforced for the reference states in the calculation. Red bars indicate the absolute energies of 0_2^+ excited states from shell model calculations with IMSRG-derived effective interactions that are based on the same $NN + 3N(400)$ initial Hamiltonian. Black bars indicate experimental data [108].

diagonal matrices in each sector as well, and η and $\frac{dH}{ds}$ inherit this structure through their relation with the Hamiltonian². The block-diagonal form of the MR-IMSRG flow equations holds for general $J^\pi = 0^+$ reference states, not just intrinsically spherical ones. We can just as well start from an intrinsically deformed state, e.g., from a symmetry-broken HF or HFB calculation, and project it on good angular momentum—the strategy is the same as in the PNP case. The actual computational challenge is the implementation of a converged deformed HFB calculation with $3N$ forces, which we defer for now.

Let us consider the neon isotopic chain as an example. As we can see in figure 14(a), the theoretical ground-state energies lie within a few MeV of experimental data, and they are insensitive to variations of λ . There are significant deviations

² For reference states with $J^\pi \neq 0^+$, the density matrices have non-scalar components that ultimately cause angular-momentum changing blocks in the f and Γ to be non-zero. Of course, these are coupled with the tensorial densities and creation/annihilation operators so that the H is a scalar overall. In the MR-IMSRG flow equations, we would have to couple terms consisting of three spherical tensors, namely $\eta^{(1)}$ or $\eta^{(2)}$, f or Γ , and a density matrix. Because of the complicated angular momentum algebra that results, it is most likely an easier option to solve the flow equations in an M -scheme approach instead.

between the theoretical and experimental energy trends along the isotopic chain, with the MR-IMSRG(2) energies alternating between lying above and below the experimental data. The reason for this behavior is the explicit spherical symmetry of the PNP reference states that we use in these calculations. As discussed in section 4.2, it is not guaranteed that the MR-IMSRG flow will extract the ground state, and in practice, we find that the overlap between our chosen reference state and the targeted eigenstate plays an important role. This is illustrated beautifully in the examples of ^{20}Ne and ^{22}Ne , which both have intrinsically deformed ground states [186]. In section 7, we will show that shell model calculations with IMSRG effective interactions based on the $NN+3N(400)$ Hamiltonian [164, 165] yield deformed ground states for $^{20,22}\text{Ne}$. In these calculations, we also find intrinsically spherical 0_2^+ excited states whose absolute energies are in excellent agreement with the MR-IMSRG(2) energies. We indicate these states by red bars in figure 14(a). Thus, the MR-IMSRG(2) appears to target the eigenstate whose overlap with the spherical reference state is largest.

Finally, we show the neon S_{2n} in figure 14(b). In $^{22-26}\text{Ne}$, the trend actually follows experimental data rather well, although the $NN+3N(400)$ results are offset by an almost constant shift. The drops of the theoretical S_{2n} at ^{18}Ne and ^{26}Ne are further examples of over-pronounced sub-shell closures, namely for $N = 8$ and 16 (also see [187, 188]). This supports our argument that the discrepancy between the experimental and theoretical energies for the ^{26}O resonance is not entirely due to the absence of continuum effects in our calculations.

7. Non-empirical shell model interactions from the IMSRG

In the previous section, we have reviewed MR-IMSRG results for ground state energies of semi-magic isotopic chains, i.e., singly open-shell nuclei, and presented a first look at doubly open-shell nuclei. The neon chain which served as an illustrative example is actually one of the harder cases we could have investigated, because it contains several isotopes with considerable intrinsic deformation, including clustering in the $N = Z$ nucleus ^{20}Ne . As discussed in section 6.3, the MR-IMSRG is formally capable of dealing with intrinsic deformation, but a practical implementation is very challenging and computationally demanding, and ultimately, we are still only considering ground states (or individual excited states selected by the MR-IMSRG flow).

The IMSRG framework provides us with another route for attacking the nuclear many-body problem, building on our considerations of the effective Hamiltonian in section 5.4. As we have shown in a series of publications [121, 164, 165], we can use IMSRG flows to construct non-empirical interactions for use in valence-space CI approaches like the interacting shell model. In this way, we can systematically link shell model phenomenology to the underlying nuclear interactions in the vacuum, and through them to QCD if we start from chiral NN and $3N$ interactions. The shell model gives us

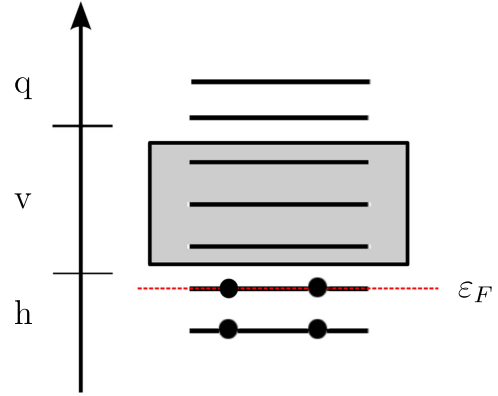


Figure 15. Separation of the single-particle basis into hole (h), valence particle (v) and non-valence particle (q) states. The Fermi energy of the fully occupied core, ε_F , is indicated by the red dashed line.

immediate access to intrinsically deformed nuclei, excited states, transitions, etc with the added benefits that we can systematically study the mechanisms by which many-body correlations are absorbed into the valence-space interactions, and maintain control over the input and many-body uncertainties. The drawback of such a combined IMSRG+shell model (IMSRG+SM) approach is that we remain bound to the factorial computational scaling of the exact diagonalization in the valence space.

In the following, we will discuss the implementation of valence-space decoupling via a straightforward modification of the ground-state decoupling, and review results from recent applications [164, 165, 189].

7.1. Valence-space decoupling

In section 4.2, we discussed in depth how we can use the (MR-)IMSRG evolution to decouple a suitable reference state from nph or general n -body excitations. From a more general point of view, we actually decouple different *sectors* of the many-body Hilbert space by driving the matrix elements of the Hamiltonian that couple these sectors to zero. To decouple multiple states in a valence space, we only need to extend our previous definition of the offdiagonal Hamiltonian from section 4.2 in a suitable manner!

Let us follow established conventions and split the single-particle basis in our calculation into core or hole (h), valence particle (v) and non-valence particle (q) orbitals (see figure 15). The actual shell model calculation for a nucleus with A nucleons is an exact diagonalization of the Hamiltonian matrix in a subspace of the Hilbert space that is spanned by configurations of the form

$$|a_{v_1}^\dagger \dots a_{v_{A_v}}^\dagger\rangle \equiv a_{v_1}^\dagger \dots a_{v_{A_v}}^\dagger |\Phi\rangle, \quad (120)$$

where $|\Phi\rangle$ is the wave function for a suitable core with A_c nucleons, and the A_v valence nucleons are distributed over the valence orbitals v_i in all allowed ways. Since the shell model assumes the core to be inert, it can be viewed as a vacuum state for the valence configurations. The matrix representation of the Hamiltonian in the space spanned by these

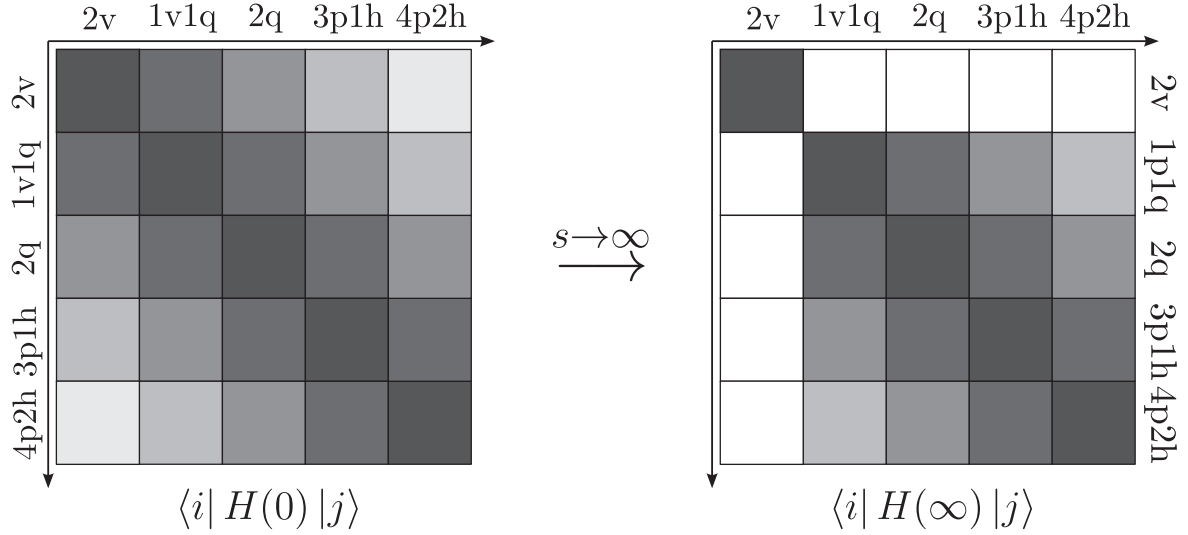


Figure 16. Schematic view of IMSRG valence-space decoupling for two valence nucleons ($p = v, q$).

Table 1. Classification of matrix elements of the many-body Hamiltonian in the many-body Hilbert space spanned by $(n + 2)$ pnh excitations of the reference state (see (16)).

No.	Type	Diagram	Energy difference Δ
I	$\langle 2p H 2p \rangle$		$f_p^p - f_{p'}^{p'}$
II	$\langle 2p H 2p \rangle$		$f_p^p + f_{p'}^{p'} - f_{p''}^{p''} - f_{p'''}^{p'''} + \Gamma_{pp'}^{pp'} - \Gamma_{p''p'''}^{p''p''}$
III	$\langle 3p1h H 2p \rangle$		$f_p^p - f_h^h - \Gamma_{ph}^{ph}$
IV	$\langle 3p1h H 2p \rangle$		$f_p^p + f_{p'}^{p'} - f_{p''}^{p''} - f_h^h + \Gamma_{pp'}^{pp'} - \Gamma_{ph}^{ph} - \Gamma_{p'h}^{p'h}$
V	$\langle 4p2h H 2p \rangle$		$f_p^p + f_{p'}^{p'} - f_h^h - f_{h'}^{h'} + \Gamma_{pp'}^{pp'} + \Gamma_{hh'}^{hh'} - \Gamma_{ph}^{ph} - \Gamma_{p'h'}^{p'h'} - \Gamma_{ph'}^{ph'} - \Gamma_{p'h}^{p'h}$

Note: For each matrix element, we show the corresponding antisymmetrized Goldstone diagrams [69] involving the one- and two-body parts of (permutations involving spectator particles which are required by antisymmetry are implied), as well as the energy differences appearing in the matrix elements for $\eta(s)$ in each case (see text).

configurations is

$$\begin{aligned} & \langle v'_1 \dots v'_{A_v} | H | v_1 \dots v_{A_v} \rangle \\ &= \langle \Phi | a_{v'_{A_v}} \dots a_{v'_1} H a_{v_1}^\dagger \dots a_{v_{A_v}}^\dagger | \Phi \rangle. \end{aligned} \quad (121)$$

For our purposes, this suggests that we normal order the

Hamiltonian and other operators with respect to the core wave function $|\Phi\rangle$, which will take on the role of the reference state for the IMSRG flow. We obtain $|\Phi\rangle$ by solving the HF equations for the core, but use the mass number A of the target nucleus (instead of A_c) in the intrinsic Hamiltonian (38). This

is appropriate, because the IMSRG+SM calculation is supposed to replicate the results of an FCI calculation for the target nucleus.

We want to use the IMSRG evolution to decouple the configurations (120) from states that involve excitations of the core, just as in the ground-state calculations. In addition, we need to decouple them from states containing nucleons in non-valence particle states. To illustrate the decoupling and identify the offdiagonal matrix elements, we consider two particles in the valence space, and show a schematic representation of the many-body Hamiltonian in a basis spanned by $(n+2)pnh$ excitations of the reference state $|\Phi\rangle$ in figure 16. In table 1, we classify the matrix elements of H which couple $2v$ to $1q1v$, $2q$, $3p1h$, and $4p2h$ excitations, respectively, where $p = v, q$. For each type of matrix element, we show antisymmetrized Goldstone diagrams (see, e.g., [69]) involving the one- and two-body vertices f and Γ (three-body vertices are omitted because of the NO2B approximation). Additional diagrams due to permutations of the nucleons or taking Hermitian adjoints are suppressed for brevity.

Diagrams (I) and (II) are eliminated if matrix elements of f and Γ that contain at least one q index are chosen to be offdiagonal. Diagrams (III) and (V) are eliminated by the reference state decoupling condition, which defines f_h^p and $\Gamma_{hh'}^{pp'}$ as offdiagonal (see section 4.2). This only leaves diagram (IV), which vanishes if matrix elements of the type $\Gamma_{vh}^{pp'}$ vanish. Thus, we define [121]

$$H_{\text{od}} \equiv \sum_{i \neq i'} f_{i'}^i : A_{i'}^i : + \frac{1}{4} \left(\sum_{pp'hh'} \Gamma_{hh'}^{pp'} : A_{hh'}^{pp'} : \right. \\ \left. + \sum_{pp'vh} \Gamma_{vh}^{pp'} : A_{vh}^{pp'} : + \sum_{pqvv'} \Gamma_{vv'}^{pq} : A_{vv'}^{pq} : \right) + \text{h.c.} \quad (122)$$

This definition of the offdiagonal Hamiltonian holds for an arbitrary number of valence particles A_v . For $A_v = 1$, diagram (II) vanishes, while diagrams (I) and (III)–(V) have the same topology, but one fewer spectator nucleon. Analogously, diagrams (I)–(V) merely contain additional spectator nucleons for $A_v > 2$.

Using H_{od} in the construction of generators, we evolve the Hamiltonian by solving the flow equations (49)–(51) in IMSRG(2) truncation. Since the core wave functions are HF Slater determinants, we can work in the single-reference limit. The final Hamiltonian is given by

$$\bar{H} = U(\infty) H U^\dagger(\infty) = E + \sum_v f_v^v : A_v^v : \\ + \frac{1}{4} \sum_{v_i, v_j, v_k, v_l} \Gamma_{v_k v_l}^{v_i v_j} : A_{v_k v_l}^{v_i v_j} : + \dots, \quad (123)$$

where the explicitly shown terms are the core energy, single-particle energies, and two-body matrix elements that are used as input for a shell model diagonalization. The solutions of

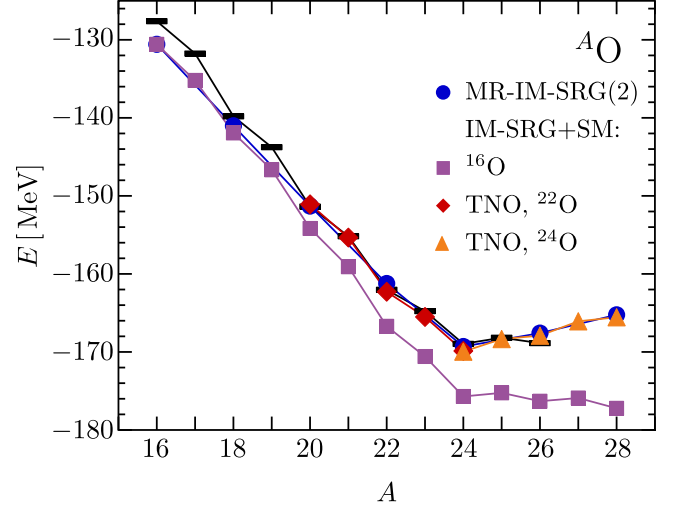


Figure 17. Ground-state energies of the oxygen isotopes, calculated from non-empirical IMSRG shell model interactions derived from $NN + 3N(400)$ at a resolution scale $\lambda = 1.88 \text{ fm}^{-1}$ and $\hbar\omega = 24 \text{ MeV}$. We compare results from the original IMSRG+SM approach discussed in [164] and an improved version using the so-called targeted normal ordering (TNO, [165]), using ^{22}O and ^{24}O as reference states. Black bars indicate experimental data [108].

that diagonalization are given by

$$|\bar{\Psi}_n\rangle = \sum_{v_1, \dots, v_{A_v}} C_{v_1 \dots v_{A_v}}^{(n)} a_{v_1}^\dagger \dots a_{v_{A_v}}^\dagger |\Phi\rangle, \quad (124)$$

and they are related to the eigenstates of the initial Hamiltonian (up to truncation errors) by

$$|\Psi_n\rangle = U^\dagger(\infty) |\bar{\Psi}_n\rangle. \quad (125)$$

The naive computational scaling for the valence-decoupling procedure described here is $\mathcal{O}(N^6)$, just like that of MR-IMSRG(2) or IMSRG(2) ground-state calculations. In practice, individual calculations require about 100–1000 core hours, putting the effort between that of single-reference and multireference ground-state calculations. Compared to other non-perturbative approaches for the construction of non-empirical shell model interactions, this effort is low [190–192]. Moreover, we note that we obtain consistent neutron–neutron, proton–neutron, and proton–proton interactions from the same IMSRG evolution.

7.2. Ground-state energies and targeted normal ordering

As a first application [164], we tested the IMSRG+SM approach in the oxygen isotopic chain, where results from large-scale MR-IMSRG ground state calculations and a variety of other exact and approximate *ab initio* methods are available for comparison (see section 6).

In figure 17 we show the oxygen ground-state energies, calculated with effective interactions derived from the $NN + 3N(400)$ Hamiltonian (see section 5.1) at a resolution scale $\lambda = 1.88 \text{ fm}^{-1}$. Note that we include ground-state energies for the odd oxygen isotopes, which are easily obtainable from a shell model calculation. In the vicinity of ^{16}O , the ground-state energies obtained from IMSRG+SM

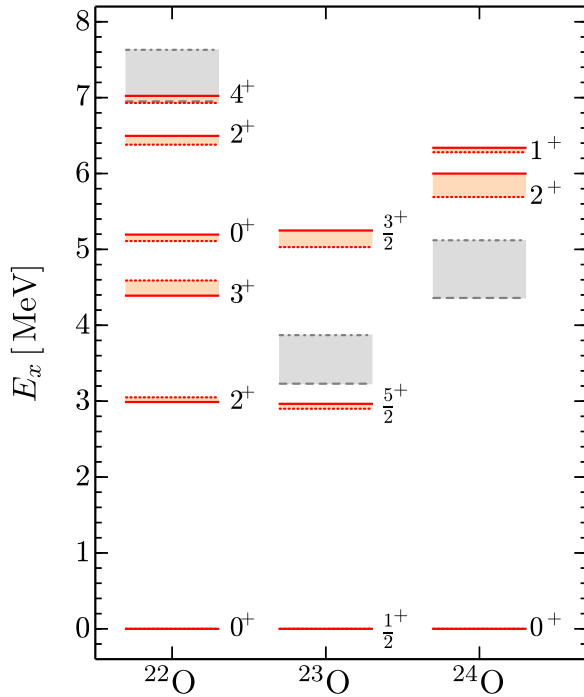


Figure 18. Excitation spectra of $^{22-24}\text{O}$ from IMSRG+SM calculations with (solid lines) and without targeted normal ordering (dotted lines, see text). All effective interactions are derived from the chiral $NN + 3N(400)$ interaction at resolution scale $\lambda = 1.88 \text{ fm}^{-1}$ ($e_{\text{max}} = 14$, $E_{3\text{max}} = 14$, $\hbar\omega = 24 \text{ MeV}$). The gray dashed and dash-dotted lines indicate the neutron separation energies.

and MR-IMSRG(2) calculations agree well with each other and experimental data, but for growing neutron number N , the IMSRG+SM solutions are increasingly overbound.

The origin of this discrepancy can be traced back to the reference state we use for both the normal ordering and the IMSRG valence-space decoupling. Initially, we used HF solutions for the ^{16}O core, only changing the mass number of the intrinsic Hamiltonian to that of the target nucleus, as explained in the previous subsection. When we normal order the Hamiltonian and perform the IMSRG evolution, we miss contributions from the valence nucleons that are taken into account fully in the MR-IMSRG ground-state calculations. In [165], we took a first step towards remedying this deficiency by means of a so-called *targeted normal-ordering* (TNO) procedure, in which the reference state for the normal ordering and decoupling is a HF solution for a closed sub-shell nucleus in close proximity to the target nucleus. Then, the Hamiltonian is re-normal ordered with respect to the ^{16}O core that is assumed by the shell model calculation. As shown in figure 17, this procedure essentially eliminates the difference between the IMSRG+SM and MR-IMSRG(2) ground-state energies, reducing the overbinding of the neutron-rich oxygen isotopes by several MeV. For ^{24}O , we can use both ^{22}O and ^{24}O as reference states for the TNO and decoupling. The resulting ground-state energies are -169.874 MeV and -169.956 MeV , respectively, in excellent agreement with each other and the MR-IMSRG(2) result for the same initial Hamiltonian, which is -169.491 MeV .

In figure 18, we show the effect of the TNO on the low-lying excitation spectra of $^{22-24}\text{O}$ and the neutron separation energies

$$S_n(Z, N) = E(Z, N - 1) - E(Z, N). \quad (126)$$

Calculations were performed with an ^{22}O reference state. If we use an ^{24}O reference state instead, both the excitation energies and neutron separation energies change by 80 keV or less (not shown). Figure 18 illustrates that the TNO improves the core energy, single-particle energies, and two-body matrix elements, in decreasing order of importance. For the nuclei shown here, the core energy is raised by 3.5–4 MeV, which accounts for the bulk of the ground-state energy improvement. The input single-particle energies for protons and neutrons are increased by up to 1.3 MeV ($\pi 0d_{3/2}$) and 200 keV ($\nu 1s_{1/2}$), respectively. The S_n decrease rather uniformly by 600 keV for our sample nuclei. Finally, the effect of the TNO on the two-body matrix elements is weak, so the orderings and level spacings of the excitation spectra are hardly affected. The largest change in excitation energy is about 250 keV.

7.3. Spectroscopy of *sd*-shell nuclei

Let us now discuss IMSRG+SM results for the spectra of selected *sd*-shell nuclei, starting with $^{22-24}\text{O}$. In figure 19, we show results obtained with the $NN + 3N(400)$ interaction at a resolution scale $\lambda = 1.88 \text{ fm}^{-1}$. The shaded band results from varying the oscillator basis parameter from $\hbar\omega = 20 \text{ MeV}$ to 24 MeV , which serves as an indicator for the convergence of a specific excited state. Factors that can affect the convergence are complex intrinsic shapes, the extension of the wave function's tail, etc. Overall, the convergence is satisfactory for the nuclei shown here. The IMSRG+SM results agree impressively well with experimental data, given that the parameters of our Hamiltonian have not been adjusted to the oxygen isotopes at all (see [164] for a more detailed analysis). The inclusion of $3N$ interactions in the initial Hamiltonian is crucial for achieving this good reproduction of the experimental level data: it stabilizes the spacing between the neutron $0d_{3/2}$ orbital and the other levels in the *sd*-shell as neutrons are added, which governs the energies of low-lying excitations and the location of the neutron drip line [54, 127, 160, 163]. We note that the excited states in $^{23,24}\text{O}$ are overestimated to some degree, but this is expected because our shell model calculations do not explicitly treat the continuum coupling at present, and the $NN + 3N(400)$ Hamiltonian produces a too-pronounced shell closure at $N = 16$ (see section 6.1).

In figure 19, we also compare our spectra to results obtained with the phenomenological USDB interaction [8], as well as non-empirical valence-space Hamiltonians obtained within the coupled cluster effective interaction (CCEI) approach [190, 194]. We note that the former depends on the mass number A of the target nucleus through a scaling of the two-body matrix elements [8]. In the latter, interactions for specific target masses were constructed for use in the oxygen isotopes, starting from the same Hamiltonian that we used for

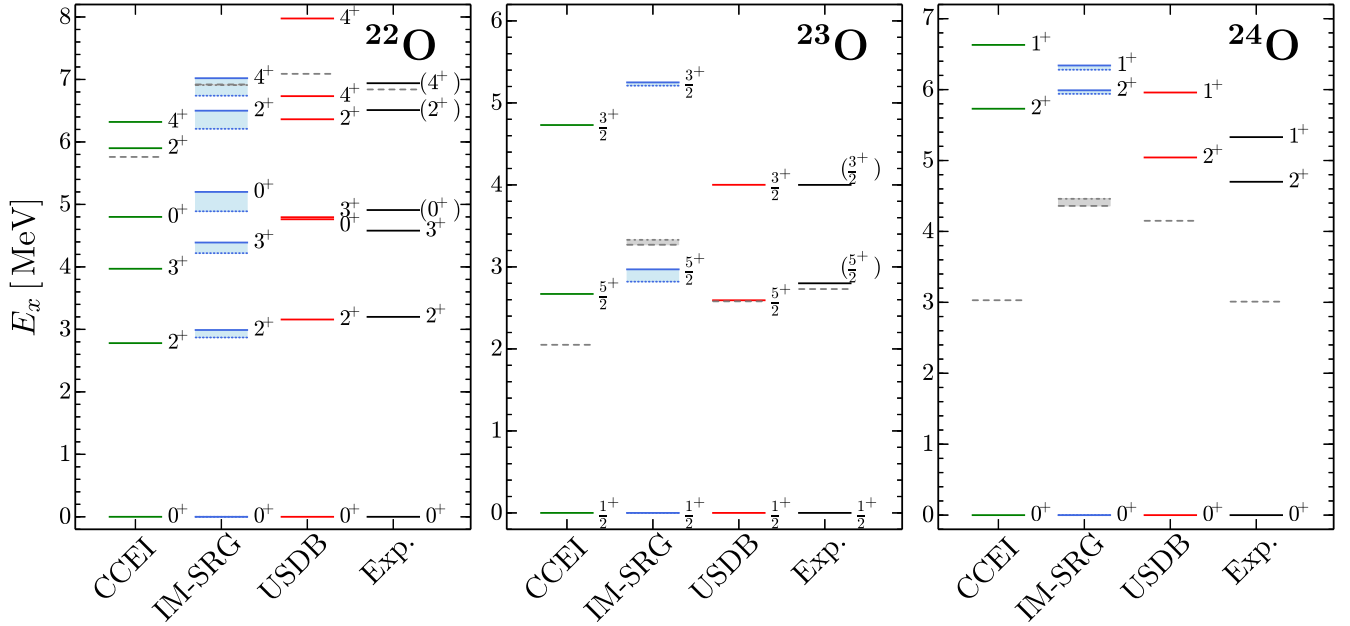


Figure 19. Excitation spectra of $^{22-24}\text{O}$ based on the chiral $NN + 3N(400)$ interaction at resolution scale $\lambda = 1.88 \text{ fm}^{-1}$. We compare results for effective interactions derived by IMSRG valence-space decoupling ($e_{\text{max}} = 14$, $E_{3\text{max}} = 14$, $\hbar\omega = 20 \text{ MeV}$ (dashed lines) and 24 MeV (solid lines)), the A -dependent CCEI approach of [190] ($e_{\text{max}} = 12$, $E_{3\text{max}} = 14$, $\hbar\omega = 20 \text{ MeV}$), and the phenomenological USDB interaction [8] to experimental data [193]. The dashed lines represent the neutron separation energies.

the IMSRG+SM here. The CCEI and IMSRG results for $\hbar\omega = 20 \text{ MeV}$ are in very good agreement. Since CCEI is built from CCSD and its equation-of-motion extension to excited states [92, 190, 195], the reshuffling of correlations into the valence-space effective interaction should be similar to that of IMSRG(2) valence decoupling, and therefore reflect the similarity of CCSD and IMSRG(2) ground-state results (see sections 5.4 and 6). The biggest discrepancy occurs for the neutron separation energies, which are lower for CCEI because neutron-rich oxygen isotopes are increasingly underbound (see [190]).

The USDB interaction is optimized to simultaneously describe more than 600 excited states in sd -shell nuclei [8], hence it is not surprising that the USDB spectra agree very well with experiment. We observe the most notable deviation for the second 0^+ and the 3^+ state in ^{22}O , which are nearly degenerate and whose ordering is inverted compared to experiment. The CCEI and IMSRG interactions describe the level ordering correctly. The latter even seems to give the correct level spacing for $\hbar\omega = 24 \text{ MeV}$, although it is necessary to reduce the $\hbar\omega$ variation of the 3^+ state to make a conclusive claim here.

As mentioned in section 7.1, the IMSRG valence-space decoupling provides us with a consistent set of proton–proton, proton–neutron, and neutron–neutron interaction matrix elements at the same time, so we can easily extend our calculations into the sd -shell. For instance, we calculated the excitation spectrum of ^{24}F in support of a recent experiment at GANIL [189]. In figure 20, we again compare IMSRG+SM (with $\hbar\omega$ variation) to experimental data and other theoretical

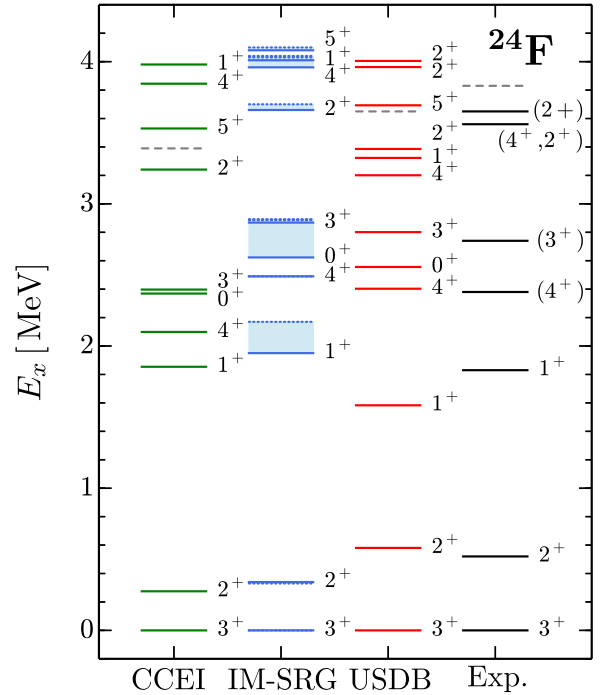


Figure 20. Excitation spectrum of ^{24}F based on the chiral $NN + 3N(400)$ interaction at $\lambda = 1.88 \text{ fm}^{-1}$. We compare results for effective interactions derived by IMSRG valence-space decoupling ($e_{\text{max}} = 14$, $E_{3\text{max}} = 14$, $\hbar\omega = 20 \text{ MeV}$ (dashed lines) and 24 MeV (solid lines)), the A -independent CCEI interaction [194] ($e_{\text{max}} = 12$, $E_{3\text{max}} = 14$, $\hbar\omega = 20 \text{ MeV}$), and the phenomenological USDB interaction [8] to experimental data [189, 193]. The dashed lines represent the neutron separation energies.

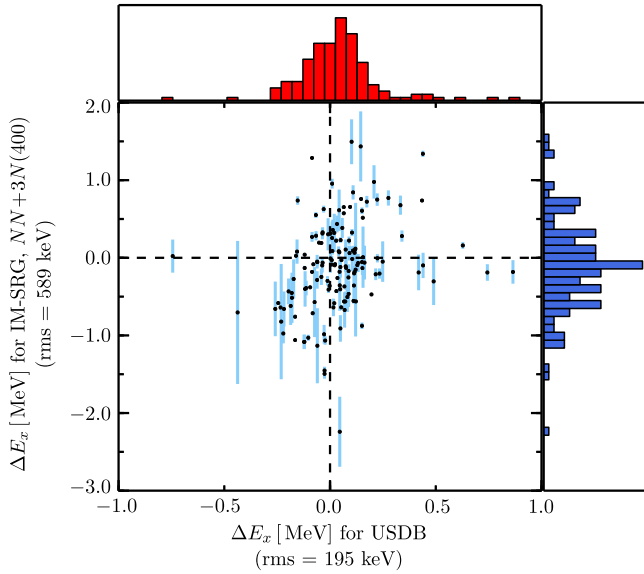


Figure 21. Deviation of theoretical excitation energies from experimental data for 144 levels in O, Fe, Ne, Na, Mg, calculated with USDB and IMSRG effective interactions derived from $NN + 3N(400)$ at $\lambda = 1.88 \text{ fm}^{-1}$. The error bars indicate the uncertainty of IMSRG excitation energies from varying $\hbar\omega$ of the underlying oscillator basis (see text).

results. States below 3 MeV are described well by the IMSRG, and aside from the 0^+ and 1^+ states, very well converged. The IMSRG interaction exhibits a gap in the spectrum between the 3_2^+ and 2_2^+ states, which USDB fills with a group of states that has not been observed at the corresponding energy in the experiment.

The CCEI results we show in figure 20 were obtained with the A -independent interaction that was recently published in [194]. While the ordering of the low-lying states is the same as for the IMSRG interactions, the positions and spacings of the levels are notably different. We assume that this is caused by fixing A to the mass number of the ^{16}O core (and its vicinity) instead of the target nucleus when the interaction is constructed [190, 194]. This issue will be investigated further elsewhere.

Encouraged by the good agreement of our excitation energies with results for the USDB interaction, we decided to broaden our perspective beyond individual nuclei. In figure 21, we compare the deviations of theoretical and experimental excitation energies of 144 excited states in the O, Fe, Ne, Na and Mg isotopes, for both USDB and the A -dependent IMSRG valence-space interactions discussed here. For USDB, the root mean square (rms) deviation is a mere 195 keV, with individual deviations ranging from -1 to 1 MeV. Aside from a few outliers, the bulk of the deviations for the IMSRG interactions fall in a similar range, but the distribution is wider, leading to an rms deviation of 589 keV. The ‘error bars’ on the IMSRG results indicate the uncertainty of the excitation energies due to a variation of $\hbar\omega$ from 20 to 24 MeV—we remind the reader that the effect of such variations depends on the structure and convergence of individual states, as mentioned above. In summary, while the

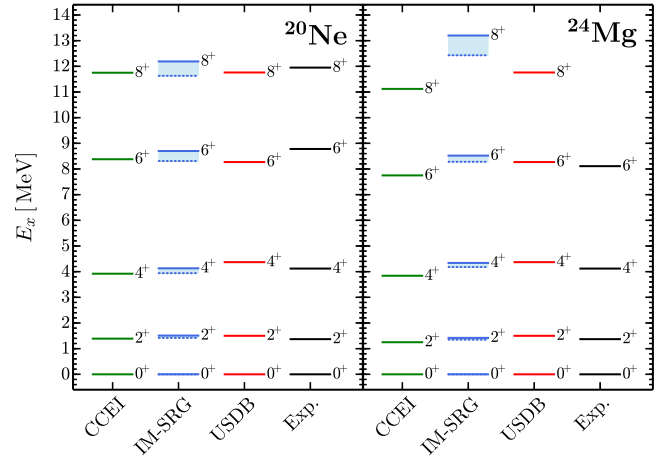


Figure 22. Ground-state rotational bands of ^{20}Ne and ^{24}Mg , based on the $NN + 3N(400)$ interaction at $\lambda = 1.88 \text{ fm}^{-1}$. We compare results for effective interactions derived by IMSRG valence-space decoupling ($e_{\text{max}} = 14$, $E_{3\text{max}} = 14$, $\hbar\omega = 20$ MeV (dashed lines) and 24 MeV (solid lines)), the A -independent CCEI interaction [194] ($e_{\text{max}} = 12$, $E_{3\text{max}} = 14$, $\hbar\omega = 20$ MeV), and the phenomenological USDB interaction [8] to experimental data [189, 193]. The dashed lines represent the neutron separation energies.

description of the states in the lower sd -shell with IMSRG derived interactions is not on the same level of accuracy as with USDB, it is very encouraging that an rms of 589 keV can be achieved without adjusting the parameters of the Hamiltonian to the nuclei in the region.

7.4. Deformation and rotational bands

As discussed above, the shell model gives us access to nuclei with intrinsic deformation. The ground-state rotational bands of ^{20}Ne and ^{24}Mg are shown in figure 22. The levels obtained with the IMSRG and the A -independent CCEI interactions, both based on the $NN + 3N(400)$ Hamiltonian ($\lambda = 1.88 \text{ fm}^{-1}$), are in good agreement with each other as well as the USDB interaction. While rotational bands emerge naturally in these nuclei even without an initial chiral $3N$ force, its inclusion markedly improves the agreement of the theoretical excitation energies and level spacings with experimental data [165].

The shell model’s capability to describe intrinsically deformed nuclei allows us to follow up on our discussion of ^{20}Ne from section 6.3 now. There, we claimed that the MR-IMSRG(2) extracts an excited state with spherical intrinsic structure. In the left panel of figure 23, we show the absolute energies of the four lowest 0^+ states in ^{20}Ne , and the MR-IMSRG(2) energy for the same Hamiltonian. The MR-IMSRG(2) energy is in excellent agreement with that of the 0_2^+ state. The middle column of the panel shows the overlap of the shell model eigenstate with the spherical configuration (suppressing the core wave function) $|\pi 0 d_{5/2}^2 J_\pi = 0, [\nu 0 d_{5/2}^2] J_\nu = 0; J = 0\rangle$, which is a fair approximation to the spherical PNP reference state we use for the MR-IMSRG(2). This overlap is indeed largest for the 0_2^+ state, but also considerable for the 0_1^+ state.

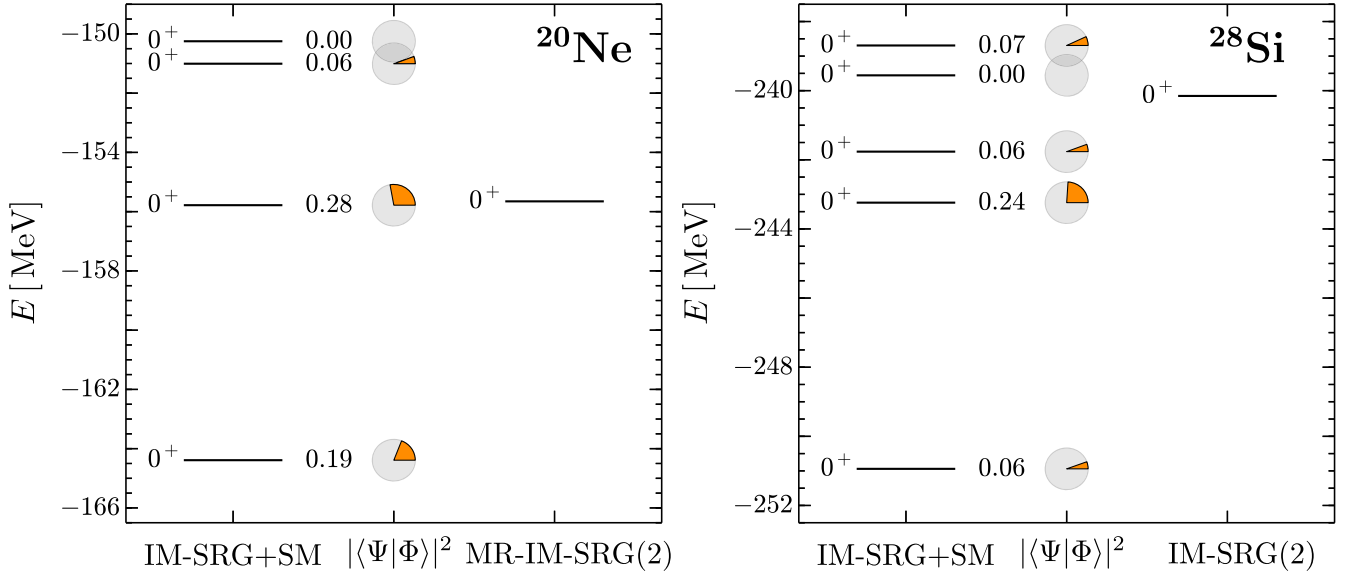


Figure 23. Absolute energies of the 0^+ states in ^{20}Ne and ^{28}Si from shell model calculation with an IMSRG derived interaction, compared to the result of MR-IMSRG(2) ground-state calculations. The $NN + 3N(400)$ Hamiltonian at $\lambda = 1.88 \text{ fm}^{-1}$ served as input in all cases. The middle column shows the overlap of the shell model solutions with intrinsically spherical shell model configurations:

$|\langle \pi 0 d_{5/2} \rangle^2 J_\pi = 0, [\nu 0 d_{5/2}]^2 J_\nu = 0; J = 0\rangle$ for ^{20}Ne , and $|\langle \pi 0 d_{5/2} \rangle^6 J_\pi = 0, [\nu 0 d_{5/2}]^6 J_\nu = 0; J = 0\rangle$ for ^{28}Si .

As another example, we consider ^{28}Si . For the Hamiltonian we use here, there is a stable HF solution with closed proton and neutron subshells and spherical intrinsic structure. The MR-IMSRG(2) energy (or rather, IMSRG(2) energy because of the HF reference state) is within 400 keV of the 0_4^+ state, but that specific shell model solution has practically no overlap with the $|\langle \pi 0 d_{5/2} \rangle^6 J_\pi = 0, [\nu 0 d_{5/2}]^6 J_\nu = 0; J = 0\rangle$ configuration that is identical to the reference state used for both the IMSRG(2) calculation and the (TNO) valence decoupling. The overlap is largest for the 0_2^+ state (24%), whose absolute energy is -243.2 MeV , compared to the IMSRG(2) energy of -240.2 MeV .

An absolute energy difference of 3 MeV between the IMSRG+SM and IMSRG(2) results is well within the realm of possibility, given the estimated uncertainties due to the many-body truncation. This is especially relevant because ^{28}Si is an $N = Z$ nucleus, and therefore exhibits α -cluster correlations in excited states [196]. The IMSRG(2) energy contains only limited contributions from $4p4h$ excitations, which appear first as immediate excitations in fourth-order MBPT diagrams (see [61]). A complete treatment of $4p4h$ excitations would make it necessary to work in IMSRG(4) truncation (or use a reference state with α correlations in the MR-IMSRG). In contrast, the shell model diagonalization can readily access $4p4h$ excitations in the valence space. From this perspective, it is perhaps more surprising that the IMSRG+SM and MR-IMSRG(2) energies for the 0_2^+ state in the ^{20}Ne are practically identical, because that nucleus should exhibit α correlations as well. We conclude our discussion here, and defer further investigations of this issue to a future publication.

8. Conclusions and outlook

Over the course of this article, we have strived to give a pedagogical introduction to the description of nuclear many-body physics in the IMSRG framework. The IMSRG belongs to a family of efficient, systematically extendable many-body approaches that have extended the reach of *ab initio* nuclear structure theory well into the medium-mass region of the nuclear chart in recent years (see, e.g., [56, 61]). The MR-IMSRG and IMSRG+SM, specifically, are ideally suited to investigate the properties of open-shell nuclei with a systematic assessment of the theoretical uncertainties. The consistency of the results from these two different approaches that are rooted in the same framework is highly encouraging, promising many opportunities for cross-validating and interpreting nuclear structure results in future applications (see sections 6 and 7). The capability to confront nuclear interactions from chiral EFT with a wealth of new many-body data will be of great importance in the ongoing effort of understanding and improving these interactions, which are currently the dominant source of uncertainty in all *ab initio* many-body calculations (see section 6).

Of course, there is much work to be done. A variety of efforts are underway to further extend the capabilities of the MR-IMSRG and IMSRG+SM approaches. The MR-IMSRG allows us to explore both dynamic and static correlations. The former are due to the dynamics of correlated nucleon pairs, triples, etc in the nucleus, which is captured well by the (generalized) particle-hole expansion that underlies the MR-IMSRG flow equations. In contrast, static correlations are collective and would require us to treat up to $ApAh$ correlations, in exact and numerically unfeasible IMSRG(A) or MR-

IMSRG(A) truncation schemes. However, collective correlations can be treated efficiently by breaking and restoring symmetries of the nuclear wave function, and using the generator coordinate method to mix various projected configurations (see, e.g., [197]). We can calculate the density matrices of such many-body wave functions, and use them as reference states for the MR-IMSRG(2), combining dynamic and static correlation. The use of PNP reference states in our applications of the MR-IMSRG(2) to open-shell nuclei (see section 6) is the simplest possible example of such a combined approach, and the use of GCM reference states with richer collective structures is being explored now.

Another important new development is the successful use of Magnus expansion techniques to explicitly construct the unitary transformation that is generated by the IMSRG [122]. This greatly simplifies the evaluation of general observables, which can be obtained with a simple application of $U(s)$ to the operator of interest rather than a concurrent evolution alongside the Hamiltonian by means of additional sets of flow equations. Moreover, the Magnus methods make it possible to construct systematic approximations to the complete IMSRG (3) flow, analogous in many-body content and computational efficiency to non-iterative triples methods in CC [119, 153, 154, 168]. The extension of this approach to the MR-IMSRG is in progress.

The triples corrections to IMSRG Hamiltonians will also be extremely valuable for the IMSRG+SM approach, allowing us to test the many-body convergence of the valence-space interaction and operators. The construction of valence-space transition operators is now in full swing, with the prospect of shedding new light on the emergence of the phenomenological effective charges. A new refinement of the targeted normal ordering procedure was presented in [198], improving once again the agreement between IMSRG+SM and large-scale MR-IMSRG calculations.

As an alternative to the exact valence-space diagonalization in the IMSRG+SM approach, we are working on combining the IMSRG with equation-of-motion methods (see [69]). The basic framework has been developed and tested for the single-reference case [199], and we aim to generalize it to multireference applications as a next step, incorporating triples corrections to the (MR-)IMSRG evolved Hamiltonian at the same time.

Last but not least, the IMSRG+SM and IMSRG based EoM approaches are, in essence, established techniques for many-body calculations whose results are (possibly) enhanced through the use of an IMSRG improved effective Hamiltonian. We have begun to explore the use of such IMSRG and MR-IMSRG improved Hamiltonians as input for other methods. A promising combination of MR-IMSRG and NCSM as discussed in [152].

The RG perspective is a key element that is woven into all of the applications discussed in this review, and the future directions mentioned in our look ahead. In my (admittedly biased) view, this is a unique feature of the IMSRG framework that sets it apart from the other many-body methods that we

touched upon during this work. When the comparison with those other methods and experimental data is our first and foremost concern, we are primarily interested in the $s \rightarrow \infty$ limit of the IMSRG or MR-IMSRG evolution, but the flow trajectory offers a wealth of additional insight. By considering points along the trajectory, we can gain a new understanding of how many-body correlations are reshuffled between the wave function and the Hamiltonian, or different pieces of the Hamiltonian, making transparent what is only implicitly assumed in other methods. Like in the free-space SRG (or other RG methods), we have the freedom to work at intermediate values of s if this is more practical than working at $s = 0$ (in appropriate units) or in the limit $s \rightarrow \infty$, especially if we would incur unacceptable numerical errors at either of these extremes (see, e.g., [82, 83, 152]). This is the inherent power of a framework that integrates many-body and RG techniques, and the reason why the IMSRG is an extremely versatile and valuable tool for quantum many-body theory.

Acknowledgments

Special acknowledgments are due to all my collaborators on the IMSRG framework presented in this work: In chronological order, they are S K Bogner, K Tsukiyama, A Schwenk, T D Morris, N M Paruchowski, J D Holt, and S R Stroberg. Furthermore, I am grateful to C Barbieri, S Binder, A Calci, T Duguet, F Evangelista, R J Furnstahl, E Gebrer-ufael, G Hagen, K Hebeler, M Hjorth-Jensen, G R Jansen, R Roth, J Simonis, V Somà and K A Wendt for many useful discussions on the subjects discussed in this work. I am also grateful to A Calci, S Binder, and R Roth for providing matrix elements of the chiral $3N$ interactions, and to S R Stroberg for sharing his scripts for the visualization of shell model results.

I would like to thank the National Superconducting Cyclotron Laboratory (NSCL)/Facility for Rare Isotope Beams (FRIB) and Michigan State University for startup support during the preparation of this work. Computing resources were provided by the Ohio Supercomputing Center (OSC), the Michigan State University High Performance Computing Center (HPCC)/Institute for Cyber-Enabled Research (iCER), and the National Energy Research Scientific Computing Center (NERSC), a DOE Office of Science User Facility supported by the Office of Science of the US Department of Energy under Contract No. DE-AC02-05CH11231.

Appendix A. Products and commutators of normal-ordered operators

We introduce the permutation symbol P_{ij} to interchange the attached indices in any expression, i.e.,

$$P_{ij}g(\dots, i, \dots, j) \equiv g(\dots, j, \dots, i). \quad (\text{A.1})$$

A.1. Operator products

$$:A_b^a::A_l^k:= :A_{bl}^{ak}:-\lambda_l^a:A_b^k:-\xi_b^k:A_l^a:-\lambda_l^a\xi_b^k+\lambda_{bl}^{ak}, \quad (A.2)$$

$$\begin{aligned} :A_b^a::A_{mn}^{kl}:=& :A_{bmn}^{akl}:+(1-P_{mn})\lambda_n^a:A_{bm}^{kl}: \\ & +(1-P_{kl})\xi_b^l:A_{mn}^{ak}: \\ & +(1-P_{kl})(1-P_{mn})\lambda_{bn}^l:A_m^k: \\ & +(1-P_{kl})\lambda_{mn}^{ak}:A_b^l:+(1-P_{mn})\lambda_{bm}^{kl}:A_n^a: \\ & +(1-P_{kl})(1-P_{mn})\lambda_m^a\xi_b^l:A_n^k: \\ & +(1-P_{mn})\lambda_n^a\lambda_{bm}^{kl}+(1-P_{kl})\lambda_{mn}^{ak}\xi_b^l+\lambda_{bmn}^{akl}, \end{aligned} \quad (A.3)$$

$$\begin{aligned} & :A_{cd}^{ab}::A_{mn}^{kl}: \\ =& :A_{cdmn}^{abkl}:+(1-P_{ab})(1-P_{mn})\lambda_m^a:A_{cdn}^{bkl}: \\ & +(1-P_{cd})(1-P_{kl})\xi_c^k:A_{dmn}^{abl}: \\ & +(\lambda_{mn}^{ab}+(1-P_{mn})\lambda_m^a\lambda_n^b):A_{cd}^{kl}: \\ & +(\lambda_{cd}^{kl}+(1-P_{cd})\xi_c^k\xi_d^l):A_{mn}^{ab}: \\ & +(1-P_{ab})(1-P_{cd})(1-P_{kl})(1-P_{mn}) \\ & \times (\lambda_{cm}^{ak}-\lambda_m^a\xi_c^k):A_{dn}^{bl}: \\ & +(1-P_{ab})(1-P_{kl})\lambda_{mn}^{al}:A_{cd}^{bk}: \\ & +(1-P_{ab})(1-P_{kl})\lambda_{cd}^{bk}:A_{mn}^{al}: \\ & +(1-P_{cd})(1-P_{mn})\lambda_{cn}^{kl}:A_{dm}^{ab}: \\ & +(1-P_{cd})(1-P_{mn})\lambda_{dm}^{ab}:A_{cn}^{kl}: \\ & +(1-P_{ab})(1-P_{mn})(\lambda_{cdn}^{bkl} \\ & - (1-P_{cd})(1-P_{kl})\xi_c^k\lambda_{dn}^{bl} \\ & + \lambda_n^b(\lambda_{cd}^{kl}+\xi_c^k\xi_d^l-\xi_d^k\xi_c^l)):A_m^a: \\ & +(1-P_{cd})(1-P_{kl})(\lambda_{dmn}^{abl} \\ & - (1-P_{ab})(1-P_{mn})\lambda_m^a\lambda_{dn}^{bl} \\ & + \xi_d^l(\lambda_{mn}^{ab}+\lambda_m^a\lambda_n^b-\lambda_n^a\lambda_m^b)):A_c^k: \\ & +(1-P_{ab})(1-P_{cd})(\lambda_{dmn}^{bkl} \\ & + (1-P_{mn})\lambda_n^b\lambda_{dm}^{kl}+(1-P_{kl})\xi_d^l\lambda_{mn}^{bl}):A_c^a: \\ & +(1-P_{kl})(1-P_{mn})(\lambda_{cdn}^{abl} \\ & + (1-P_{ab})\lambda_n^a\lambda_{cd}^{bl}+(1-P_{cd})\xi_c^l\lambda_{dn}^{ab}):A_m^k: \\ & +\lambda_{cdmn}^{abkl}+(1-P_{ab})(1-P_{mn})\lambda_m^a\lambda_{cdn}^{bkl} \\ & +(1-P_{cd})(1-P_{kl})\xi_c^k\lambda_{dmn}^{abl} \\ & - (1-P_{cd})(1-P_{mn})\lambda_{cm}^{ab}\lambda_{dn}^{kl} \\ & +(1-P_{cd})(1-P_{kl})(1-P_{mn})\lambda_{cm}^{ak}\lambda_{dn}^{bl} \\ & +(1-P_{kl})(\lambda_{mn}^{al}\lambda_{cd}^{bk}-\lambda_{cd}^{ak}\lambda_{mn}^{bl}) \\ & +(1-P_{ab})(1-P_{cd})(1-P_{kl})(1-P_{mn})\lambda_m^b\xi_c^k\lambda_{dn}^{al} \\ & +(\lambda_{mn}^{ab}+\lambda_m^a\lambda_n^b-\lambda_n^a\lambda_m^b)(\lambda_{cd}^{kl}+\xi_c^k\xi_d^l-\xi_d^k\xi_c^l). \end{aligned} \quad (A.4)$$

A.2. Commutators

$$[:A_b^a::, :A_l^k:] = \delta_b^k:A_l^a:-\delta_l^a:A_b^k:+\lambda_l^a\delta_b^k-\lambda_b^k\delta_l^a, \quad (A.5)$$

$$\begin{aligned} [:A_b^a::, :A_{mn}^{kl}]&= (1-P_{kl})\delta_b^k:A_m^{al}: \\ & -(1-P_{mn})\delta_m^a:A_{bn}^{kl}: \\ & +(1-P_{kl})(1-P_{mn})(\delta_b^l\lambda_n^a-\delta_n^a\lambda_b^l):A_m^k: \\ & +(1-P_{kl})\delta_b^k\lambda_{mn}^{al} \\ & -(1-P_{mn})\delta_m^a\lambda_{bn}^{kl}, \end{aligned} \quad (A.6)$$

$$\begin{aligned} [:A_{cd}^{ab}::, :A_{mn}^{kl}]&= (1-P_{ab})(1-P_{mn})\delta_m^a:A_{cdn}^{bkl}: \\ & -(1-P_{cd})(1-P_{kl})\delta_c^k:A_{dmn}^{abl}: \\ & +(1-P_{cd})(\xi_c^k\xi_d^l-\lambda_c^k\lambda_d^l):A_{mn}^{ab}: \\ & +(1-P_{ab})(\lambda_m^a\lambda_n^b-\xi_m^a\xi_n^b):A_{cd}^{kl}: \\ & +(1-P_{ab})(1-P_{cd})(1-P_{kl})(1-P_{mn}) \\ & \times (\delta_d^l\lambda_n^b-\delta_n^b\lambda_d^l):A_{cm}^{ak}: \\ & +(1-P_{ab})(1-P_{mn})(\delta_n^b\lambda_{cd}^{kl} \\ & + (1-P_{cd})(1-P_{kl})\delta_c^k\lambda_{dn}^{bl} \\ & + \lambda_n^b\xi_c^k\xi_d^l-\xi_n^b\lambda_c^k\lambda_d^l):A_m^a: \\ & -(1-P_{cd})(1-P_{kl})(\delta_d^l\lambda_{mn}^{ab} \\ & + (1-P_{ab})(1-P_{mn})\delta_m^a\lambda_{dn}^{bl} \\ & + \lambda_d^l\xi_m^a\xi_n^b-\xi_d^l\lambda_m^a\lambda_n^b):A_c^k: \\ & -(1-P_{ab})(1-P_{cd})(1-P_{mn})\delta_m^b\lambda_{dn}^{kl} \\ & - (1-P_{kl})\delta_d^k\lambda_{mn}^{bl}):A_c^a: \\ & +(1-P_{kl})(1-P_{mn})(1-P_{ab})\delta_n^a\lambda_{cd}^{bl} \\ & - (1-P_{cd})\delta_c^l\lambda_{dn}^{ab}):A_m^k: \\ & +(1-P_{ab})(1-P_{mn})\delta_m^a\lambda_{cdn}^{bkl} \\ & - (1-P_{cd})(1-P_{kl})\delta_c^k\lambda_{dmn}^{abl} \\ & +(1-P_{cd})\lambda_{mn}^{ab}(\xi_c^k\xi_d^l-\lambda_c^k\lambda_d^l) \\ & +(1-P_{ab})\lambda_{cd}^{kl}(\lambda_m^a\lambda_n^b-\xi_m^a\xi_n^b) \\ & +(1-P_{ab})(1-P_{cd})(1-P_{kl})(1-P_{mn}) \\ & \times (\delta_d^l\lambda_n^b-\delta_n^b\lambda_d^l)\lambda_{cm}^{ak} \\ & +(1-P_{ab})(1-P_{cd}) \\ & \times (\lambda_m^a\lambda_n^b\xi_c^k\xi_d^l-\lambda_c^k\lambda_d^l\xi_m^a\xi_n^b). \end{aligned} \quad (A.7)$$

Appendix B. Particle-number projected HFB reference states

In this appendix, we summarize the essential properties of particle-number projected HFB states. More details can be found, e.g., in [197, 200]. We introduce fermionic quasi-particle operators $\alpha_k, \alpha_k^\dagger$ that are superpositions of creation and annihilation operators by means of a Bogoliubov–Valatin transformation:

$$\alpha_k^\dagger = u_k a_k^\dagger - v_k a_{\bar{k}}, \quad (B.1)$$

$$\alpha_{\bar{k}}^\dagger = u_k a_k^\dagger + v_k a_k, \quad (B.2)$$

$$\alpha_k = u_k a_k - v_k a_{\bar{k}}^\dagger, \quad (B.3)$$

$$\alpha_{\bar{k}} = u_k a_{\bar{k}} + v_k a_k^\dagger. \quad (\text{B.4})$$

Here k is a collective index for the single-particle states in the so-called *canonical basis*, i.e., the eigenbasis of the HFB density matrix. The bars indicate time-reversed states. The occupation coefficients can be chosen to be real if only like-particle (i.e., proton–proton and neutron–neutron) pairing is considered, and they satisfy

$$u_k^2 + v_k^2 = 1. \quad (\text{B.5})$$

In terms of these coefficients, a solution of the HFB equations can be written as

$$|\Phi\rangle = \prod_k \alpha_k |\text{vac}\rangle = \prod_{k>0} (u_k + v_k a_k^\dagger a_{\bar{k}}^\dagger) |\text{vac}\rangle, \quad (\text{B.6})$$

where $|\text{vac}\rangle$ refers to the particle vacuum state. It is clear from equation (B.6) that $|\Phi\rangle$ is a superposition of states with even proton and neutron number, and therefore not an eigenstate of the corresponding proton, neutron, or nucleon number operators. The HFB equations are solved under the constraint that the *expectation values* of these number operators match a given nucleus.

The broken particle-number symmetry can be restored by projecting $|\Phi\rangle$ on good Z and N with the operator

$$P_{ZN} = P_Z P_N = \frac{1}{(2\pi)^2} \int_0^{2\pi} d\phi_p \int_0^{2\pi} d\phi_n e^{i\phi_p(\hat{Z}-Z)} e^{i\phi_n(\hat{N}-N)}. \quad (\text{B.7})$$

Expectation values in the projected HFB states are formally given by

$$\langle \Phi_{ZN} | O | \Phi_{ZN} \rangle = \frac{\langle \Phi | OP_{ZN} | \Phi \rangle}{\langle \Phi | P_{ZN} | \Phi \rangle}. \quad (\text{B.8})$$

Under the unitary transformations generated by the number operators, the particle creation and annihilation operators transform as

$$e^{i\phi_k \hat{A}_k} a_k^\dagger e^{-i\phi_k \hat{A}_k} = e^{i\phi_k} a_k^\dagger, \quad (\text{B.9})$$

$$e^{i\phi_k \hat{A}_k} a_k e^{-i\phi_k \hat{A}_k} = e^{-i\phi_k} a_k, \quad (\text{B.10})$$

where $\phi_k \in \{\phi_p, \phi_n\}$ and $\hat{A}_k \in \{\hat{Z}, \hat{N}\}$ are the appropriate gauge angle and number operator for the single-particle state k . Using these relations, we can write the gauge-rotated quasi-particle state as

$$\begin{aligned} |\Phi(\phi_p, \phi_n)\rangle &\equiv e^{i(\phi_p \hat{Z} + \phi_n \hat{N})} |\Phi\rangle \\ &= \prod_{k>0} (u_k + v_k e^{2i\phi_k} a_k^\dagger a_{\bar{k}}^\dagger) |\text{vac}\rangle \end{aligned} \quad (\text{B.11})$$

and introduce the proton and neutron norm kernels ($\tau = p, n$)

$$\begin{aligned} x_\tau(\phi_\tau) &\equiv \langle \Phi | e^{i\phi_\tau(\hat{A}_\tau - A_\tau)} | \Phi \rangle \\ &= e^{-i\phi_\tau A_\tau} \prod_{k>0} (u_k^2 + v_k^2 e^{2i\phi_k}). \end{aligned} \quad (\text{B.12})$$

The overlap between the particle-number projected state and the initial HFB state is now given by

$$\begin{aligned} \langle \Phi | P_{ZN} | \Phi \rangle &= \frac{1}{(2\pi)^2} \int_0^{2\pi} d\phi_p \int_0^{2\pi} d\phi_n \langle \Phi | e^{i\phi_p(\hat{Z}-Z)} e^{i\phi_n(\hat{N}-N)} | \Phi \rangle \\ &= \frac{1}{(2\pi)^2} \left(\int_0^{2\pi} d\phi_p x_p(\phi_p) \right) \left(\int_0^{2\pi} d\phi_n x_n(\phi_n) \right). \end{aligned} \quad (\text{B.13})$$

The numerator of equation (B.8) can be expressed in terms of the norm kernel and the gauge-rotated state as

$$\begin{aligned} \langle \Phi | OP_{ZN} | \Phi \rangle &= \frac{1}{(2\pi)^2} \\ &\times \int_0^{2\pi} d\phi_p \int_0^{2\pi} d\phi_n e^{-i(\phi_p Z + \phi_n N)} \langle \Phi | O e^{i(\phi_p \hat{Z} + \phi_n \hat{N})} | \Phi \rangle \\ &= \frac{1}{(2\pi)^2} \int_0^{2\pi} d\phi_p \int_0^{2\pi} d\phi_n \langle \Phi | e^{i(\phi_p(\hat{Z}-Z) + \phi_n(\hat{N}-N))} | \Phi \rangle \\ &\times \frac{\langle \Phi | O e^{i(\phi_p \hat{Z} + \phi_n \hat{N})} | \Phi \rangle}{\langle \Phi | e^{i(\phi_p \hat{Z} + \phi_n \hat{N})} | \Phi \rangle} \\ &= \frac{1}{(2\pi)^2} \int_0^{2\pi} d\phi_p \int_0^{2\pi} d\phi_n x_p(\phi_p) x_n(\phi_n) \\ &\times \frac{\langle \Phi | O | \Phi(\phi_p, \phi_n) \rangle}{\langle \Phi | \Phi(\phi_p, \phi_n) \rangle}. \end{aligned} \quad (\text{B.14})$$

Defining the operator kernel

$$O(\phi_p, \phi_n) \equiv \frac{\langle \Phi | O | \Phi(\phi_p, \phi_n) \rangle}{\langle \Phi | \Phi(\phi_p, \phi_n) \rangle} \quad (\text{B.15})$$

and the auxiliaries

$$\begin{aligned} y_\tau(\phi_\tau) &= \frac{x_\tau(\phi_\tau)}{\int_0^{2\pi} d\phi_\tau x_\tau(\phi_\tau)}, \\ \int_0^{2\pi} d\phi_\tau y_\tau(\phi_\tau) &= 1, \end{aligned} \quad (\text{B.16})$$

we can combine equations (B.13) and (B.14) into the following compact expression for the expectation value of O in the particle-number projected state:

$$\begin{aligned} \langle \Phi_{ZN} | O | \Phi_{ZN} \rangle &= \int_0^{2\pi} d\phi_p \int_0^{2\pi} d\phi_n y_p(\phi_p) y_n(\phi_n) O(\phi_p, \phi_n). \end{aligned} \quad (\text{B.17})$$

As we have seen above, the initial and gauge-rotated HFB states have essentially the same structure, because the transformation of the basis operators only introduces simple phase factors. This implies that a simple extension of Wick's theorem for non-orthogonal product states can be applied to express the operator kernel (B.15) in terms of the basic contractions [197], the so-called transition density matrix and transition pairing tensors:

$$\rho_{kl}(\phi_k) = \frac{\langle \Phi | a_l^\dagger a_k | \Phi(\phi_p, \phi_n) \rangle}{\langle \Phi | \Phi(\phi_p, \phi_n) \rangle}, \quad (\text{B.18})$$

$$\bar{\kappa}_{kl}(\phi_k) = \frac{\langle \Phi | a_k^\dagger a_l^\dagger | \Phi(\phi_p, \phi_n) \rangle}{\langle \Phi | \Phi(\phi_p, \phi_n) \rangle}, \quad (\text{B.19})$$

$$\kappa_{kl}(\phi_k) = \frac{\langle \Phi | a_l a_k | \Phi(\phi_p, \phi_n) \rangle}{\langle \Phi | \Phi(\phi_p, \phi_n) \rangle}. \quad (\text{B.20})$$

For $\phi_p = \phi_n = 0$, the standard density matrix and pairing tensor of non-projected HFB theory are obtained. Since we do not allow proton–neutron pairing here, the contractions only depend on the gauge angle matching the isospin projection contained in the collective indices, because the HFB product state factorizes into proton and neutron parts (see equations (B.6) and (B.11)):

$$|\Phi(\phi_p, \phi_n)\rangle = |\Phi_p(\phi_p)\rangle \otimes |\Phi_n(\phi_n)\rangle. \quad (\text{B.21})$$

For instance, if k and l are proton indices, we have

$$\begin{aligned} \rho_{kl}(\phi_p) &= \frac{\langle \Phi | a_l^\dagger a_k | \Phi(\phi_p, \phi_n) \rangle}{\langle \Phi | \Phi(\phi_p, \phi_n) \rangle} \\ &= \frac{\langle \Phi_p | a_l^\dagger a_k | \Phi_p(\phi_p) \rangle \langle \Phi_n | \Phi_n(\phi_n) \rangle}{\langle \Phi_p | \Phi_p(\phi_p) \rangle \langle \Phi_n | \Phi_n(\phi_n) \rangle} \\ &= \frac{\langle \Phi_p | a_l^\dagger a_k | \Phi_p(\phi_p) \rangle}{\langle \Phi_p | \Phi_p(\phi_p) \rangle}. \end{aligned} \quad (\text{B.22})$$

Switching to the tensorial notation we use for the MR-IMSRG, the transition density matrices and pairing tensors in the canonical basis representation are given by

$$\rho_l^k(\phi_\tau) = \frac{v_k^2 e^{2i\phi_\tau}}{u_k^2 + v_k^2 e^{2i\phi_\tau}} \delta_l^k, \quad (\text{B.23})$$

$$\bar{\kappa}^{kl}(\phi_\tau) = \frac{u_k v_k}{u_k^2 + v_k^2 e^{2i\phi_\tau}} \delta^{kl}, \quad (\text{B.24})$$

$$\kappa_{kl}(\phi_\tau) = \frac{u_k v_k e^{2i\phi_\tau}}{u_k^2 + v_k^2 e^{2i\phi_\tau}} \delta_{kl}. \quad (\text{B.25})$$

The one-body density matrix of the projected state is obtained by integration:

$$\begin{aligned} \rho_l^k &= \int_0^{2\pi} d\phi_k y_k(\phi_k) \rho_l^k(\phi_k) \\ &= \int_0^{2\pi} d\phi_k y_k(\phi_k) \frac{v_k^2 e^{2i\phi_\tau}}{u_k^2 + v_k^2 e^{2i\phi_\tau}} \delta_l^k. \end{aligned} \quad (\text{B.26})$$

We see that all of the density matrices are diagonal in the canonical basis, which is identical to the natural orbital basis that is most convenient for the formulation of the MR-IMSRG flow. We can also directly read off the projected occupation numbers n_k from equation (B.26).

The full two-body and three-body density matrices are given by

$$\begin{aligned} \rho_{mn}^{kl} &= \int_0^{2\pi} d\phi_p \int_0^{2\pi} d\phi_n y_p(\phi_p) y_n(\phi_n) \\ &\times \left(\frac{v_k^2 e^{2i\phi_k}}{u_k^2 + v_k^2 e^{2i\phi_k}} \frac{v_l^2 e^{2i\phi_l}}{u_l^2 + v_l^2 e^{2i\phi_l}} (\delta_m^k \delta_n^l - \delta_n^k \delta_m^l) \right. \\ &\left. + \frac{u_k v_k}{u_k^2 + v_k^2 e^{2i\phi_k}} \frac{u_m v_m e^{2i\phi_m}}{u_m^2 + v_m^2 e^{2i\phi_m}} \delta^{kl} \delta_{m\bar{n}} \right) \end{aligned} \quad (\text{B.27})$$

and

$$\begin{aligned} \rho_{stu}^{pqr} &= \int_0^{2\pi} d\phi_p \int_0^{2\pi} d\phi_n y_p(\phi_p) y_n(\phi_n) \\ &\times \left(\frac{v_p^2 e^{2i\phi_p}}{u_p^2 + v_p^2 e^{2i\phi_p}} \frac{v_q^2 e^{2i\phi_q}}{u_q^2 + v_q^2 e^{2i\phi_q}} \frac{v_r^2 e^{2i\phi_r}}{u_r^2 + v_r^2 e^{2i\phi_r}} \right. \\ &\times (\delta_s^p \delta_t^q \delta_u^r + \delta_t^p \delta_u^q \delta_s^r + \delta_u^p \delta_s^q \delta_t^r \\ &\quad - \delta_t^p \delta_s^q \delta_u^r - \delta_s^p \delta_u^q \delta_t^r - \delta_u^p \delta_t^q \delta_s^r) \\ &+ \frac{v_p^2 e^{2i\phi_p}}{u_p^2 + v_p^2 e^{2i\phi_p}} \frac{u_q v_q}{u_q^2 + v_q^2 e^{2i\phi_q}} \frac{u_t v_t e^{2i\phi_t}}{u_t^2 + v_t^2 e^{2i\phi_t}} \delta_s^p \delta^{qr} \delta_{t\bar{u}} \\ &- \frac{v_p^2 e^{2i\phi_p}}{u_p^2 + v_p^2 e^{2i\phi_p}} \frac{u_q v_q}{u_q^2 + v_q^2 e^{2i\phi_q}} \frac{u_s v_s e^{2i\phi_s}}{u_s^2 + v_s^2 e^{2i\phi_s}} \delta_t^p \delta^{qr} \delta_{s\bar{u}} \\ &+ \frac{v_p^2 e^{2i\phi_p}}{u_p^2 + v_p^2 e^{2i\phi_p}} \frac{u_q v_q}{u_q^2 + v_q^2 e^{2i\phi_q}} \frac{u_s v_s e^{2i\phi_s}}{u_s^2 + v_s^2 e^{2i\phi_s}} \delta_u^p \delta^{qr} \delta_{s\bar{t}} \\ &- \frac{v_q^2 e^{2i\phi_q}}{u_q^2 + v_q^2 e^{2i\phi_q}} \frac{u_p v_p}{u_p^2 + v_p^2 e^{2i\phi_p}} \frac{u_t v_t e^{2i\phi_t}}{u_t^2 + v_t^2 e^{2i\phi_t}} \delta_s^q \delta^{pr} \delta_{t\bar{u}} \\ &+ \frac{v_q^2 e^{2i\phi_q}}{u_q^2 + v_q^2 e^{2i\phi_q}} \frac{u_p v_p}{u_p^2 + v_p^2 e^{2i\phi_p}} \frac{u_s v_s e^{2i\phi_s}}{u_s^2 + v_s^2 e^{2i\phi_s}} \delta_t^q \delta^{pr} \delta_{s\bar{u}} \\ &- \frac{v_q^2 e^{2i\phi_q}}{u_q^2 + v_q^2 e^{2i\phi_q}} \frac{u_p v_p}{u_p^2 + v_p^2 e^{2i\phi_p}} \frac{u_s v_s e^{2i\phi_s}}{u_s^2 + v_s^2 e^{2i\phi_s}} \delta_u^q \delta^{pr} \delta_{s\bar{t}} \\ &+ \frac{v_r^2 e^{2i\phi_r}}{u_r^2 + v_r^2 e^{2i\phi_r}} \frac{u_p v_p}{u_p^2 + v_p^2 e^{2i\phi_p}} \frac{u_t v_t e^{2i\phi_t}}{u_t^2 + v_t^2 e^{2i\phi_t}} \delta_s^r \delta^{pq} \delta_{t\bar{u}} \\ &- \frac{v_r^2 e^{2i\phi_r}}{u_r^2 + v_r^2 e^{2i\phi_r}} \frac{u_p v_p}{u_p^2 + v_p^2 e^{2i\phi_p}} \frac{u_s v_s e^{2i\phi_s}}{u_s^2 + v_s^2 e^{2i\phi_s}} \delta_t^r \delta^{pq} \delta_{s\bar{u}} \\ &\left. + \frac{v_r^2 e^{2i\phi_r}}{u_r^2 + v_r^2 e^{2i\phi_r}} \frac{u_p v_p}{u_p^2 + v_p^2 e^{2i\phi_p}} \frac{u_s v_s e^{2i\phi_s}}{u_s^2 + v_s^2 e^{2i\phi_s}} \delta_u^r \delta^{pq} \delta_{s\bar{t}} \right). \end{aligned} \quad (\text{B.28})$$

From these, the irreducible two-body and three-body density matrices are obtained by subtracting all antisymmetrized products of lower-rank density matrices:

$$\lambda_{mn}^{kl} = \rho_{mn}^{kl} - \lambda_m^k \lambda_n^l + \lambda_n^k \lambda_m^l, \quad (\text{B.29})$$

$$\lambda_{stu}^{pqr} = \rho_{stu}^{pqr} - \mathcal{A}(\lambda_{st}^{pq} \lambda_u^r) - \mathcal{A}(\lambda_s^p \lambda_t^q \lambda_u^r). \quad (\text{B.30})$$

References

- [1] Rainwater J 1950 *Phys. Rev.* **79** 432–4
- [2] Bohr A 1951 *Phys. Rev.* **81** 134–8
- [3] Bohr A and Mottelson B R 1953 *Dan. Mat. Fys. Medd.* **27** 1–174
- [4] Bohr A and Mottelson B R 1953 *Phys. Rev.* **89** 316–7
- [5] Bohr A and Mottelson B R 1953 *Phys. Rev.* **90** 717–9
- [6] Brown B A 2001 *Prog. Part. Nucl. Phys.* **47** 517–99
- [7] Caurier E, Martínez-Pinedo G, Nowacki F, Poves A and Zuker A P 2005 *Rev. Mod. Phys.* **77** 427–88
- [8] Brown B A and Richter W A 2006 *Phys. Rev. C* **74** 034315

- [9] Erler J, Birge N, Kortelainen M, Nazarewicz W, Olsen E, Perhac A M and Stoitsov M 2012 *Nature* **486** 509–12
- [10] Kortelainen M, Lesinski T, Moré J, Nazarewicz W, Sarich J, Schunck N, Stoitsov M V and Wild S 2010 *Phys. Rev. C* **82** 024313
- [11] Kortelainen M, McDonnell J, Nazarewicz W, Reinhard P G, Sarich J, Schunck N, Stoitsov M V and Wild S M 2012 *Phys. Rev. C* **85** 024304
- [12] McDonnell J D, Schunck N, Higdon D, Sarich J, Wild S M and Nazarewicz W 2015 *Phys. Rev. Lett.* **114** 122501
- [13] Detmold W 2015 *Nuclear Physics from Lattice QCD* (Cham: Springer) pp 153–94
- [14] Epelbaum E, Hammer H W and Meißner U G 2009 *Rev. Mod. Phys.* **81** 1773–825
- [15] Machleidt R and Entem D 2011 *Phys. Rep.* **503** 1–75
- [16] Epelbaum E, Krebs H and Meißner U G 2015 *Phys. Rev. Lett.* **115** 122301
- [17] Entem D R, Kaiser N, Machleidt R and Nosyk Y 2015 *Phys. Rev. C* **91** 014002
- [18] Gezerlis A, Tews I, Epelbaum E, Freunek M, Gandolfi S, Hebeler K, Nogga A and Schwenk A 2014 *Phys. Rev. C* **90** 054323
- [19] Lynn J E, Tews I, Carlson J, Gandolfi S, Gezerlis A, Schmidt K E and Schwenk A 2016 *Phys. Rev. Lett.* **116** 062501
- [20] Pastore S, Girlanda L, Schiavilla R, Viviani M and Wiringa R B 2009 *Phys. Rev. C* **80** 034004
- [21] Pastore S, Girlanda L, Schiavilla R and Viviani M 2011 *Phys. Rev. C* **84** 024001
- [22] Piarulli M, Girlanda L, Marcucci L E, Pastore S, Schiavilla R and Viviani M 2013 *Phys. Rev. C* **87** 014006
- [23] Kölling S, Epelbaum E, Krebs H and Meißner U G 2009 *Phys. Rev. C* **80** 045502
- [24] Kölling S, Epelbaum E, Krebs H and Meißner U G 2011 *Phys. Rev. C* **84** 054008
- [25] Ekström A, Jansen G R, Wendt K A, Hagen G, Papenbrock T, Carlsson B D, Forssén C, Hjorth-Jensen M, Navrátil P and Nazarewicz W 2015 *Phys. Rev. C* **91** 051301
- [26] Shirokov A M, Mazur A I, Zaytsev S A, Vary J P and Weber T A 2004 *Phys. Rev. C* **70** 044005
- [27] Shirokov A M, Vary J P, Mazur A I, Zaytsev S A and Weber T A 2005 *Phys. Lett. B* **621** 96–101
- [28] Shirokov A M, Vary J P, Mazur A I and Weber T A 2007 *Phys. Lett. B* **644** 33–7
- [29] Shirokov A M, Shin I J, Kim Y, Sosonkina M, Maris P and Vary J P 2016 *Phys. Lett. B* **761** 87–91
- [30] Bogner S K, Kuo T T S and Schwenk A 2003 *Phys. Rep.* **386** 1–27
- [31] Bogner S K, Furnstahl R J and Perry R J 2007 *Phys. Rev. C* **75** 061001(R)
- [32] Bogner S K, Furnstahl R J and Schwenk A 2010 *Prog. Part. Nucl. Phys.* **65** 94–147
- [33] Furnstahl R J and Hebeler K 2013 *Rep. Prog. Phys.* **76** 126301
- [34] Bethe H A 1971 *Ann. Rev. Nucl. Sci.* **21** 93–244
- [35] Polyzou W and Glöckle W 1990 *Few-Body Syst.* **9** 97–121
- [36] Kuo T 1967 *Nucl. Phys. A* **90** 199–208
- [37] Kuo T T S and Brown G E 1968 *Nucl. Phys. A* **114** 241–79
- [38] Brueckner K A, Levinson C A and Mahmoud H M 1954 *Phys. Rev.* **95** 217–28
- [39] Brueckner K A and Levinson C A 1955 *Phys. Rev.* **97** 1344–52
- [40] Day B D 1967 *Rev. Mod. Phys.* **39** 719–44
- [41] Barrett B R and Kirson M W 1970 *Nucl. Phys. A* **148** 145–80
- [42] Kirson M W 1971 *Ann. Phys., NY* **66** 624–50
- [43] Barrett B R 1972 *Phys. Lett. B* **38** 371–5
- [44] Kirson M W 1974 *Ann. Phys., NY* **82** 345–68
- [45] Goode P and Kirson M W 1974 *Phys. Lett. B* **51** 221–4
- [46] Vary J P, Sauer P U and Wong C W 1973 *Phys. Rev. C* **7** 1776–85
- [47] Glazek S D and Wilson K G 1993 *Phys. Rev. D* **48** 5863–72
- [48] Wegner F 1994 *Ann. Phys., Lpz.* **3** 77
- [49] Bogner S K, Furnstahl R J, Ramanan S and Schwenk A 2006 *Nucl. Phys. A* **773** 203–20
- [50] Tichai A, Langhammer J, Binder S and Roth R 2016 *Phys. Lett. B* **756** 283–8
- [51] Roth R and Langhammer J 2010 *Phys. Lett. B* **683** 272–7
- [52] Barrett B R, Navrátil P and Vary J P 2013 *Prog. Part. Nucl. Phys.* **69** 131–81
- [53] Jurgenson E D, Maris P, Furnstahl R J, Navrátil P, Ormand W E and Vary J P 2013 *Phys. Rev. C* **87** 054312
- [54] Hergert H, Binder S, Calci A, Langhammer J and Roth R 2013 *Phys. Rev. Lett.* **110** 242501
- [55] Roth R, Calci A, Langhammer J and Binder S 2014 *Phys. Rev. C* **90** 024325
- [56] Binder S, Langhammer J, Calci A and Roth R 2014 *Phys. Lett. B* **736** 119–23
- [57] Hagen G, Papenbrock T, Hjorth-Jensen M and Dean D J 2014 *Rep. Prog. Phys.* **77** 096302
- [58] Hagen G, Hjorth-Jensen M, Jansen G R and Papenbrock T 2016 *Phys. Scr.* **91** 063006
- [59] Tsukiyama K, Bogner S K and Schwenk A 2011 *Phys. Rev. Lett.* **106** 222502
- [60] Hergert H, Bogner S K, Binder S, Calci A, Langhammer J, Roth R and Schwenk A 2013 *Phys. Rev. C* **87** 034307
- [61] Hergert H, Bogner S K, Morris T D, Schwenk A and Tsukiyama K 2016 *Phys. Rep.* **621** 165–222
- [62] Brown B and Rae W 2014 *Nucl. Data Sheets* **120** 115–8
- [63] Kehrlein S 2006 *The Flow Equation Approach to Many-Particle Systems* (Springer Tracts in Modern Physics vol 237) (Berlin: Springer)
- [64] Heidbrink C and Uhrig G 2002 *Eur. Phys. J. B* **30** 443–59
- [65] Drescher N A, Fischer T and Uhrig G S 2011 *Eur. Phys. J. B* **79** 225–40
- [66] Krull H, Drescher N A and Uhrig G S 2012 *Phys. Rev. B* **86** 125113
- [67] Fauseweh B and Uhrig G S 2013 *Phys. Rev. B* **87** 184406
- [68] Krones J and Uhrig G S 2015 *Phys. Rev. B* **91** 125102
- [69] Shavitt I and Bartlett R J 2009 *Many-Body Methods in Chemistry and Physics: MBPT and Coupled-Cluster Theory* (Cambridge: Cambridge University Press)
- [70] White S R 2002 *J. Chem. Phys.* **117** 7472–82
- [71] Yanai T and Chan G K L 2006 *J. Chem. Phys.* **124** 194106 (pages 16)
- [72] Yanai T and Chan G K L 2007 *J. Chem. Phys.* **127** 104107 (pages 14)
- [73] Nakatsuji H 1976 *Phys. Rev. A* **14** 41–50
- [74] Valdemoro C 1987 *Theory and Practice of the Spin-Adapted Reduced Hamiltonians (SRH)* (Dordrecht: Springer Netherlands) pp 275–88
- [75] Mukherjee D and Kutzelnigg W 2001 *J. Chem. Phys.* **114** 2047–61
- [76] Kutzelnigg W and Mukherjee D 2002 *J. Chem. Phys.* **116** 4787–801
- [77] Kutzelnigg W and Mukherjee D 2004 *J. Chem. Phys.* **120** 7340–9
- [78] Kutzelnigg W and Mukherjee D 2004 *J. Chem. Phys.* **120** 7350–68
- [79] Mazziotti D A 2006 *Phys. Rev. Lett.* **97** 143002
- [80] Mazziotti D A 2007 *Reduced-Density-Matrix Mechanics: With Applications to Many-Electron Atoms and Molecules* (Advances in Chemical Physics vol 134) (New York: Wiley)
- [81] Evangelista F A 2014 *J. Chem. Phys.* **141** 054109
- [82] Li C and Evangelista F A 2015 *J. Chem. Theory Comput.* **11** 2097–108
- [83] Li C and Evangelista F A 2016 *J. Chem. Phys.* **144** 164114

- [84] Hannon K P, Li C and Evangelista F A 2016 *J. Chem. Phys.* **144** 204111
- [85] Dyson F J 1949 *Phys. Rev.* **75** 1736–55
- [86] Blanes S, Casas F, Oteo J and Ros J 2009 *Phys. Rep.* **470** 151–238
- [87] Brockett R 1991 *Linear Algebr. Appl.* **146** 79–91
- [88] Chu M T 1994 *Fields Inst. Commun.* **3** 87–97
- [89] Chu M T 1995 *Linear Algebr. Appl.* **215** 261–73
- [90] Roth R, Langhammer J, Calci A, Binder S and Navrátil P 2011 *Phys. Rev. Lett.* **107** 072501
- [91] Hergert H, Bogner S K, Morris T D, Binder S, Calci A, Langhammer J and Roth R 2014 *Phys. Rev. C* **90** 041302
- [92] Hagen G, Papenbrock T, Dean D J and Hjorth-Jensen M 2010 *Phys. Rev. C* **82** 034330
- [93] Roth R, Binder S, Vobig K, Calci A, Langhammer J and Navrátil P 2012 *Phys. Rev. Lett.* **109** 052501
- [94] Binder S, Langhammer J, Calci A, Navrátil P and Roth R 2013 *Phys. Rev. C* **87** 021303
- [95] Somà V, Duguet T and Barbieri C 2011 *Phys. Rev. C* **84** 064317
- [96] Somà V, Barbieri C and Duguet T 2013 *Phys. Rev. C* **87** 011303
- [97] Somà V, Barbieri C and Duguet T 2014 *Phys. Rev. C* **89** 024323
- [98] Somà V, Cipollone A, Barbieri C, Navrátil P and Duguet T 2014 *Phys. Rev. C* **89** 061301
- [99] Jurgenson E D, Navrátil P and Furnstahl R J 2009 *Phys. Rev. Lett.* **103** 082501
- [100] Hebeler K 2012 *Phys. Rev. C* **85** 021002
- [101] Griesshammer H W 2015 Assessing theory uncertainties in EFT power countings from residual cutoff dependence *Proc. of the 8th Int. Workshop on Chiral Dynamics PoS(CD15)* 104
- [102] Jurgenson E D, Navrátil P and Furnstahl R J 2011 *Phys. Rev. C* **83** 034301
- [103] Wendt K A 2013 Advances in the application of the similarity renormalization group to strongly interacting systems *PhD Thesis* The Ohio State University
- [104] Epelbaum E, Nogga A, Glöckle W, Kamada H, Meißner U G and Witała H 2002 *Phys. Rev. C* **66** 064001
- [105] Epelbaum E 2006 *Prog. Part. Nucl. Phys.* **57** 654–741
- [106] Gazit D, Quaglioni S and Navrátil P 2009 *Phys. Rev. Lett.* **103** 102502
- [107] Wendt K A 2013 *Phys. Rev. C* **87** 061001
- [108] Wang M, Audi G, Wapstra A, Kondev F, MacCormick M, Xu X and Pfeiffer B 2012 *Chin. Phys. C* **36** 1603
- [109] Calci A 2014 Evolved chiral Hamiltonians at the three-body level and beyond *PhD Thesis* TU Darmstadt
- [110] De la Madrid R 2005 *Eur. J. Phys.* **26** 287
- [111] Michel N, Nazarewicz W, Płoszajczak M and Vertse T 2009 *J. Phys. G: Nucl. Part. Phys.* **36** 013101
- [112] Jaganathan Y, Michel N and Płoszajczak M 2014 *Phys. Rev. C* **89** 034624
- [113] Fossez K, Michel N, Płoszajczak M, Jaganathan Y and Id Betan R M 2015 *Phys. Rev. C* **91** 034609
- [114] Roth R, Neff T and Feldmeier H 2010 *Prog. Part. Nucl. Phys.* **65** 50–93
- [115] Kutzelnigg W and Mukherjee D 1997 *J. Chem. Phys.* **107** 432–49
- [116] Kong L, Nooijen M and Mukherjee D 2010 *J. Chem. Phys.* **132** 234107 (pages 8)
- [117] Hergert H and Roth R 2009 *Phys. Lett. B* **682** 27–32
- [118] Hagen G, Papenbrock T, Dean D J, Schwenk A, Nogga A, Włoch M and Piecuch P 2007 *Phys. Rev. C* **76** 034302
- [119] Binder S, Piecuch P, Calci A, Langhammer J, Navrátil P and Roth R 2013 *Phys. Rev. C* **88** 054319
- [120] Gebrerufael E, Calci A and Roth R 2016 *Phys. Rev. C* **93** 031301
- [121] Tsukiyama K, Bogner S K and Schwenk A 2012 *Phys. Rev. C* **85** 061304
- [122] Morris T D, Parzuchowski N M and Bogner S K 2015 *Phys. Rev. C* **92** 034331
- [123] Brandow B H 1967 *Rev. Mod. Phys.* **39** 771–828
- [124] Fetter A and Walecka J 2003 *Quantum Theory of Many-particle Systems Dover Books on Physics* (New York: Dover)
- [125] Dickhoff W and Barbieri C 2004 *Prog. Part. Nucl. Phys.* **52** 377–496
- [126] Barbieri C, Van Neck D and Dickhoff W H 2007 *Phys. Rev. A* **76** 052503
- [127] Cipollone A, Barbieri C and Navrátil P 2013 *Phys. Rev. Lett.* **111** 062501
- [128] Kutzelnigg W 1982 *J. Chem. Phys.* **77** 3081–97
- [129] Kutzelnigg W and Koch S 1983 *J. Chem. Phys.* **79** 4315–35
- [130] Kutzelnigg W 1984 *J. Chem. Phys.* **80** 822–30
- [131] Epstein P S 1926 *Phys. Rev.* **28** 695–710
- [132] Nesbet R K 1955 *Proc. R. Soc. A* **230** 312–21
- [133] Carlson J, Gandolfi S, Pederiva F, Pieper S C, Schiavilla R, Schmidt K E and Wiringa R B 2015 *Rev. Mod. Phys.* **87** 1067–118
- [134] Entem D R and Machleidt R 2003 *Phys. Rev. C* **68** 041001
- [135] Ekström A *et al* 2013 *Phys. Rev. Lett.* **110** 192502
- [136] Hebeler K, Krebs H, Epelbaum E, Golak J and Skibiński R 2015 *Phys. Rev. C* **91** 044001
- [137] Epelbaum E, Krebs H and Meißner U G 2015 *Eur. Phys. J. A* **51** 1–29
- [138] Binder S *et al* 2016 *Phys. Rev. C* **93** 044002
- [139] Entem D R, Kaiser N, Machleidt R and Nosyk Y 2015 *Phys. Rev. C* **91** 014002
- Entem D R, Kaiser N, Machleidt R and Nosyk Y 2015 *Phys. Rev. C* **92** 064001
- [140] Hagen G *et al* 2015 *Nat. Phys.* **12** 186
- [141] Garcia Ruiz R F *et al* 2016 *Nat. Phys.* **12** 594–8
- [142] Coon S A, Avetian M I, Kruse M K G, van Kolck U, Maris P and Vary J P 2012 *Phys. Rev. C* **86** 054002
- [143] Furnstahl R J, Hagen G and Papenbrock T 2012 *Phys. Rev. C* **86** 031301
- [144] More S N, Ekström A, Furnstahl R J, Hagen G and Papenbrock T 2013 *Phys. Rev. C* **87** 044326
- [145] Furnstahl R J, More S N and Papenbrock T 2014 *Phys. Rev. C* **89** 044301
- [146] Furnstahl R J, Hagen G, Papenbrock T and Wendt K A 2015 *J. Phys. G: Nucl. Part. Phys.* **42** 034032
- [147] Wendt K A, Forssén C, Papenbrock T and Sääf D 2015 *Phys. Rev. C* **91** 061301
- [148] Odell D, Papenbrock T and Platter L 2016 *Phys. Rev. C* **93** 044331
- [149] Hergert H and Roth R 2009 *Phys. Rev. C* **80** 024312
- [150] Calci A and Roth R 2016 *Phys. Rev. C* **94** 014322
- [151] Angeli I and Marinova K P 2013 *At. Data Nucl. Data Tables* **99** 69–95
- [152] Gebrerufael E, Vobig K, Hergert H and Roth R 2016 Ab initio description of open-shell nuclei: merging no-core shell model and in-medium similarity renormalization group (<https://arxiv.org/abs/1610.05254>)
- [153] Taube A G and Bartlett R J 2008 *J. Chem. Phys.* **128** 044110 (pages 13)
- [154] Taube A G and Bartlett R J 2008 *J. Chem. Phys.* **128** 044111 (pages 9)
- [155] Roth R, Papakonstantinou P, Paar N, Hergert H, Neff T and Feldmeier H 2006 *Phys. Rev. C* **73** 044312

- [156] Günther A, Roth R, Hergert H and Reinhardt S 2010 *Phys. Rev. C* **82** 024319
- [157] Hebeler K, Bogner S K, Furnstahl R J, Nogga A and Schwenk A 2011 *Phys. Rev. C* **83** 031301
- [158] Langhammer J, Roth R and Stumpf C 2012 *Phys. Rev. C* **86** 054315
- [159] Cipollone A, Barbieri C and Navrátil P 2015 *Phys. Rev. C* **92** 014306
- [160] Otsuka T, Suzuki T, Holt J D, Schwenk A and Akaishi Y 2010 *Phys. Rev. Lett.* **105** 032501
- [161] Hagen G, Hjorth-Jensen M, Jansen G R, Machleidt R and Papenbrock T 2012 *Phys. Rev. Lett.* **108** 242501
- [162] Epelbaum E, Krebs H, Lähde T A, Lee D, Meißner U G and Rupak G 2014 *Phys. Rev. Lett.* **112** 102501
- [163] Holt J, Menéndez J and Schwenk A 2013 *Eur. Phys. J. A* **49** 1–6
- [164] Bogner S K, Hergert H, Holt J D, Schwenk A, Binder S, Calci A, Langhammer J and Roth R 2014 *Phys. Rev. Lett.* **113** 142501
- [165] Stroberg S R, Hergert H, Holt J D, Bogner S K and Schwenk A 2016 *Phys. Rev. C* **93** 051301
- [166] Roth R and Navrátil P 2007 *Phys. Rev. Lett.* **99** 092501
- [167] Roth R 2009 *Phys. Rev. C* **79** 064324
- [168] Piecuch P and Włoch M 2005 *J. Chem. Phys.* **123** 224105
- [169] Lee D 2009 *Prog. Part. Nucl. Phys.* **63** 117–54
- [170] Hoffman C R *et al* 2008 *Phys. Rev. Lett.* **100** 152502
- [171] Kohley Z *et al* 2015 *Phys. Rev. C* **91** 034323
- [172] Caesar C *et al* (R3B Collaboration) 2013 *Phys. Rev. C* **88** 034313
- [173] Lunderberg E *et al* 2012 *Phys. Rev. Lett.* **108** 142503
- [174] Schuster M D, Quaglioni S, Johnson C W, Jurgenson E D and Navrátil P 2014 *Phys. Rev. C* **90** 011301
- [175] Lapoux V, Somà V, Barbieri C, Hergert H, Holt J D and Stroberg S R 2016 *Phys. Rev. Lett.* **117** 052501
- [176] Wienholtz F *et al* 2013 *Nature* **498** 346–9
- [177] Hagen G, Hjorth-Jensen M, Jansen G R, Machleidt R and Papenbrock T 2012 *Phys. Rev. Lett.* **109** 032502
- [178] Holt J D, Otsuka T, Schwenk A and Suzuki T 2012 *J. Phys. G: Nucl. Part. Phys.* **39** 085111
- [179] Holt J D, Menéndez J, Simonis J and Schwenk A 2014 *Phys. Rev. C* **90** 024312
- [180] Gallant A T *et al* 2012 *Phys. Rev. Lett.* **109** 032506
- [181] Steppenbeck D *et al* 2013 *Nature* **502** 207–10
- [182] Kreim K *et al* 2014 *Phys. Lett. B* **731** 97–102
- [183] Chiara C J *et al* 2012 *Phys. Rev. C* **86** 041304
- [184] Recchia F *et al* 2013 *Phys. Rev. C* **88** 041302
- [185] Suchyta S *et al* 2014 *Phys. Rev. C* **89** 021301
- [186] Marinova K *et al* 2011 *Phys. Rev. C* **84** 034313
- [187] Gibelin J *et al* 2007 *Phys. Rev. C* **75** 057306
- [188] Lepailleur A *et al* 2013 *Phys. Rev. Lett.* **110** 082502
- [189] Cáceres L *et al* 2015 *Phys. Rev. C* **92** 014327
- [190] Jansen G R, Engel J, Hagen G, Navrátil P and Signoracci A 2014 *Phys. Rev. Lett.* **113** 142502
- [191] Lisetskiy A F, Barrett B R, Kruse M K G, Navrátil P, Stetcu I and Vary J P 2008 *Phys. Rev. C* **78** 044302
- [192] Dikmen E, Lisetskiy A F, Barrett B R, Maris P, Shirokov A M and Vary J P 2015 *Phys. Rev. C* **91** 064301
- [193] National Nuclear Data Center, information extracted from the NuDat 2 database, <http://nndc.bnl.gov/nudat2/>
- [194] Jansen G R, Schuster M D, Signoracci A, Hagen G and Navrátil P 2016 *Phys. Rev. C* **94** 011301
- [195] Jansen G R 2013 *Phys. Rev. C* **88** 024305
- [196] von Oertzen W, Freer M and Kanada-En'yo Y 2006 *Phys. Rep.* **432** 43–113
- [197] Ring P and Schuck P 1980 *The Nuclear Many-Body Problem* 1st edn (Berlin: Springer)
- [198] Stroberg S R, Calci A, Hergert H, Holt J D, Bogner S K, Roth R and Schwenk A 2016 arXiv:1607.03229
- [199] Parzuchowski N M, Morris T D and Bogner S K 2016 Ab Initio excited states from the in-medium similarity renormalization group (<https://arxiv.org/abs/1611.00661>)
- [200] Sheikh J A and Ring P 2000 *Nucl. Phys. A* **665** 71–91